

II.I.A Next Generation Anodes for Lithium-Ion Batteries: Silicon

II.I.A Next Generation Anodes for Lithium-Ion Batteries: Silicon (ANL, LBNL, ORNL, SNL, NREL)

Jack Vaughey, Point-of-Contact
 Argonne National Laboratory
 9700 South Cass Avenue
 Argonne, IL 60439
 Phone: (630) 252-8885
 E-mail: vaughey@anl.gov

Brian Cunningham, DOE-EERE-VTO Program Manager
 Hybrid Electric Systems, Battery R&D
 Phone: (202) 287-5686
 E-mail: brian.cunningham@ee.doe.gov

Table of Contents

Project Introduction	(page 2)
Objectives	(page 4)
Milestones	(page 4)
Approach	(page 4)
1. Results: Silicon Electrode: Components	
Silicon	(page 5)
Conductive Additives	(page 12)
PAA Binder Processing	(page 17)
PAA Binder Modifications	(page 20)
BatPaC Models	(page 26)
Electrode Formation	(page 27)
Dispersants	(page 30)
Conclusions: Electrode Components	(page 33)
2. Results: Silicon Electrode: Testing Protocols	
Calendar Aging Screening Protocol	(page 35)
Data Collection	(page 37)
Data Analysis	(page 38)
Conclusions: Testing Protocols	(page 43)
3. Results: Silicon Electrode: Additives	
Silicon Pouch Cells with Multivalent Electrolyte	
Additives	(page 43)
Electrode Composition	(page 44)

Calendar Life Studies with Multivalent Electrolyte	
Additives	(page 47)
FEC & Temperature	(page 50)
SEI Solubility	(page 53)
Cation Crossover	(page 54)
Conclusions: Electrolyte Additives	(page 58)
4. Key Publications	(page 60)
5. References	(page 61)

Project Introduction

Silicon has received significant attention as an alternative active component to the graphitic carbon in a lithium-ion battery negative electrode due to its much higher capacity and general availability. Compared to graphitic carbons, silicon has nearly an order of magnitude higher capacity (~3600 mAh/g silicon vs 372 mAh/g graphite), however, several problems that limit its utility in commercial cells have been identified including large crystallographic expansion upon lithiation (~320%), slow lithium diffusion, and high reactivity with electrode constituents at high states of charge. Combined, these materials properties can result in particle cracking, particle isolation, electrolyte reactivity, and electrode delamination issues. These chemical reactivity and volume changes are manifested in SEI stability and cycling efficiency issues for the cell. Keeping this in mind, the large number of studies focused on silicon-based electrodes is a testament to the opportunity it presents but also the size of the challenge and innovation it inspires on multiple fronts. BatPaC, a techno-economic program

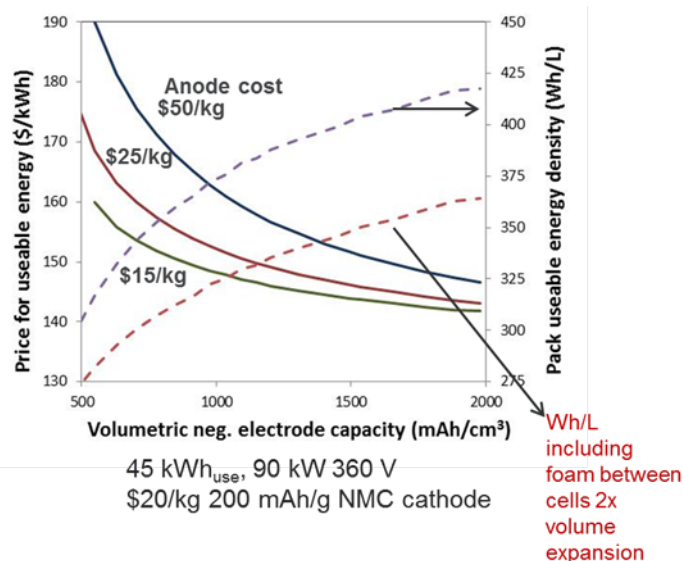


Figure II.I.A.1. Battery Performance and Cost (BatPaC) model utilized to establish relevance by connecting pack to anode targets.

designed to model lithium-ion battery performance and cost, was utilized to establish program relevance by connecting DOE/USABC pack performance targets to anode targets. BatPaC analysis of the needs for LIB anode (see Figure II.I.A.1) indicated that anode volumetric capacities greater than 1000 mAh/cm³ generally minimizes battery cost when coupled to an advanced NMC cathode.

The Next Generation Anodes for Lithium-Ion Batteries Program, also referred to as the Silicon DeepDive Program, is a consortium of five National Laboratories assembled to tackle the barriers associated with

development of an advanced lithium-ion negative electrode based on silicon as the active material. The program goals include establishing baseline silicon materials for the multi-lab research program, executing full cell development strategies that leverage DOE-EERE-VTO investments in electroactive materials and characterization, and identifying electrode-based limitations that effect full cell performance. The primary objective of this program is to understand and eliminate the barriers to implementation of a silicon-based anode in a lithium-ion cell. The five National Laboratories work as a single program with continuous interaction, established protocols for analysis, and targets for developing both an understanding and a cell chemistry associated with advance negative electrodes for lithium-ion cells. This undertaking is a full electrode/full cell chemistry project leveraging common baseline electrodes prepared at the consortium facilities. All efforts are directed to understanding and developing the chemistry needed for advancing silicon-based anodes operating in full cells. Team focus areas include active material development, binder synthesis, electrode formulations, and electrolyte additives. Efforts include modeling and a wide range of electrochemical, chemical, and structural characterization of the system across length- and timescales. Specialized characterization techniques developed with DOE-EERE-VTO funding, include neutron diffraction studies, MAS-NMR, optical spectroscopy methods, and X-ray based techniques. The project is managed as a single team effort spanning the Labs, with consensus decisions driving research directions and toward development of high-energy density lithium-ion batteries. A detailed list of participants is given in Figure II.I.A.2.

Contributors

▪ Daniel Abraham	▪ Alison Dunlop	▪ Min Ling	▪ Stephen Trask
▪ Shabbir Ahmed	▪ Yeyoung Ha	▪ Michael Liu	▪ Ritesh Uppuluri
▪ Elisabetta Arta	▪ Katherine Harrison	▪ Gao Liu	▪ Jack Vaughey
▪ Ira Bloom	▪ Sang-Don Han	▪ Wenquan Lu	▪ Gabriel Veith
▪ Su Ahmed	▪ Emma Hopkins	▪ Hannah Morin	▪ Johanna Welker
▪ Beth Armstrong	▪ Andrew Jansen	▪ Nate Neale	▪ Qingliu Wu
▪ Ryan Armstrong	▪ Sisi Jiang	▪ K. Nie	▪ Yimin Wu
▪ Katie Browning	▪ Haiping Jia	▪ Bryant Polzin	▪ Zhen Zhen Yang
▪ M. Katie Burdette- Trofimov	▪ Christopher Johnson	▪ Alexander Rogers	▪ Kang Yao
▪ Anthony Burrell	▪ Baris Key	▪ Andressa Rodriguez Prado	▪ Ji-Guang Zhang
▪ Saida Cora	▪ Robert Kostecki	▪ Marco Tulio F. Rodrigues	▪ Lu Zhang
▪ Jaclyn Coyle	▪ Joseph Kubal	▪ Niya Sa	▪ John Zhang
▪ Yanjie Cui	▪ Bob Jin Kwon	▪ Yangping Sheng	▪ Sanpei Zhang
▪ Dennis Dees	▪ Xiang Li	▪ Seoung-Bum Son	▪ Tianyue Zheng
▪ Fulya Dogan	▪ Xiaolin Li	▪ Caleb Stetson	▪ Ting Zhang
	▪ Chen Liao	▪ Wei Tong	

Research Facilities

- Post-Test Facility (PTF)
- Cell Analysis, Modeling, and Prototyping (CAMP)
- SLAC National Accelerator Laboratory
- Spallation Neutron Source (SNS-ORNL)
- Advanced Photon Source (APS-ANL)
- Battery Manufacturing Facility (BMF)
- Battery Abuse Testing Laboratory ([BATLab](#))

Figure II.I.A.2. Program participants including Laboratories, research facilities, and individual contributors.

Objectives

- Understand and overcome the science and technology barriers to the use of silicon-based anodes in high-energy density lithium-ion batteries for transportation applications.
 - Stabilize the SEI

- Stabilize the electrode structure
- Demonstrate functional prototype lithium-ion cell chemistries that include a silicon-containing anode which meet the DOE/USABC performance targets.

Milestones

FY20Q1	Evaluate two new binder - slurry – silicon laminate combinations that lead to improved stability and a 15% improvement in performance compared to baseline for a high silicon-loading (>60%) electrode. <i>(Completed 01/2020)</i>
FY20Q2	Assess and evaluate multiple surface driven coatings that utilize a multivalent surface substitution. Develop an understanding of the formation mechanism on the cycling stability of the underlying silicon electrode, propose a mechanism of formation. <i>(Completed 03/2020)</i>
FY20Q3	Assess the stability of electrode level silicon baseline materials on cycling and determine the range of species that solubilize and leach into the electrolyte. <i>(Completed 09/2020)</i>
FY20Q4	Combine the advancements made over various aspects of the silicon electrode by the Silicon Deep Dive team evaluate them at the full system level and optimize a best full cell with a commercial cathode that using BatPaC can be determined to deliver > 350 Wh/kg for 120 cycles, Evaluate the energy fade on standing for 2 mos and demonstrate an improvement over baseline of 20%. <i>(Completed 10/2020)</i>
FY20Q4	Have published a document that will enable other research and development groups to analyze stability of the SEI on a silicon-based anode, thus enabling developers or researchers to continually improve silicon cell stability (joint milestone with the SEISta). <i>(Completed 09/2020)</i>

Approach

Oak Ridge National Laboratory (ORNL), National Renewable Energy Laboratory (NREL), Pacific Northwest National Laboratory (PNNL), Lawrence Berkeley National Laboratory (LBNL), and Argonne National Laboratory (ANL) have teamed to form an integrated program dedicated to identifying, understanding, and proposing solutions to the problems associated with the commercialization of silicon as an active component of a lithium-ion electrochemical cell. Technical targets have been developed and regular communications have been established across the team through weekly meetings and quarterly face to face meetings. Throughout the program, the focus is on silicon-based materials, electrodes, and cells. Advancements will be verified based on cycle and calendar life and performance of full cells. Toward that end, baseline silicon-based materials, electrodes, and cells have been adopted, along with uniform full cell testing protocols.

With improvements, the baseline cell technology will be updated to reflect advances, new suppliers, and treatments based on the data and assessments from team members. Cycling and calendar life studies for baseline systems have adopted a testing protocol (based on literature reports) that has worked well for silicon-containing lithium-ion cells. The test consists of (1) three slow (C/20) formation cycles, (2) an HPPC cycle, (3) a set number of C/3 aging cycles, and finished with (4) another HPPC cycle, and (5) three slower (C/20) cycles. All constant current cycling is symmetric between charge and discharge rates. The tests are run at 30°C. This protocol effectively examines capacity, impedance, and aging effects in about a month's worth of testing. Our baseline silicon was produced by Paraclete Energy (Chelsea, MI) and has been made available to all participants on demand. The silicon was purchased in bulk from Paraclete to minimize batch to batch issues and electrode fabrication was done using consistent materials, compositions, and conditions. The cathode used (i.e. NMC,

LMR-NMC) is matched to the silicon by CAMP, the baseline electrolyte is 1.2M LiPF₆ in a 3:7 ratio of EC/EMC by weight (Gen2) plus 10 wt% FEC. Based on FY19 data, although it noticeably improved performance, a determination was made not to mandate the addition of Mg(TFSI)₂ as an electrolyte additive to the baseline system due to researcher concerns about battery grade salt availability and uncertainty of optimized concentrations at this time. The baseline research facilities include the Battery Abuse Testing Laboratory (BATLab), the Cell Analysis, Modeling, and Prototyping (CAMP), and the Post-Test Facility (PTF).

The fundamental understanding developed as part of the silicon DeepDive is based on extensive electrochemical and analytical studies of the components, electrodes, and cells conducted by researchers in the program. This effort contains in-situ and ex-situ studies on full and specialty cells, including reference electrode cells. Overall, the diagnostic studies are intended to help establish structure-composition-property relationships, including lithium-rich surface compounds, bulk transport, and kinetic phenomena. Together they form the basis for accurately assessing component and electrode failure modes and sets a path for advancements. Supported by the diagnostic studies, materials development on silicon-based materials, electrodes, and cells has been focused on enhancement of interfacial stability, accommodation of volume changes on lithiation, improvements in overall performance and life. A key avenue of research for this goal is the development and testing of electrolyte additives designed to modify and stabilize the dynamic silicon-electrolyte interface. In this past year we added more effort focused on soluble SEI species, alternative conductive additives, Zintl electrolyte additives, and calendar life testing and de-emphasized binder development and pre-lithiation developmental studies. Keeping with the goals of using full cell for the DeepDive effort, we increased efforts in the area of slurry and electrode formulation properties as a multi-Lab pathway to improve the baseline electrodes.

Communication of programmatic progress to battery community is critical. This will generally be accomplished through publications, presentations, reports, and reviews. Further, the program is open to industrial participation and/or collaboration that does not limit program innovation or the free flow of information. Finally, the DeepDive is highly integrated with the anode focused BMR researchers and the SEISta program, a sister program focused on stabilization of the silicon SEI layer. Generally, SEISta is focused on the development and characterization of model systems, surface analysis, well-defined thin film electrodes, and interfacial silicate phases and phenomena.

1. Results: Silicon Electrodes: Components

Silicon: In the DeepDive Silicon effort, the baseline silicon was purchased from Paraclete Energy (Chelsea, MI) in a large batch as needed by the program to ensure minimal baseline drift over the time of the program. This is partly to help offset some of the known batch to batch variability (i.e. surface areas and crystalline to amorphous materials ratio) and aging issues associated with silicon as it oxidizes and interacts with its storage environment. In part to better understand these phenomena and create a baseline material with a longer shelf-life for testing, we have been developing a mechanochemical mixing/grinding technique to convert low surface area and high purity silicon boules to silicon powders. The technique also allows us to directly functionalize the surface during size reduction to obtain starting materials which will optimize electrode formulation and SEI formation

In order to understand the processing parameters and mixing variables, a series of new high kinetic ball milling experiments were performed to evaluate the role of polyethylene glycol (PEG) concentration on the resulting Si particle sizes, morphology and reproducibility. Nine ball milling experiments were conducted at 700 RPM milling speed for various times and with two different ball media to powder ratios of 10/1 and 20/1. Concentrations of 0.5, 1 and 5 wt.% PEG (2,000 MW) were added to intrinsic silicon boules (~ 1-2 cm cubes) and ball milled with 2 kg of 440c milling media in ball-to-powder ratios of 10/1 or 20/1 for times ranging from

1 minute to 5 hours. The milling media was reused for each experiment to evaluate aging and chemical contamination. The particle size analysis detected bimodal distribution of particles in all the ball milling experiments, which is similar to the results reported previously from the first set of milling experiments. A very noticeable effect was the volume expansion of the Si powder ball milled with the PEG additions, which correlates with a decrease in the specific density of Si. Experimentally, using 200 g of powder consisting of 95% Si + 5% PEG resulted in a volume expansion that exceeded 500 cm³. The estimated density of the Si powder was 0.40 g/ml, or ~5.8 times lower than the 2.33g/ml density of bulk Si, demonstrating the strong interaction between PEG and the Si during ball milling.

As noted earlier, the samples isolated have a bi-modal distribution of particle sizes. Analysis of the data showed that the Si particles were continuously being fractured into smaller particles followed by agglomeration into larger particles by fusing of fractured particles during ball milling, resulting in the bimodal populations of Si particles. It was also observed that increasing the milling time led to larger agglomerated particles. Interestingly, the initial ball milling experiment at 700 RPM for 90 min. that was conducted on Si boule with ~0.5% PEG addition showed that the polymer did not have a significant effect on reducing the Si particle size compared to the Si boule ball milled with the same conditions without polymer. This result may indicate that interaction of PEG with the Si particles does not prevent the fusing of fractured Si particles during milling. Therefore, the effect of ball to powder ratio on Si particle size reduction was explored. Results comparing the ball milling of 200 g (10/1 ratio) and 100 g (20/1 ratio) of Si +1% PEG powder for 60 min. at 700 RPM are shown in Figure II.I.A.2. The plot shows the size and volume fraction of particles in the lower size population (LP) and upper size population (UP) of the bimodal size distributions. Although the 20/1 ball to powder ratio did not change the size of the LP particles there was an increase in the volume fraction of these particles compared to the UP particles. There was also a significant increase in the size of the UP particles with the larger 20/1 ball to powder ratio, strongly supporting the idea that Si particles agglomeration occurs.

The effect of milling time on the particle size was explored in another ball milling experiment. This experiment started with ball milling 200 g of powder consisting of 99% Si and 1% PEG at 700 RPM for 90 minutes. A bimodal particle size distribution resulted with one peak having an average size of 434 nm and volume fraction of 24.4% and the other peak having an average size of 3.58 μ m and volume fraction of 74.3%. From the experiments comparing the ball to powder ratio, it was decided to separate the 200 g of ball milled Si + 1% PEG powder into 100 g batches for additional milling times covering the range of 1, 10 and 60 min. at 700 RPM using a ball to powder ratio of 20/1. The ball milling run for 60 min. was stopped after 1 min. to extract a powder sample for size distribution analysis followed by ball milling the powder the remainder time of 59 min. The size distribution results obtained from these ball millings are shown in Figure II.I.A.3. There is a steady increase in volume fraction of the LP particles with increasing time even though no appreciable decrease in particle size occurred. This corresponds with a decrease in volume fraction of the UP particles, but as observed in previous experiments, there is a steady increase in the particle size. These results demonstrate that increasing the frequency of ball to powder collisions by increasing the ball to powder ratio improves the yield of nano-size Si particles but does not prevent the increase in size of the larger Si particles that occurs with increasing milling time.

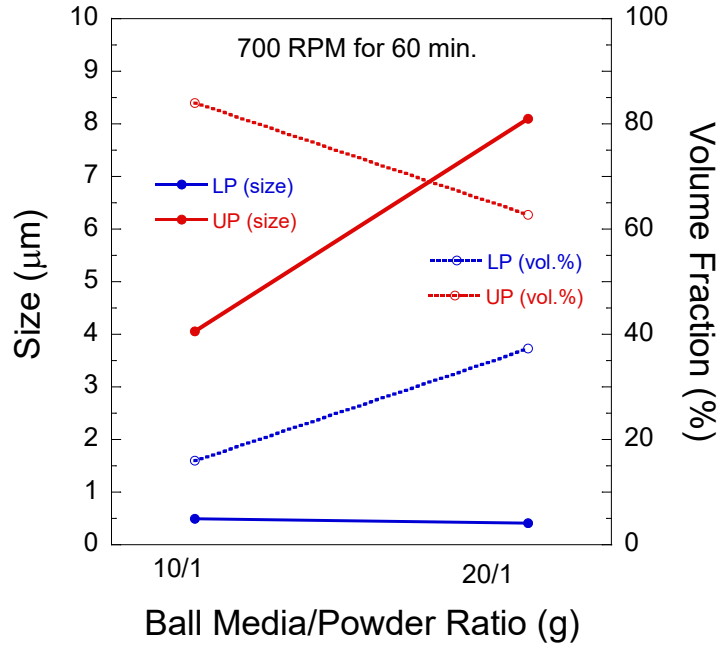


Figure II.I.A.3. Ball milling experiment comparing the effect of ball to powder ratio with particle size distribution.

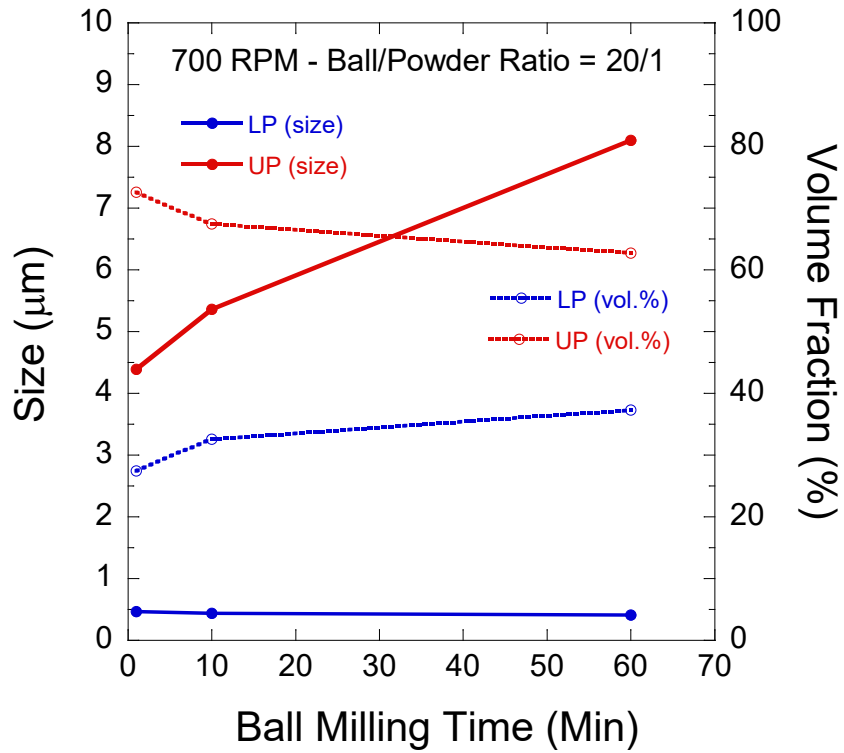


Figure II.I.A.4. Ball milling experiment comparing the effect milling time with particle size distribution.

The results of the ball milling experiments show the fracturing of Si particles exposes fresh surfaces that are extremely reactive and will reform bonds with other freshly cleaved Si particles or to surface active polymers, as demonstrated by the significant volume expansion of Si powder that was ball milled with PEG. The fusing of fractured Si particles causes the formation of larger size agglomerates with increasing milling time and higher ball to powder ratio. Further ball milling experiments will explore cooling the ball mill chamber as a means to promote more fracturing processes and less fusing that may lead to a higher volume fraction of Si particles in the 200-400 nm size range.

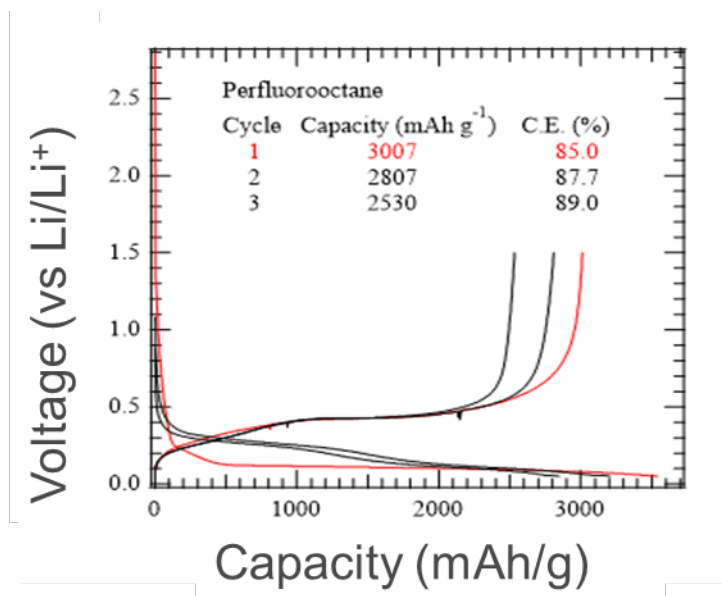


Figure II.I.A.5 Electrochemical performance of a silicon sample ball milled in the presence of perfluorooctane.

Milling silicon boules with additions of PEG polymers promoted significant reduction in the specific density of Si with concomitant volume expansion while increasing the ball to powder ratio to 20/1 helped to increase the volume fraction of Si particles in the ~400 nm size range. Ball milling experiments using a cooled milling chamber will be explored for keeping the Si powder from agglomerating into larger sizes. Further optimization of ball milling conditions for obtaining nano-size Si particles and additions of polymers during milling to create a uniform surface on the silicon powder will take place. These polymers may act like an artificial SEI. Consistent with this hypothesis, the best results to date have come from inert fluoropolymers, i.e. perfluorooctane (see Figure II.I.A.5) where the reactivity with the exposed silicon surfaces may be mediated by the stronger C-F bonds or the inert nature of the polymer itself to breakdown.

Besides the program baseline silicon from Paraclete Energy (Chelsea MI), development of alternative silicon materials has progressed in an effort to address issues not easily covered by the baseline material requirements, notably variation of passivation layer (i.e. silicon oxide) thickness and crystallite particle growth on cycling. One pathway has been designing and optimizing synthetic methods to create highly porous and nanostructured silicon materials that possess a thin oxide passivation created by an HF-based surface dissolution process. Once the oxide is removed, the surface is stabilized by a carbon coating. [1] While the large surface area can enhance kinetic issues, the continuous reaction between lithiated silicon and electrolyte still results in surface degradation and performance issues related to SEI growth. This was investigated extensively by Key, et al., as part of the DeepDive Silicon effort. [2] It is generally believed that minimizing the surface area of the active silicon structure can help minimize electrolyte reactivity and is critical for long term stability of the cells components.

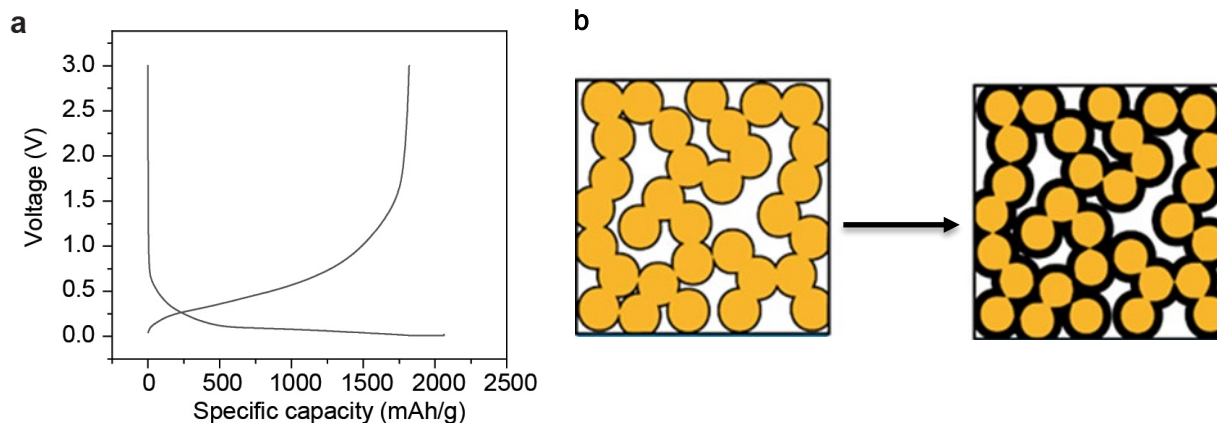


Figure II.I.A.6 (a) Electrochemical properties of pitch coated porous Si-C in the half-cell. The voltage profile of pitch coated porous Si anode at the first cycle under a 3V window testing protocol (b) cartoon showing synthesis of the porous silicon

With this electrolyte reactivity, the surface area of the silicon has strong implications for the silicon electrode calendar life. In an evaluation of carbon-coated porous silicon studies noted previously, Si||LFP full cells utilizing a pitch-coated porous etched silicon in baseline electrolyte and an LHCE (Figure II.I.A.6). Before full cell assembly, the porous silicon anode was characterized for its electrochemical properties in half-cells. The calendar-life studies for the pitch-coated porous silicon anode were tested using a protocol where it was cycled at a C/10 rate in the voltage window between 0.01 to 3.0V and a CV step at 0.01V. For this ~3 V window, the 1st cycle reversible capacity was found to be 1820 mAh/g (Si-C) with 88.3% of first cycle Coulombic Efficiency. Consistent with earlier CAMP results, the capacity of silicon is dependent on its voltage window. For the pitch-coated porous silicon, approximately 60% of the capacity is below 100mV (vs Li) on charge, while on discharge approximately 80% of the reversible capacity was found to be above 700mV (Figure II.I.A.6). More restricted windows, including one proposed for the SCP silicon half-cell electrochemical cells, would need to have gone thru a series of electrode conditioning cycles in order to fully activate the silicon, to be meaningful. Studies of this material continue as part of the SCP stage-gate process and seedling effort.

For calendar life full cell testing, the Silicon Consortium Protocols were used. A pitch-coated porous Si anode (~1.1 mAh/cm² at 0.1V), the anode was matched to an LFP cathode (~2.5 mAh/cm²) provided by Argonne's CAMP facility were utilized. The areal capacities of the electrodes were chosen to ensure enough Li⁺ inventory was available to supply the Si-containing test electrode during the aging protocol. The Silicon Consortium Protocol was based on (1) three formation cycles at a C/10 rate between 2.7 and 3.35V, the full cells are charged to 3.35V at a C/10 rate, followed by voltage hold at 3.35V for a set period (360, 720, 1440, and 2160 hours). During the voltage hold at 3.35V, the parasitic current and capacity are normalized by the charge capacity before voltage hold is obtained (Figure II.I.A.7). As shown in Figure II.I.A.7, the role of the electrolyte and its subsequent voltage hold stability is noted. Overall, the parasitic current of the full cells with LHCE was found to be much smaller than that of the full cells using Gen2+FEC. The observation is consistent with the lower reactivity of the LHCE systems (due in part to its inherent limited free solvent) when compared to the baseline Gen2+FEC electrolytes.

As an alternative to the C-coated porous silicon where the use of an LHCE electrolyte was effective in limiting parasitic reactions at higher states of charge, the embedding of electroactive silicon in a Li-Sn matrix was also investigated. The Li-Sn material acts as both a solid lithium ion conductor and a matrix buffer to inhibit particle growth. The amorphous Si and Si-Sn composite thin film materials were synthesized by magnetron sputtering

of the elements on Cu foils. The materials were tested in half-cells using in Gen2 electrolyte (1.2 M LiPF₆ in ethylene carbonate-ethyl methyl carbonate (3:7 by weight)). The cells were galvanostatically discharged and charged between 1.5 and 0.01 V at C/20 based on the experimental capacity. As shown in Figure II.I.A.8, the 180 nm a-Si film delivers an initial lithiation and delithiation capacity of 0.1697 and 0.1385 mAh cm⁻², respectively, while the 140 nm Si- Sn film exhibits a corresponding capacity of 0.1140 and 0.099 mAh cm⁻². Based on the theoretical density of Si and Sn, the calculated specific capacities are 4064 and 1782 mAh g⁻¹, respectively. These correspond to full lithiation for the Si and Si-Sn, respectively, with additional capacity attributed to SEI formation and electrode break-in processes. With similar degrees of initial lithiation, these two binder and carbon additive free electrodes exhibit different cycling behaviors (Figure II.I.A.8). The Si-Sn film exhibit quite stable cycling, even without the use of fluoroethylene carbonate (FEC) additive. The Li-Sn matrix, formed on lithiation, appears to stabilize the silicon cycling performance.

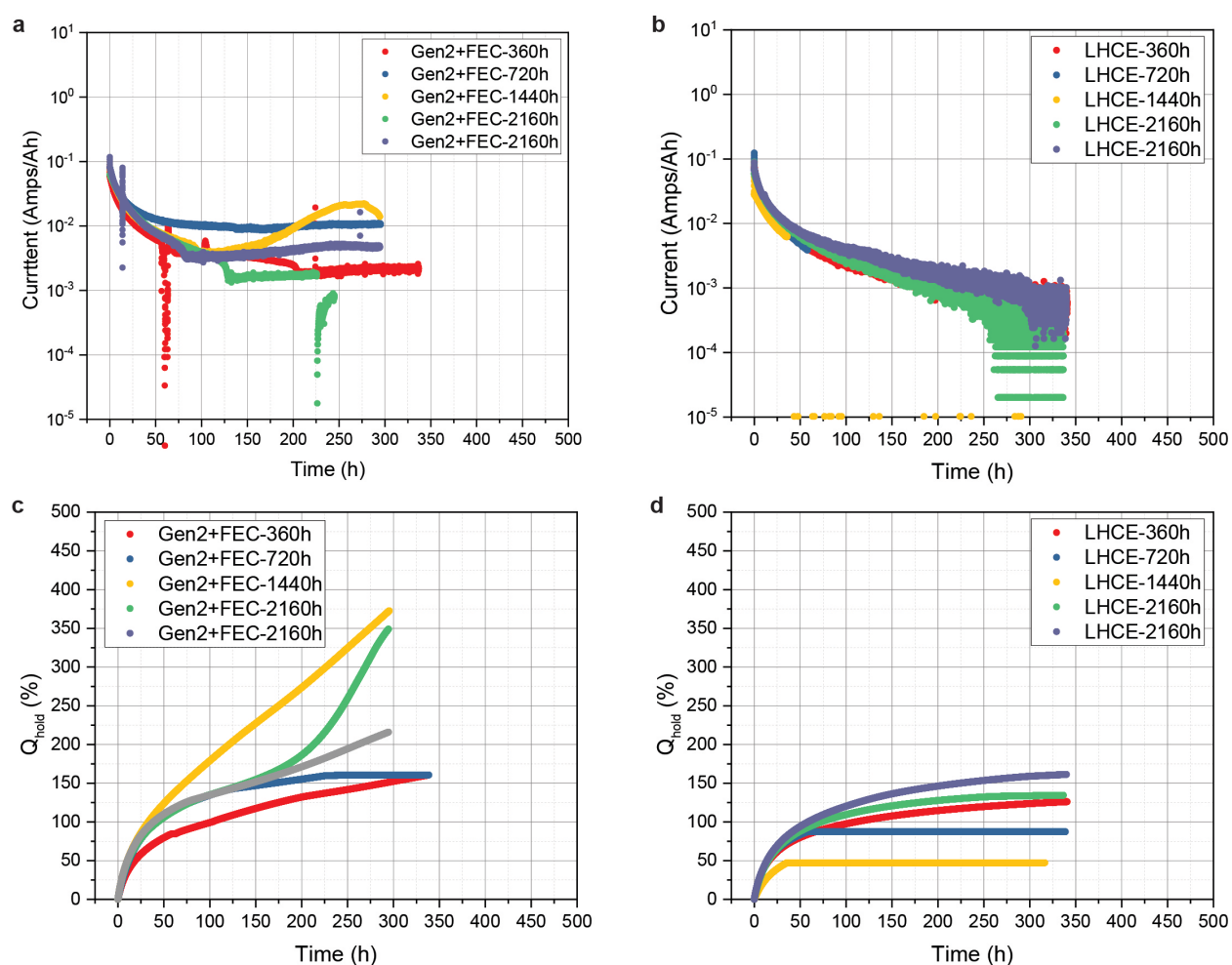


Figure II.I.A.7 Parasitic currents and accumulated capacities of Si | LFP full cells using Gen2+FEC (a, c) and LHCE (b, d) during the voltage hold at 3.35 V.

We examined the morphological/structural changes upon lithiation to understand the impact of volume change, which is believed to contribute to the poor capacity retention. Figure II.I.A.9 shows the cross-sectional *in situ* TEM/STEM images captured at selected reaction time for the Si film. The large thickness increase along time can be clearly seen, whereas the increase for the Si-Sn film from *in situ* TEM time-sequence images (Figure

II.I.A.9) is visually less pronounced. The volume expansion of Si is 140% (264 s) and 240% (893 s), while the value for Si-Sn is 158% (136 s) and 230% (408 s). In comparison, it takes around half the time for Si-Sn vs. Si to reach similar expansion, indicating a much faster reaction kinetics in the Si-Sn film. At the end of lithiation (2285 s for Si and 1360 s for Si-Sn), Si and Si-Sn expand to 400% and 266% of its original volume, respectively, suggesting a 34% smaller volume expansion of the fully lithiated Si-Sn film. This is in good agreement with our previous result that the Si-Sn film displays less cracking than the Si film under the same cycling conditions. However, it is worth noting that the Si-Sn film cracks after a few cycles, but it still shows quite stable cycling.

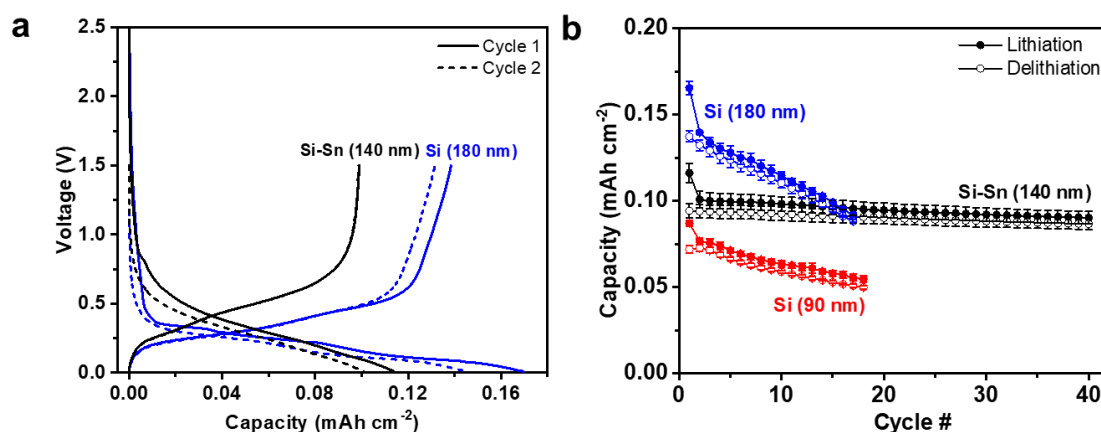


Figure II.I.A.8. (a) Charge-discharge voltage profiles and (b) cycling performance of the Si-Sn and Si films. Error bar shows the standard capacity deviation from three replicate cells.

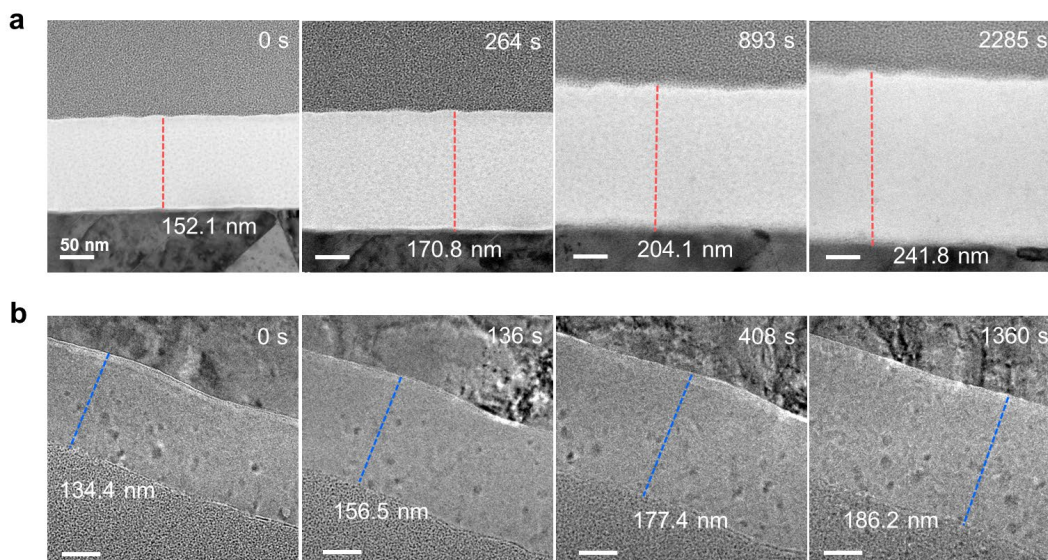


Figure II.I.A. 9 (a) Cross-sectional In situ STEM images of Si film and (b) cross-sectional in situ TEM images of Si-Sn film captured at different time series during lithiation.

Figure II.I.A.10 presents the EELS mapping of the microstructure and elemental distribution of the Si-Sn film at its pristine and fully lithiated states. Before lithiation, the Si-Sn film displays a morphology with branch-like

network (Figure II.I.A.10), where the separation between Si and Sn elements is revealed at nanometer scale. This is expected due to the immiscibility between these two elements. Interestingly, after lithiation, the branch-like morphology disappears and uniform elemental distribution of Si and Sn is seen in Figure II.I.A.10, again consistent with the isostructural nature of the fully lithiated endmembers. Our EELS mapping results reveal the dynamic rearrangement of Sn and Si atoms after the intake of Li atoms, which can be further facilitated given the higher Li diffusivity in lithiated Sn than that in lithiated Si, resulting in the homogeneous elemental distribution after lithiation.

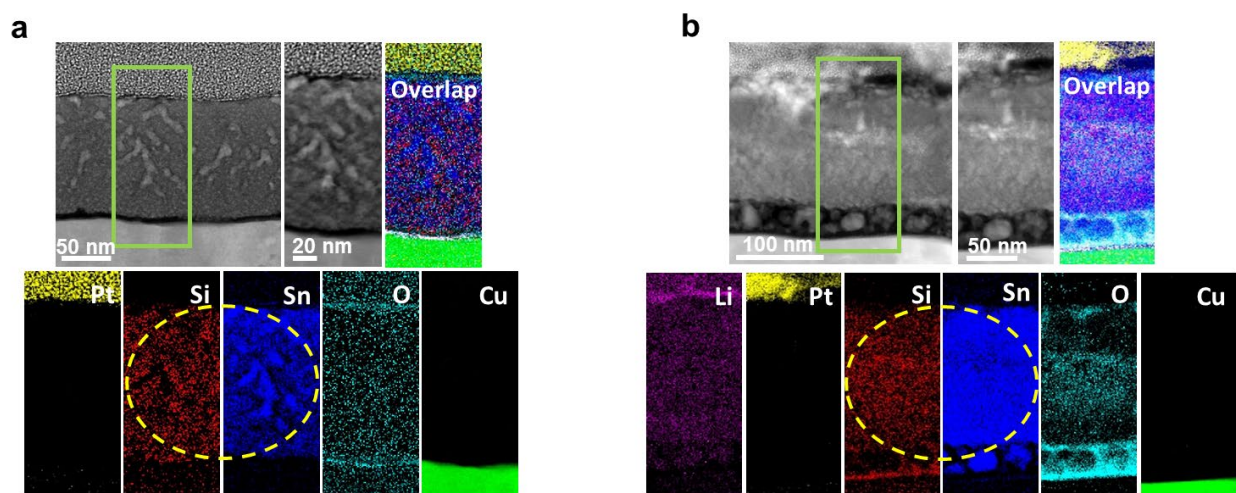


Figure II.I.A.10. EELS mapping of Si-Sn thin film at (a) pristine and (b) fully lithiated states, showing the microstructures and elemental distributions.

As noted by the alternative silicon studies, interfacial control (amorphous carbon, Li-Sn) both yield more stable cycling and appear to have attributes that favor longer calendar life via the addition of species that help maintain electrode homogeneity (lithiation). Based on new research priorities and scaling issues, this film effort is not continuing as part of the Silicon Consortium Program.

Conductive Additives: Numerous efforts in the CAMP Facility were directed to optimizing the silicon composite electrode with conductive additives, such as carbon black (*e.g.* Timcal C45), hard carbon, and graphite (flaky vs. round). In the case of Timcal C-45 carbon, the first cycle Coulombic efficiency of the C45 alone is only 62%, which is also similar to the hard carbon and flaky graphite (SFG-6-L). Another unfortunate side effect of many of these high surface area additives is that they require the use of additional binder to make a robust electrode and may have some catalytic activity towards the electrolyte. In this year the CAMP Facility explored the idea of using inert conductive additives to replace all carbon-based additives. It is hoped that this approach could also enable the use of other binders, and perhaps better control the degree of electrode expansion.

Table II.I.A.1 Volume Resistivity of Alternative Electrode Conductive Additives

Material	Volume Resistivity at 20 °C (Ohm-cm)
Cu	10^{-6}
Carbon	< 0.1
B ₄ C	0.1 – 10
SiC	10^2 - 10^5
SiO ₂	10^{18}

One materials class to consider for inert conductive additives are semiconductors with low band gaps (and low resistivity) that are comprised of earth-abundant elements. Some natural choices include boron carbide and silicon carbide. A comparison of resistivities for common materials are seen in Table II.I.A.1.

Boron carbide has a resistivity that is only slightly higher than carbon & graphite, which are themselves almost five orders of magnitude more resistive than copper metal. In addition, if the semiconductor materials are doped or have crystal defects, their effective resistivity can be made even lower. A range of carbon-free additive materials were selected in this study to scope the effect of resistivity, which include boron carbide, silicon carbon, and silica. Ideally, a metal powder (such as copper or nickel) could be used in this study, but there is a concern that these metal powders could become pyrophoric during processing in the dry room. Silica was selected as a worse-case baseline, where it is expected that the silica additive would block all electrical pathways to the copper foils. Electrodes were designed with an initial concentration of 50 wt.% Si and 40 wt.% inert additives (B₄C, SiC, or SiO₂). Later, an additional boron carbide electrode was designed with 2 wt.% carbon black to create a baseline with higher electrical conductivity. These electrodes were made on the CAMP Facility's pilot-scale reverse-comma coater (A-Pro) with a target capacity of 2 mAh/cm².

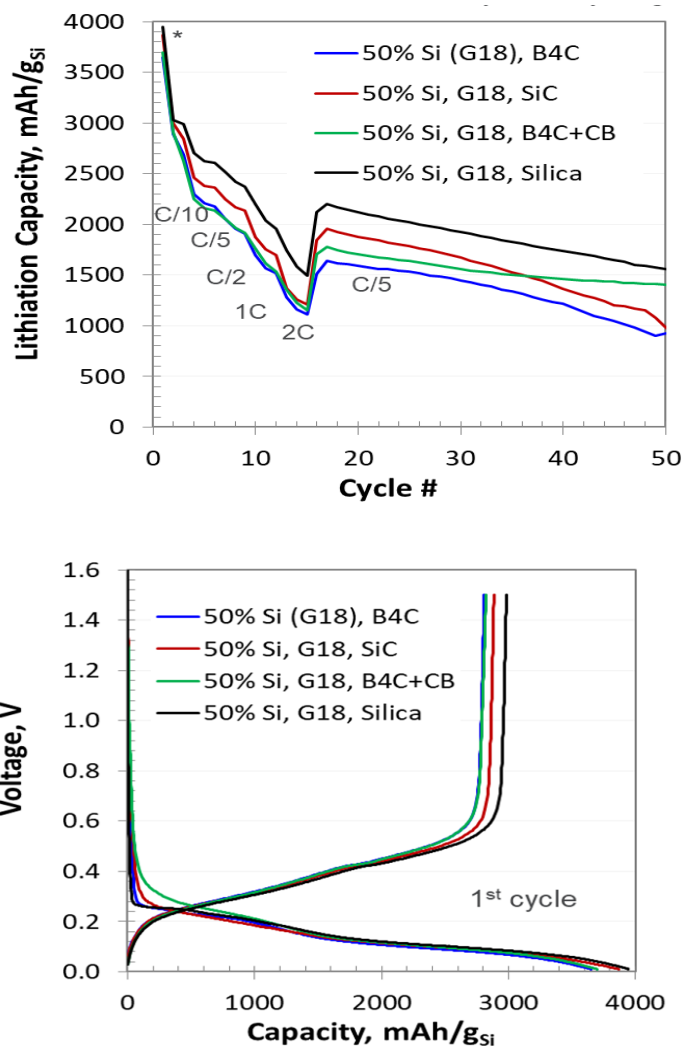


Figure II.I.A.11. Formation cycles (bottom) and Rate & Life cycles (top) for Inert Conductive Additive Study, versus Lithium.

Coin cells were made with these electrodes using lithium metal as the counter electrode and “Gen2F” electrolyte (1.2 M LiPF₆ in EC:EMC (3:7 wt) +10 wt.% FEC). The cells were cycled 3 times at a C/20 rate between 1.5 and 0.01 V for formation, followed by rate tests between 1.5 and 0.05 V, then cycle life test at CAMP Library.

By far, the most surprising observation from this scoping study is that all the cells performed surprisingly well, regardless of the conductive additive. This was especially surprising for the cells that used silica as the inert additive, which were cells made to set the absolute lower boundary for electrically conductive cells. Ironically, the silica cells had the best capacity utilization at all rates, as can be seen from Figure II.I.A.11 – even better than the cells made with boron carbide plus carbon black.

Further testing was done in full cell coin-cells using NMC532 as the counter electrode. These coin cells were tested using the Silicon Deep Dive test protocol (3x C/20, HPPC, C/3 cycling, HPPC, 3x C/20) in a voltage window of 3.0 to 4.1 V (Gen2F electrolyte, 30°C). HPPC protocol used consisted of a charge to 4.1 V, remove 10% capacity, 10 s 3C discharge, 40 s rest OCV, 10 s 2.25C charge pulse, repeat pulse sequence for each 10% DOD. The results of these tests are summarized in Figure II.I.A.12, which includes data from baseline electrodes that consisted of 15 wt.% Si and 80 wt.% Si for comparison. Here too, it is apparent that the choice

in conductive additive had little effect on the capacity utilization and retention during cycling. However, the Coulombic efficiency of the inert additive cells were found to start at a higher level and then decrease toward that of the 15 & 80 wt.% silicon cells.

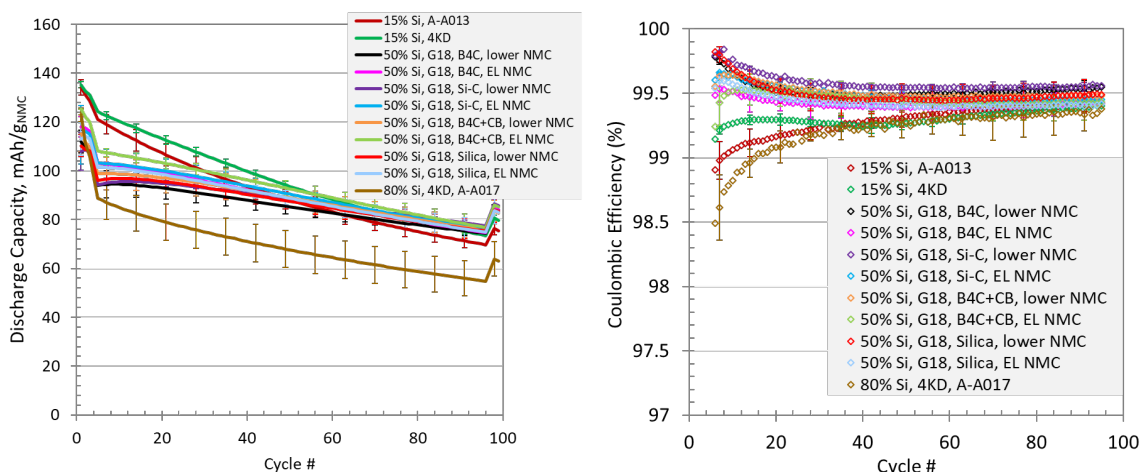


Figure II.I.A.12. Discharge capacities (left) and Coulombic efficiencies (right) for Inert Conductive Additive Study, versus NMC532.

The half-cell and full cell coin cells were opened, along with other older silicon-based coin cells with similar cycling history and similar capacity loading (near 1.9 mAh/cm²). The silicon electrodes were harvested, rinsed with DMC, and the thickness was measured. During the harvesting of many of these cells, it was observed that silicon-based anodes that experienced lithiation near or below 10 mV usually suffered from severe delamination – a situation that often occurred in half cell tests. This was especially true for anodes with high silicon content. Whereas, full cells were designed around a 50 or 100 mV lithiation cutoff, and reference electrode data indicates that the true lithiation potential is over 100 mV for majority of the cycle life. Table II.I.A.2 is a compilation of the thicknesses of the pristine anodes and the harvested anodes (ones that did not show signs of delamination). The harvested (cycled) thicknesses shown in Table II.I.A.2 are focused on anodes from full cells cycled for 100 cycles under the Silicon Deep Dive Protocol (100 cycles) between 3 - 4.1 V at 30°C, with similar n:p ratio.

While it is promising that the initial thickness of electrodes with inert additives (50 wt.% Si) are on par with the electrodes made with 80 wt.% Si, it is clear these cells still swell with cycling. On an optimistic note, the final thickness of the high silicon anodes is still half the thickness of the cycled graphite-only anodes. If the cycle life and calendar life problems can be solved, battery hardware can be designed to accommodate the swelling of the silicon-based cells – although the extra hardware needed will most likely lower the volumetric and mass-specific energy density (and probably increase cost).

Table II.I.A.2 Electrode Thickness of Variety of Pristine & Cycled Anode Electrodes made by the CAMP Facility

Negative Electrode from Full cells (3 4.1V, 100 cycles)	Initial thickness, calendered, μm	Cycled thickness, calendered, μm	% Increase
0% Si, 92% Graphite, 2% C45	41	44	7
5% Si, 83% Graphite, 2% C45	49	54	10
10% Si, 78% Graphite, 2% C45	33	41	24
15% Si, 73% Graphite, 2% C45	28		
30% Si, 58% Graphite, 2% C45	16		
50% Si, 40% B4C	11	21	91
50% Si, 40% B4C, 2% CB	12	20	67
50% Si, 40% SiC	11	21	91
50% Si, 40% SiO ₂	12	22	83
60% Si, 23% Graphite, 2% C45	18		
71% Si, 0% Graphite, 10% C45	9	20	122
80% Si, 0% Graphite, 10% C45	9		

Data in Table II.I.A.2 indicates that there is a dependence of anode swelling on silicon content. This was explored further by plotting the thickness increase (%) versus silicon content, which is shown in Figure II.I.A.13. It was interesting to see a strong linear relationship exists between thickness increase and silicon content, despite the “minor” variations in particle size, morphology, capacity loadings, porosity, binders, and n:p ratio that occurs across these cells over the years. This was not a controlled study, but merely an effort to glean preliminary correlations from existing data. Ideally, this study needs to be redone in a controlled manner where all

components are fixed and the counter electrode is lithium metal, with lithiation of the silicon-based anode limited to a fixed voltage (*e.g.*, 100 mV) or capacity (*e.g.*, 1000 mAh/g).

In summary, it was determined that a new class of composite silicon electrodes made with inert additives such as semiconductor materials (B_4C , SiC) and insulators (SiO_2) performed surprisingly similar to silicon electrodes made with graphite and carbon black - despite the wide range of electrical resistivity. These electrodes were mechanically robust and had thicknesses almost identical to other high-silicon content electrodes. It is time to rethink the importance (or need) of carbon & graphite additives in silicon electrodes. Preliminary investigations also indicate that the anode thickness increase during cycling shows clear linear dependence on silicon content.

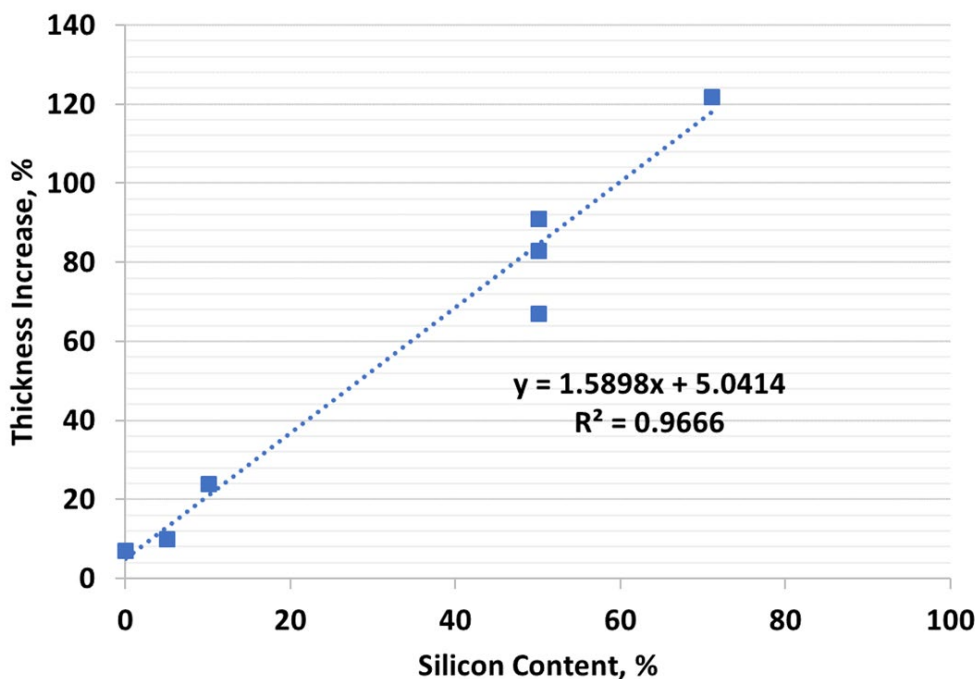


Figure II.I.A.13 Thickness of harvested anodes from full cells cycled under Si Deep Dive Protocol as a function of silicon content.

PAA Binder Processing: Silicon DeepDive and baseline SEISTA electrodes in most cases use a LiPAA-based binder system. It was initially chosen from a survey study based on performance, electrode quality, and consistency. Various adhesive polymers, such as poly(vinyl alcohol), sodium alginate, sodium carboxymethyl cellulose, polyimide, and poly(acrylic acid) (PAA), were evaluated as binders to mitigate the issues associated with the volume expansion of Si during lithiation process. These polymeric binders firmly hold the electrode components together and keep them in electrical contact during electrochemical cycling. After evaluation, a lithium hydroxide (LiOH) titrated PAA (PAA-Li) was chosen as the standard binder for the Silicon Deep Dive program. Although PAA-Li binder has been widely used in laboratory development of Si anodes, multi-lab studies have indicated that protonated PAA had better cycling performance. Discussions have noted that the need for lithiation of the PAA was a conclusion from earlier studies that it was beneficial to the rheological properties of the slurries, such as viscosity and shear thinning (see Figure II.I.A.14), were beneficial to stabilizing electrode slurries and fabricating high-quality electrode laminates, whereas electrodes based on PAA-H showed better performance but had issues associated with homogeneity. This difference is based on that the higher pH

preparation (with LiOH addition) accelerates side reactions at the silicon surface due in part to dissolution of passivating silica. In association with CAMP and ORNL, a method was developed to create a reversible neutralization process that uses ammonia ($\text{NH}_3/\text{NH}_4\text{OH}$) as the neutralizing agent instead of LiOH. Ammonia (NH_3) is a weak base that effectively neutralizes PAA polymer effectively promoting the positive rheological properties of the higher pH processing without degrading the silicon surface.

Characterization of pH adjusted PAA samples was undertaken to assess the role of pH and viscosity, as appropriate viscosity is critical for the electrode manufacturing side to control thickness and loading. [3-7] In these studies, the viscosity of PAA- NH_3 solution was raised to 11.15 Pa·s at 0.2/s, an approximate 30-fold enhancement over protonated (pristine) PAA solution (0.37 Pa·s). The viscosity of PAA- NH_3 solution decreases to 0.84 Pa·s as shear rate increases to 1057/s, indicating strong shear thinning effect. Both the high viscosity and

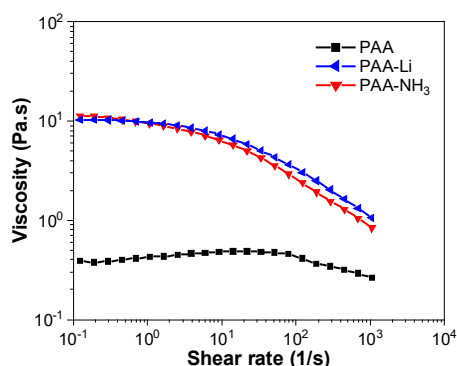


Figure II.I.A.14. Plots of apparent viscosity vs. shear rate for 10 wt% aqueous solutions of PAA, PAA-

the shear thinning effect are beneficial to the slurry processing as they can contribute to slurry stability and facilitate the mixing process, respectively. In addition, unlike the irreversible LiOH-based neutralization protocols, NH_3 neutralization (as NH_4^+ cations) provides a critical feature that restores $-\text{COOH}$ groups. During the standard drying process of the electrodes (e.g., 80 °C, in vacuo), PAA- NH_3 binder can be thermally reversed back to protonated-PAA with removal of NH_3 . Using this technique, the advantages of the higher pH processing can be merged with the benefits of the binding as the protonated PAA form. This unique process is particularly beneficial to maintaining the binding strength of PAA binder for improved cycling performance. ATR-FTIR analysis of electrodes fabricated using PAA, PAA- NH_3 , and PAA-Li binders confirmed the proposed thermal decomposition of PAA- NH_3 binder. The carbonyl peak of PAA- NH_3 electrode overlaps with that of PAA electrode (1750 cm^{-1}). On the other hand, the carbonyl peak of PAA-Li electrode showed at 1630 cm^{-1} due to the irreversible conversion of $-\text{COOH}$ groups to $-\text{COO}^-$ groups. In addition, the adhesive strength of PAA- NH_3 binder is also restored to almost identical to that of pristine PAA binder as evidenced by 180° peeling tests.

Initial proof-of-concept work was demonstrated on 15% Si / 73% graphite formulations. For 70 % silicon electrodes, the electrodes utilized either 20 wt% PAA-Li or PAA-NH₃ binder, or both used 10 wt% C45, conductive additive. Figure II.I.A.15 summarizes capacity retention and coulombic efficiency profiles of half cells, which are subjected to three formation cycles between 0.01 V and 1.50 V at C/20 rate, followed by 100 aging cycles at C/3 rate. As with the 15% silicon cells, the PAA-NH₃ cell formulation outperforms the PAA-Li cell formulation with higher initial capacity, higher average capacity, and better capacity retention. For instance, the average capacity of PAA-NH₃ cell is 1924 mAh/g during the 100 cycles at C/3, which is a 29% increase

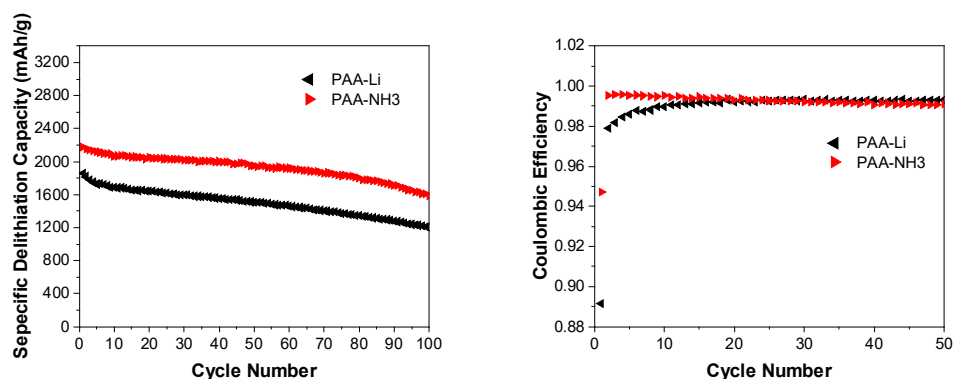


Figure II.I.A.15 Specific delithiation capacity (left) and coulombic efficiency profiles (right) of Li half-cells using electrodes containing 70 wt% Si, 20 wt% PAA-Li or PAA-NH₃ binder, and 10 wt% C45 over 100 cycles at C/3 rate.

compared to PAA-Li baseline (1495 mAh/g). The capacity retention of PAA-NH₃ cell (73%) is also significantly higher than that of PAA-Li cell (64%). The PAA-NH₃ cell shows higher CE than that of PAA-Li cell, especially during the early state of aging cycling. For example, the initial CE of PAA-NH₃ cell is 94% while the initial CE of PAA-Li cell is only 89%. Overall, the reversible PAA-NH₃ binder system provides both enhanced rheological properties as well as significant improvements in cycling performance for high silicon-loading electrodes.

Additionally, the reversibility feature can also be utilized to construct the **in-situ cross-linkable binders** for high silicon-content electrode that should be more robust and better able to withstand the cycle upon cycle volume changes. While mixtures of PAA and PEI (poly(ethylene imine), a linear polymer with nitrogen atoms in the backbone) immediately crashes out from solution upon mixing due to the ionic cross-linking reaction, this precipitation can be inhibited by the PAA-NH₃ reversible neutralization process that blocks the cross-linking. This compatibility allows one to create PAA-NH₃ / PEI solutions. After the thermal decomposition of PAA-NH₃ species during the drying process, the restored PAA binder then cross-links with the PEI via physical cross-linking as well as covalent cross-linking. The in-situ cross-linking mechanism between PAA and PAA-PEI films was confirmed by ATR-FTIR analysis.

The cross-linked material, a reinforced version of the standard PAA system used, was evaluated using 70% Si electrodes fabricated using PAA-Li and PAA-PEI binder systems against matched NMC622 cathodes. Half-cells were cycled between 0.01 V and 1.50 V for three formation cycles at C/20 rate, followed by 100 cycles at C/3 rate. The full cells were cycled between 3.0 V and 4.2 V using a standard cycling protocol including three formation cycles at C/20 rate, a Hybrid Pulse Power Characterization (HPPC), 92 cycles at C/3 rate, another HPPC, and finally three cycles at C/20 rate. As shown in Figure II.I.A.16 PAA-PEI cell shows dramatic improvements in cycling performance compared to PAA-Li baseline. In a half-cell, the average capacity of PAA-PEI cell during is 2091 mAh/g, a 40% increase to our baseline PAA-Li cell (1495 mAh/g) after 100 cycles. PAA-PEI cell also delivered a remarkable 90% capacity retention, 26% higher than PAA-Li baseline. For full cell evaluation, PAA-PEI –based electrodes yielded an average capacity of 125 mAh/g at C/3 rate with a capacity

retention of 70%, a 52% increase in average capacity and a 14% increase in capacity retention compared to the PAA-Li baseline system.

The morphology of Si electrodes fabricated using PAA-Li and PAA-PEI binders was studied by scanning electron microscopy (SEM). Figure II.I.A.17 summarizes the surface SEM and cross-sectional SEM images of PAA-Li and PAA-PEI electrodes before and after aging cycles. All cycled electrodes were fully delithiated before collecting for SEM measurements. After aging cycles, obvious cracks were found on the surface of PAA-Li electrode. The integrity of PAA-PEI electrode is much better than that of PAA-Li electrode with no obvious surface cracks. The cross-section SEM images of these electrodes before and after aging cycles were collected to investigate the volumetric changes of these electrodes. As shown in Figure II.I.A.17, PAA-Li electrode shows a 52% increase in thickness after aging cycles, while PAA-PEI binder had a volume expansion of only 10%. The SEM analysis indicates the excellent binding performance of PAA-PEI binder compared to PAA-Li baseline.

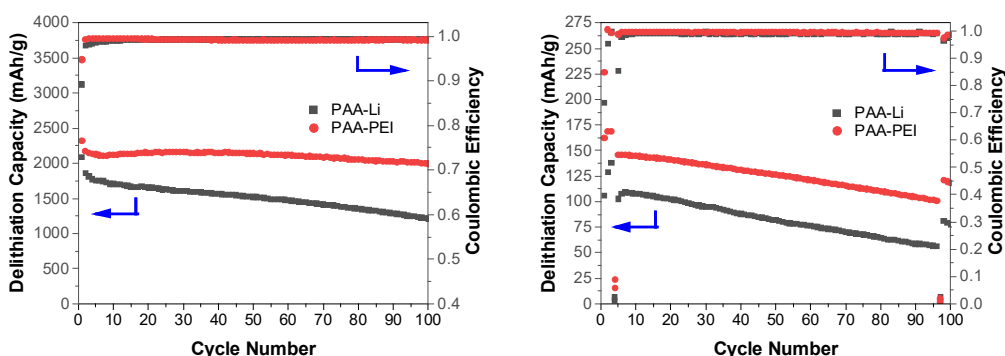


Figure II.I.A.16 Specific delithiation capacity and coulombic efficiency profiles of Li half-cells (left) and NMC622/Si full cells (right) using electrodes containing 70 wt% Si, 20 wt% PAA-Li or PAA-PEI binder, and 10 wt% C45 over 100 cycles.

PAA Binder Modifications: While the modified PAA-NH₃ or PAA-PEI systems both show improvement over baseline based on a mechanism that modifies the binding of the polymer to the surface of the silicon. In both cases the binding is mainly thru the carboxylic acid group, while in the case of the PAA-PEI system the added PEI plays the role to constrain the volume expansion of the polymer to help maintain internal contacts. A different pathway to modifying the surface-polymer interaction is to partially esterify the PAA to make an esterified PAA (termed E-PAA) as seen in Figure II.I.A.18. Specifically, the inclusion of bulky pentyl ester groups that have a minimal ability to hydrogen-bond to the silica surface hydroxyl groups was investigated to tune the surface energy by mediating the number of polymer-surface bonding interactions.

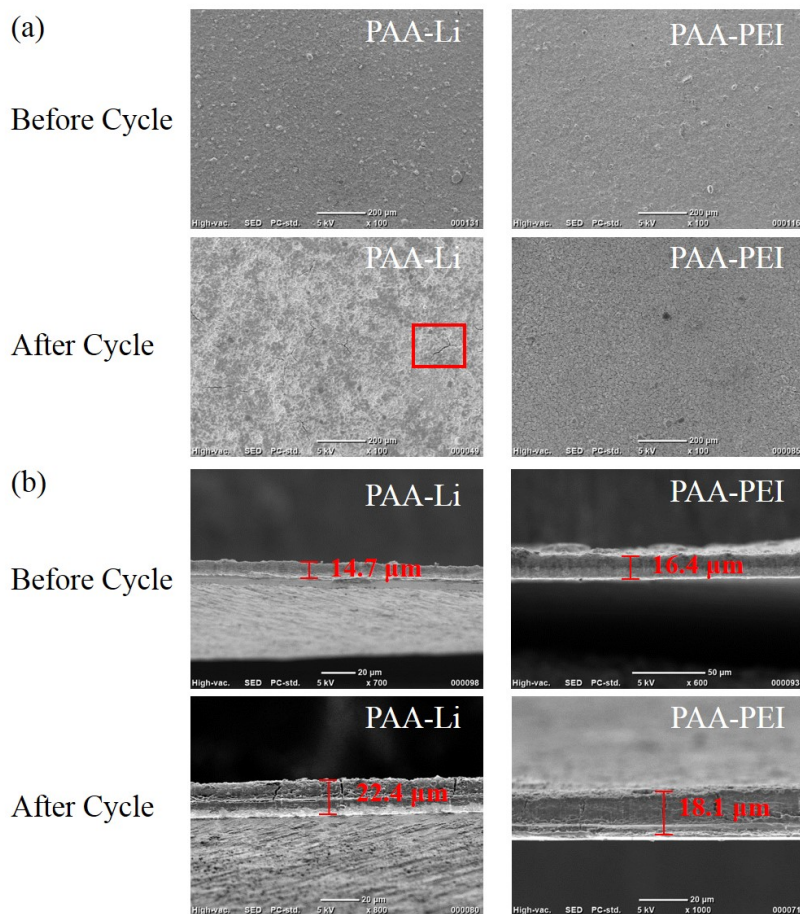


Figure II.I.A.17 (a) Surface SEM images of Si electrodes fabricated using PAA-Li or PAA-PEI binder before and after aging cycles. (b) Cross-sectional SEM images of these electrodes before and after aging cycles.

Using a polished silicon wafer as a model substrate, the measured de-bond energies between Si and PAA were measured using both the native-oxide SiO_x -termination surface and an SiH_x -terminated surface. The de-bond energies were measured using the cantilever beam test (CBT) methodology. The data (in Figure II.I.A.19) show that the SiO_x -terminated Si wafers have a higher de-bond energy than the SiH_x -terminated wafer surfaces, consistent with the stronger surface bonding interaction expected for the hydroxyl terminated surface in contrast to the weaker hydrogen bonding forces that dominate for the hydride terminated silicon.

was increased from 25 to 100 °C (Figure II.I.A.17, left column). In the second experiment, spectra were collected while the E-PAA was held at 100 °C for 24 h (Figure II.I.A.20, right column). We have made two key observations:

- *Esterification alters the conformation of the polymer, increasing stability* The *cis* polymer backbone chain conformation reacts and breaks down while the *trans* conformation not undergo thermally induced reactions.
- *PAA crosslinking occurs via both dehydration and decarboxylation to form ether groups* the reaction products from two *cis* carboxylic acids (–COOH) that combine are one ether linkage (C–O–C) formed via dehydration and decarboxylation.

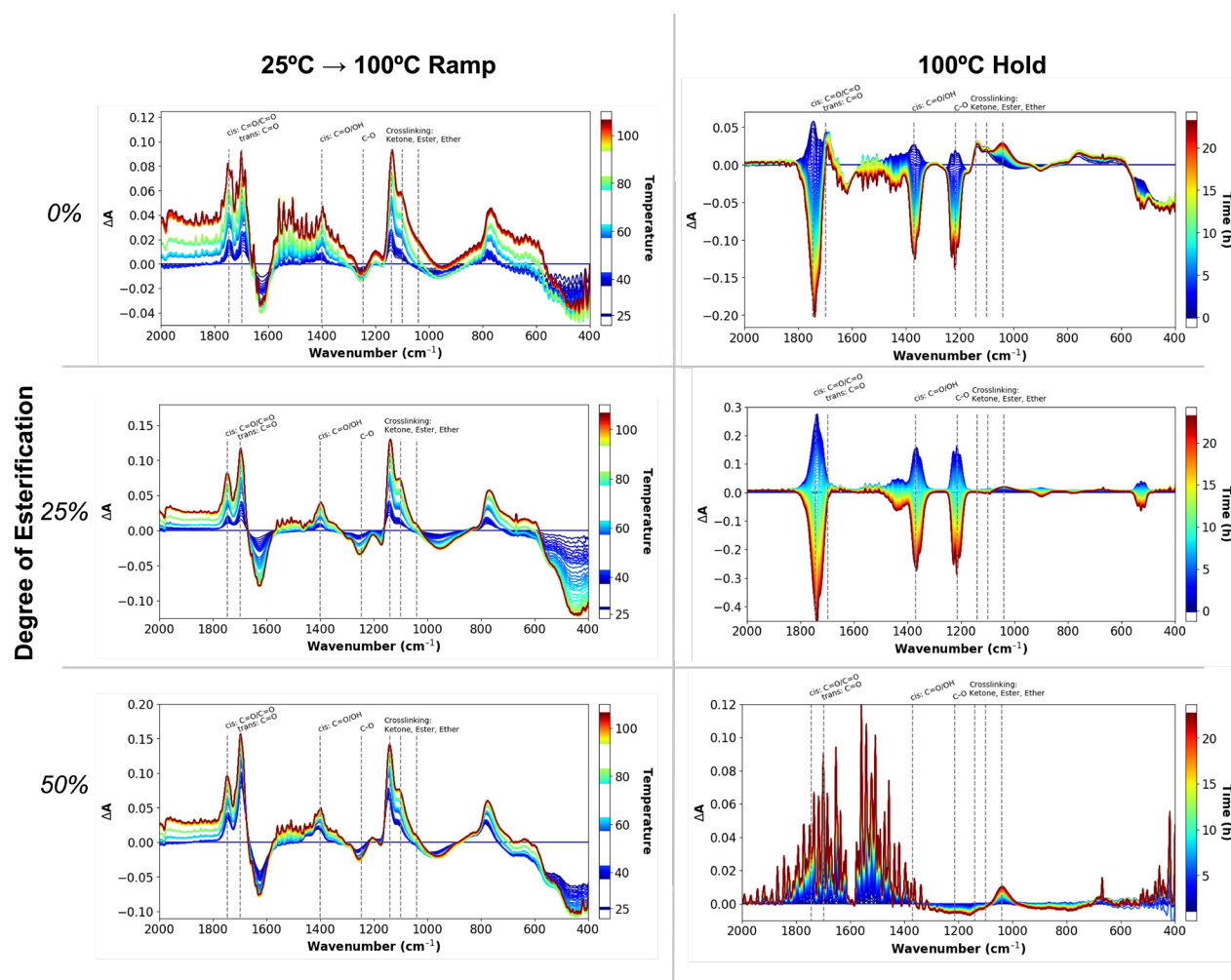


Figure II.I.A.20. Temperature-dependent FTIR measurement of the esterified polyacrylic acid (E-PAA) binder drying. The left column panels show the spectra while heating from 25 °C to 100 °C while the right column panels depict spectra while holding at 100 °C for 24 h. The top, middle, and bottom panels correspond to 0, 25 and 50% ester sidechain, respectively. The first spectrum (25 °C, atmospheric pressure) is subtracted from each spectrum to produce the difference spectra shown.

This PAA reactivity under drying conditions has mechanistic implications for the optimizing the binding strength to the Si surfaces as well as the mechanical properties of composite electrodes. Since previous studies had shown that the wafer studies were an acceptable surface model for Paraclete systems, similar reactivity between Si–OH groups that terminate SiO₂ surfaces results in similar reactivity to give bound silyl ether moieties.

As the addition of pentyl groups to the polymer backbone weakens the overall binder polymer-surface bonding strength, we evaluated the effects of weakening this interfacial interaction on the electrochemical performance using materials beyond the 20% esterification previously evaluated. Figure II.I.A.21 shows the electrochemical cycling performance of electrodes made with PAA, E-PAA esterified to 25% and 50% pentyl groups. This differs from the PAA-PEI studies noted previously in that that study focused not on the binder-silicon interface but the flexibility and volume expansion limits of the polymer after surface bonding. The PAA-pentyl modified electrodes were fabricated using Paraclete Si NPs, the (E-)PAA binder, and Timcal C65 conductive carbon in an 80:10:10 wt% ratio, respectively. The slurry was processed in water and deposited on copper mesh foil and assembled into half-cells using Gen2F electrolyte. Three formation cycles at C/20 were performed, following by cycling at C/5. As is shown in Figure II.I.A.21, the capacity of the PAA electrodes is lower than that of the electrodes made with higher content E-PAA, although all of the samples in the study have capacities significantly below theoretical capacity, indicative of poor utilization and may reflect issues with electrode processing and formation.

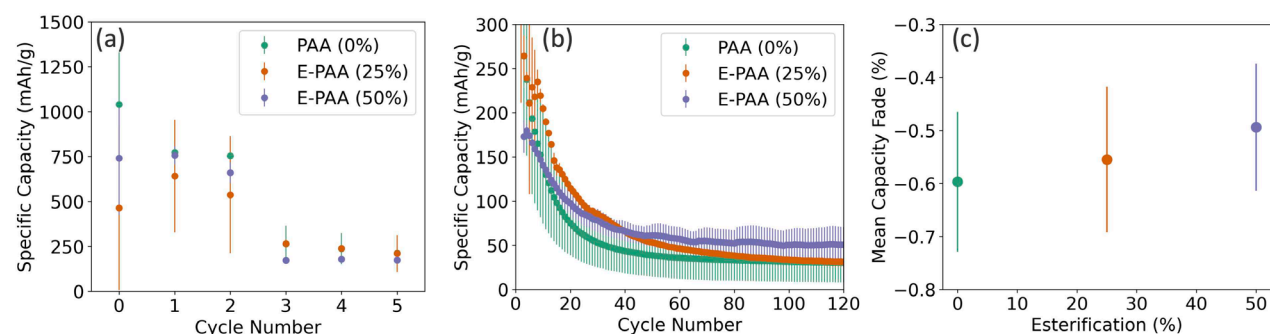


Figure II.I.A.21. Electrochemical cycling performance for Paraclete Si, (E-)PAA binder, and Timcal C65 conductive carbon electrodes (80:10:10 by wt%) in half-cell configuration with Gen2F electrolyte. (a) First 6 cycle specific capacity, (b) full cycle specific capacity, and (c) mean capacity fade as a function of degree of esterification, where 0% esterification is PAA.

The corresponding calendar lifetime test on the same electrodes also was conducted. A voltage hold at 100 mV vs. Li/Li⁺ was conducted following the three formation cycles. Figure II.I.A.22 shows that the different binders had the opposite effect on performance where the electrode made with E-PAA 50% exhibits a larger parasitic current than that with PAA. As previously noted, since the E-PAA binder has a lower binding strength to the SiO₂ surface of Si, we hypothesize that this provides more pathways for the electrolyte to react with the charged Si surface and that PAA-PEI denser polymers may be a better additional pathway to enhance electrochemical properties at the electrode level. In summary we find that the bonding of the binder polymer to the silicon surface needs to be strong and enhanced for both cycle and calendar life studies, especially in instances where the surface may be unstable towards gradual interfacial dissolution or the build-up of breakdown products.

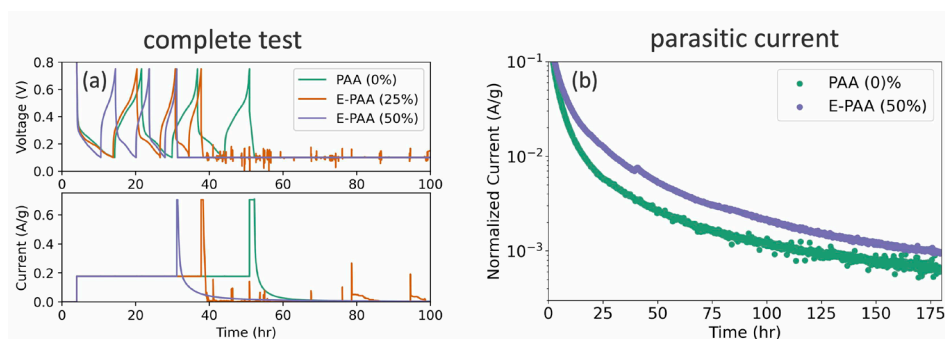


Figure II.I.A.22. Calendar lifetime test for Paraclete Si, (E-)PAA binder, and Timcal C65 conductive carbon electrodes (80:10:10 by wt%) in half-cell configuration with Gen2F electrolyte. (a) Voltage and current profiles as a function of time for PAA, 25% E-PAA, and 50% E-PAA samples. Note data beyond 100 h is not show. The 25% E-PAA sample did not exhibit meaningful cycling data and was removed from analysis. (b) Normalized parasitic current for the 100 mV voltage hold portion of the data following the 3 formation cycles shown in (a).

Using in-situ spectroelectrochemistry, the PAA and E-PAA polymer interactions were probed with respect to cell cycle and calendar lifetime. Here, we used the same Paraclete/(E-)PAA/C65 electrodes as above deposited on a Cu mesh electrode and placed this electrode directly onto an attenuated total reflectance Fourier transform infrared (ATR-FTIR) diamond crystal. Gen2 electrolyte, a Celgard separator, and lithium metal counter electrode were placed successively onto the Si NP/Cu mesh electrode. The stack was compressed with a stainless-steel plate and sealed from air. A 9-h OCV hold was performed, followed by 3 formation cycles at $C/20$, and either a $C/5$ sweep to 100 mV vs. Li/Li^+ (cycle lifetime test) or a voltage hold at 100 mV vs. Li/Li^+ for 160–180 h. An astounding amount of insight can be gained from the spectroscopic data over the course of these experiments.

FTIR data for the 9-h OCV hold is shown in Figure II.I.A.23 for electrodes made from PAA and E-PAA (50%) samples. The spectra are markedly different, with the E-PAA (50%)-based electrode swelling with significant amounts of electrolyte throughout the entire OCV hold. In contrast, the PAA-based electrode exhibits a minor amount of electrolyte swelling. Further, the PAA-based electrode appears to preferentially exclude free EMC solvent (i.e., not coordinated to a Li^+) while at the same time showing infiltration of PF_6^- anions. These results are consistent with the solvated $\text{Li}^+[\text{PF}_6^-]$ salt as calculated by the Persson group calculations that shedding *some*

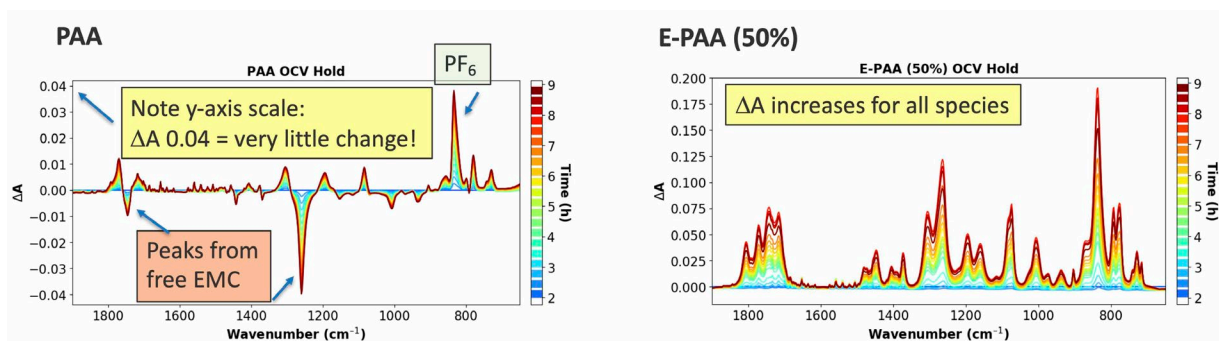


Figure II.I.A.23 Spectroelectrochemical data using in situ ATR-FTIR spectroscopy of 9-h OCV hold. Electrode is made from Paraclete/(E-)PAA/C65 deposited on a Cu mesh electrode with Gen2 electrolyte in half-cell configuration.

of its carbonates that help solvate the salt in bulk electrolyte, and indicate that the number of carbonates coordinating each Li^+ , typically between 4–6 in solution [8,9], is reduced substantially upon entering the PAA-based film. Similar conclusions are obtained from the first [cycles between 100 and 750 mV vs. Li/Li^+ (data not

shown). We conclude that PAA, because of its decarbonylation-induced polyether moieties behave like an ionically conducting material. In contrast, E-PAA behaves as an electrolyte-conducting material.

Next, we present FTIR data for 100 mV vs. Li/Li⁺ voltage hold experiments that mimic the calendar life test for electrodes made from PAA and E-PAA (50%) samples. These 160–180 h voltage holds reveal the electrolyte and SEI speciation that is changing under prolonged polarization at lithiation potentials. As shown in Figure II.I.A.24, spectra for both electrodes exhibit broad, new peaks at 1650–1600 cm⁻¹ and 1450–1400 cm⁻¹ (dashed vertical lines) that grow in over the course of the experiments and are assigned to a heterogeneous mixture of lithium alkylcarbonates. Despite this similarity in the organic SEI component, significant differences also are found. The electrolyte in the E-PAA (50%)-based electrode changes in composition slightly, but the overall electrolyte volume in the film (i.e., the degree of liquid electrolyte present from swelling) does not change significantly. In contrast, the PAA-based electrode shows that all electrolyte peaks decrease dramatically during the voltage hold as the electrode expunges significant electrolyte during the voltage hold possibly due to phases formed during the parasitic reactions clogging electrode pores. This overall picture agrees with the higher parasitic current that is found with the E-PAA-based electrode (Figure II.I.A.24), where it's more compliant nature and proclivity to swell with electrolyte results in an easier pathway for electrolyte to access the Si surface, resulting in a higher parasitic current and, ultimately, a shorter calendar lifetime. This is consistent to the PAA-PEI study where crosslinking induced densification of the binder at the interface appeared to be beneficial to the cells performance.

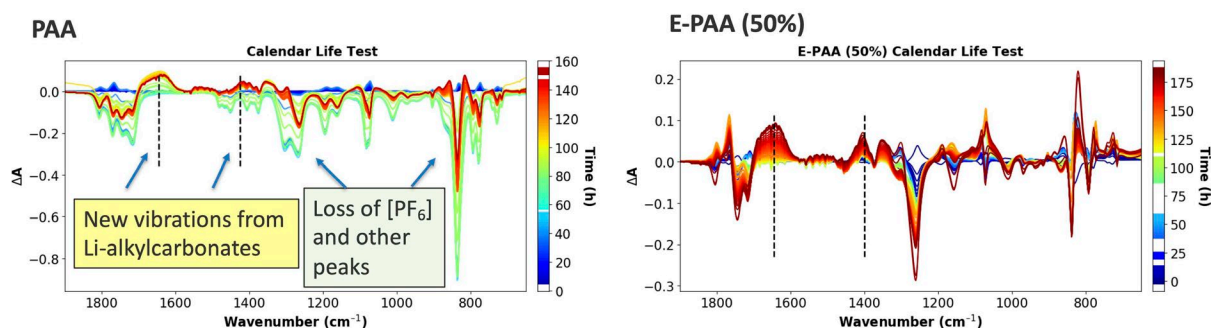


Figure II.I.A.24. Spectroelectrochemical data using in situ ATR-FTIR spectroscopy of 100 mV vs. Li/Li⁺ that mimics the calendar life test. Electrode is made from Paraclete/(E-)PAA/C65 deposited on a Cu mesh electrode with Gen2 electrolyte in half-cell configuration.

For these three PAA studies, we can conclude that 1) the processing pH is important for maintaining the integrity of the silicon surface as too high a pH is likely to dissolve the interfacial silicon surface, (2) maximizing the connectivity of the PAA to the silicon surface has been found to enhance calendar life studies, and (3) increasing the conductivity and density of the polymeric PAA binder by addition of a PEI polymer at time of surface attachment was found to limit electrode volume expansion and lead to enhanced performance.

BatPaC Model: Our calculations have shown that achieving the project-wide Si Deep Dive Q4 Milestone to: “Combine and assess the advancements made over various aspects of the silicon electrode by the Silicon Deep Dive team (Binder/Silicon/Electrode Formation/in-situ Coatings/Electrode-level Failure Mechanisms) and optimize a best full cell with a commercial cathode that using BatPaC can be determined to deliver > 350 Wh/kg” will require a silicon-based anode >500 mAh/g and ideally approaching 1000 mAh/g capacity (data not shown). We have made significant progress toward this goal using a new, surface engineered Si active material with a multivalent surface substitution. Combining the knowledge from the binder studies with optimized solvent and drying temperature conditions with this new surface engineered Si, we have achieved high >99.5% coulombic efficiencies after the first few cycles and stabilized specific capacities of ~800 mAh/g in half-cell configuration. The data are presented in Figure II.I.A.25 (red and black data points) not only meet the Q4 Milestone, but critically point a pathway toward further electrode optimization using surface engineering strategies.

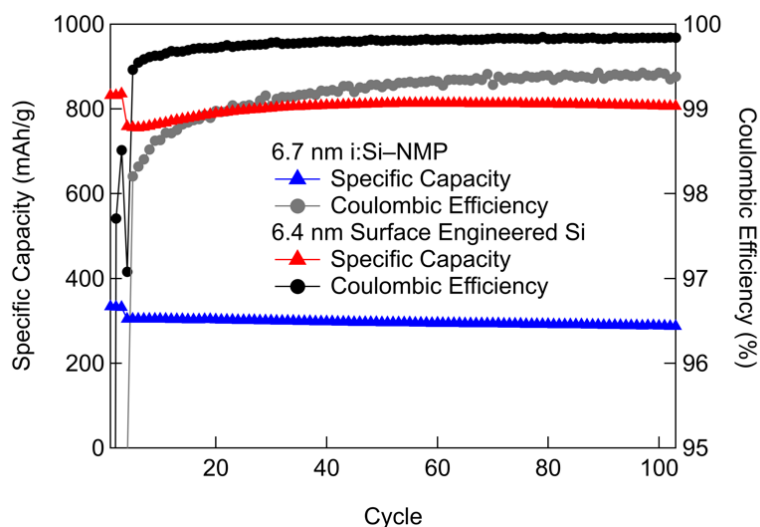


Figure II.I.A.25. Comparison of half-cell electrochemical performance of the baseline electrode containing intrinsic Si NPs coated with N-methylpyrrolidone (i:Si-NMP) active material and PAA binder (blue and grey) with an electrode containing a new, surface-engineered Si active material and PAA binder.

Electrode Formation: While often investigated as individual components, electrochemical cells are a complex balancing act of numerous materials in the form of electrodes, electrolytes, and balance of plant issues (i.e. cell stack pressure). A critical multi-component piece of an electrochemical cell is the actual electrode. The electrode is a complex mixture of engineered active materials, binders, conductive additives and metal foil current collectors. The processing of these pieces to make a porous and active electrode is an art requiring trials and conditions. At many levels electrode processing is a crucial component of materials evaluation as understanding the various surface-interfacial interactions may not always be known ahead of time. Composite silicon- graphite anodes, fabricated with poly(acrylic acid) or lithium neutralized poly(acrylic acid) (LiPAA), were shown to have preferential adsorption of PAA or LiPAA on graphite or silicon due to surface interactions. With this information, the processing requirements and optimization parameters for PAA and LiPAA polymeric binders were explored for high silicon content anodes where both PAA and LiPAA-based electrodes were fabricated. Within this effort, we sought to identify and characterize the role of electrode processing since the fabrication method directly effects electrode architecture, homogeneity, and performance. Our research pathway was to add small molecular weight polymers as dispersants into the slurry to probe their utility to stabilize the slurry structure and see how that translates to a more homogeneous silicon/ graphite electrode architecture.

The mixing and processing protocols used were developed and characterized in conjunction with the CAMP facility at Argonne. With this data, the influence of slurry homogeneity on the physical and structural chemistry

(from nano to micron length scales) of the binder system was ascertained. The goal of these studies is to develop Si-based slurries that lead to higher levels of electrode homogeneity not only on the surface of the electrode, but throughout the bulk. The binder-processing combinations were selected as these baseline materials and methods are currently utilized in the CAMP facility at Argonne. The PAA used was processed with either planetary centrifugal mixing (PCM) or a ball milling (BM) method to increase the surface area and speed dissolution. Because these two mixing methods have different energies associated with them, they could alter the binder structure and electrode slurry interactions, leading to variability in electrode homogeneity (i.e. sedimentation) after casting. [10-15] Additionally, the sedimentation rates and the flow behavior of the slurry produced can be altered by the addition of a low molecular weight dispersant to the electrode slurry. To understand the role that chemistry and processing have on the PAA binder-Si laminate combinations and eventual electrode architecture, two characterization techniques that are sensitive to the length scales and porosity produced were utilized, namely x-ray nano-tomography and ultra-small angle neutron scattering (USANS). X-ray nano-tomography was used to probe the electrode architecture of high silicon content anodes. Given that the signal strength from X-ray techniques is tied to the atomic number of the sample, traditional binders like PAA and LiPAA will provide poor contrast against the electrode silicon. To enhance the signal strength, Cs was substituted for Li in the mixture resulting in a binder with significant electron density suitable for X-ray nano-tomography.

X-ray nano-tomography data were collected on a cast electrode without exposure to electrolyte. A triangular shaped portion of the electrode, shown in Figure II.I.A.26 (column 1), was removed from the center of the cast and used for the experiment. Figure II.I.A.26 shows an intensity color map of the electrode made with planetary centrifugal mixing (PCM) mixed CsPAA without dispersant (Figure II.I.A.26, row 1), ball milled (BM) CsPAA without dispersant (Figure II.I.A.26, row 2), PCM mixed CsPAA with dispersant (Figure II.I.A.26, row 3), and BM CsPAA with dispersant (Figure II.I.A.26, row 4). Red indicates the densest areas of Cs^+ , while blue indicates the most dilute areas of Cs^+ , which are assumed to be silicon-rich areas. It should be noted that carbon black is likely mixed in these areas, which would further dilute any signal from Cs^+ or silicon. However, the extent of carbon black mixing is difficult to probe since it cannot be imaged in the X-ray due to its low atomic number and low crystallinity. This is because silicon produces a detectable signal in the X-ray while carbon black does not, thus, the blue areas are assumed to be silicon rich. There appears to be “black holes” in some areas of the electrode. This is attributed to the surface roughness of the electrode. Comparisons can be made between electrodes due to the same normalization process applied to all electrodes.

To quantify the electrode homogeneity as a function of depth in the electrode, 37.4 nm slices were analyzed and the concentrations of silicon and Cs^+ determined. Qualitative analysis reveals clear evidence for Cs^+ segregation in the electrode with PCM blended binder with no dispersant added as indicated by the blue regions on the surface of the electrode and yellow and red regions on the interior of the electrode. Since silicon has a longer attenuation length than Cs^+ (approximately 100 μm compared to 22 μm for Cs), the blue areas are assumed to be silicon rich and consequently CsPAA binder poor regions. Yellow regions are due to more dilute areas of Cs^+ where silicon is mixed with CsPAA thus diluting the signal from the Cs^+ , while the red region corresponds to the highest Cs^+ concentration. The electrode depth was plotted as a fraction of the most prevalent species, based on the area within each slice corresponding to the different CsPAA concentrations and is presented in Figure II.I.A.26, insets, when the data show two or more species in each layer,

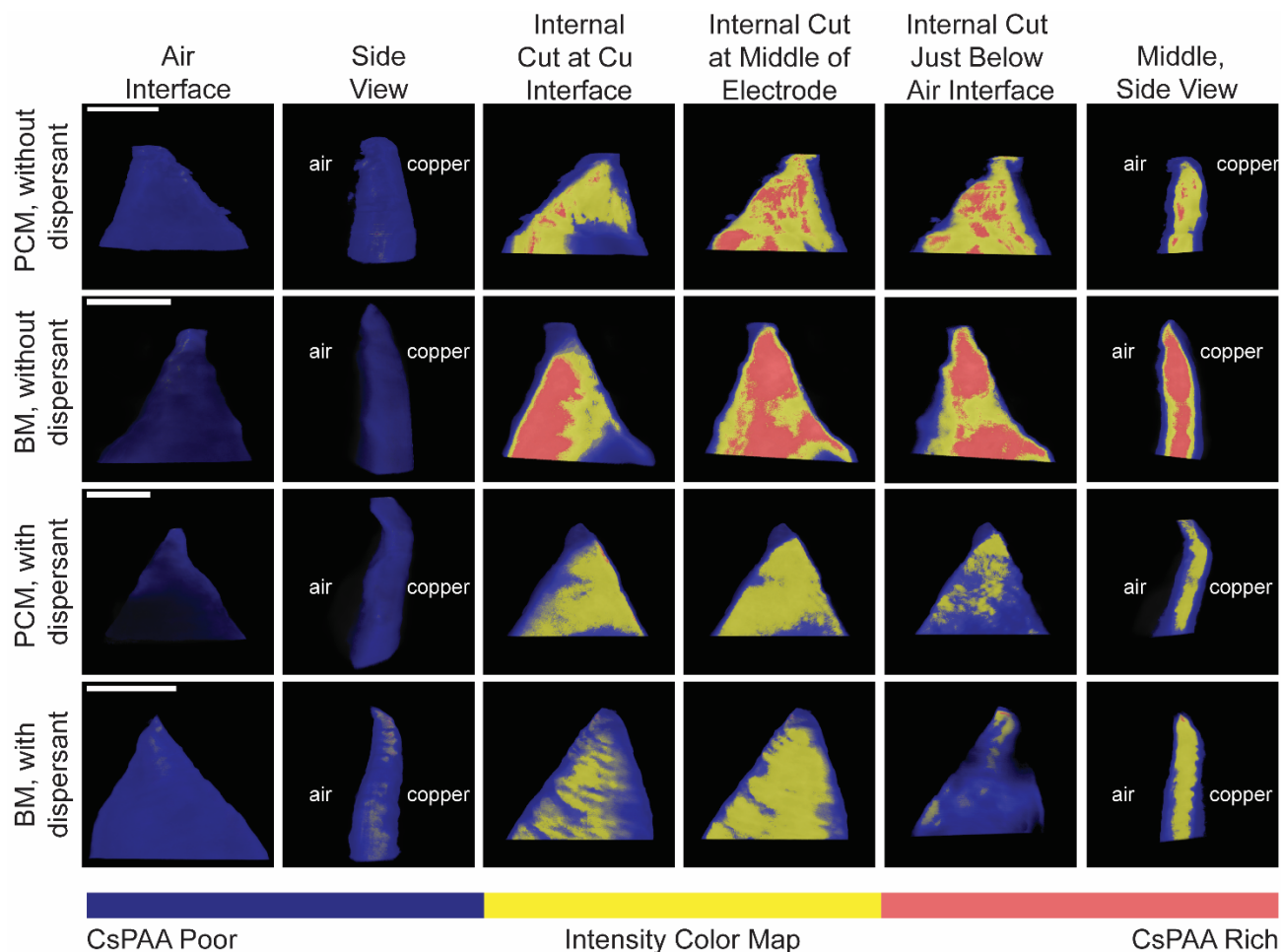


Figure II.I.A.26: X-ray nano-tomography slices of electrodes made with PCM binder without dispersant (row 1), BM binder without dispersant (row 2), PCM binder with dispersant (row 3), BM binder with dispersant (row 4). Each column represents a slice of the electrode at a certain location from left to right: (1) surface of the intact electrode at the air interface, (2) side view of the surface of the intact electrode where the air interface is on the left and the copper interface is on the right, (3) internal structure as the electrode is sliced at the copper interface toward the air interface, (4) internal structure at the middle of the electrode, (5) internal structure at the air interface, (6) side view of the internal electrode sliced at the middle of the electrode. The color intensity map at the bottom of the figure shows that CsPAA poor areas are depicted by blue while CsPAA rich areas are depicted by red. All scale bars are $100\ \mu\text{m}$ and located in the top left corner.

this indicates increasing lateral heterogeneity, the percent of each species is represented as percentage in the horizontal axis. The top of the vertical axis corresponds to the air interface while the bottom (deeper) corresponds to the copper (current collector) interface.

From these data analysis the electrode appears heterogeneous as the binder contains a different distribution of electron density as a function of depth. This is an artifact of the analysis as silicon, and potentially carbon black is likely intermixed throughout the entire electrode since it comprises 80 wt% (71.5 vol%) of the total electrode albeit again with varying concentrations of CsPAA. Blue pixels correspond to areas with the least amount of CsPAA, appearing as bands from the air interface at $0\ \mu\text{m}$ to $13\ \mu\text{m}$ and from $42\ \mu\text{m}$ to $50\ \mu\text{m}$. The majority of the red pixels occur at a depth of $24\ \mu\text{m}$ and corresponds to areas with the most (or highest concentrations) CsPAA. The yellow pixels occur between $10\ \mu\text{m}$ and $42\ \mu\text{m}$ where the majority occurs at $21\ \mu\text{m}$ and $29\ \mu\text{m}$.

From 21-29 μm , the yellow area comprises approximately 60% of the electrode, which indicates that there is more intermixing of silicon in these areas, causing the signal from CsPAA to be dampened. This clearly shows that the most concentrated areas of the binder reside in the middle of the electrode. Additionally, there is probably less silicon in the red areas than in the yellow areas because the Cs signal is not diluted by the lower absorbing silicon.

Representative tomography data for the BM without dispersant electrode is shown in Figure II.I.A.26 (second row). The BM electrode without dispersant contained 50-60% CsPAA rich area (red areas) from approximately 22-34 μm compared to the PCM electrode without dispersant, which contained approximately 22% CsPAA rich area from 22-28 μm . The BM electrode without dispersant likely has ~40% more CsPAA rich areas due to the BM CsPAA having a larger molecular weight or a different polymer chain conformation (i.e. shape) when compared to the PCM CsPAA.

Similar to the PCM electrode without dispersant, the CsPAA rich areas reside in the middle of the electrode (red). However, it is now at a depth of 28 μm (versus 24 μm for the PCM electrode). The silicon/CsPAA intermixed region (yellow) starts at a depth of 6 μm and has a concentration of 15% at 10 μm . This is compared to the PCM electrode without dispersant in which the intermixed silicon/CsPAA areas start at a depth of 10 μm with a concentration of less than 5%. As such, these areas appear as CsPAA rich. The yellow areas are closer to the air interface by 4 μm , the yellow areas only make up 45% of the total concentration of the slice at depths of 18-23 μm and 36-40 μm for the BM CsPAA without dispersant electrode versus approximately 60% at depths of 18-38 μm for the PCM CsPAA without dispersant electrode. This coupled with the 40% increase in the CsPAA areas for the BM CsPAA without dispersant electrode versus its PCM counterpart, indicate that the BM CsPAA electrode is less homogeneous in both the lateral (i.e. along the slice) and z-direction (i.e. thickness) of the electrode. From these analyses we can conclude that the polymer solution preparation and mixing stages strongly influence the final electrode architecture.

Dispersants have been used in these slurries for battery materials to create a more homogeneous distribution of components. [16-19] To explore this effect, an 1,800 g/mol MW CsPAA (i.e. dispersant) was blended with a 450,000 g/mol CsPAA (i.e. binder). This addition to the slurry formulation has a major impact on the resulting electrode homogeneity and cycling performance as shown from the internal images of the electrode in Figure II.I.A.23, row 3. Unlike the electrodes without dispersants, the middle of the PCM electrode with dispersant is dominated (77%) by the well mixed Si/CsPAA (yellow region) with less than 2% of the regions originating the high CsPAA (red) zones. Second, with the exception of a small fraction of the silicon/CsPAA intermixed region (yellow pixels) between 5 μm and 14 μm , the well mixed Si/CsPAA zone does not materialize until 25 μm versus 15 μm for the PCM without dispersant case (Figure II.I.A.27, inset) with the remainder of the electrode dominated by the Si-rich/CsPAA poor species. Since all electrodes were fabricated with the same amount of CsPAA, dispersant causes a laterally more homogeneous distribution of silicon intermixed with binder as evidenced by the absence of the CsPAA-rich region. This shows that, while dispersant causes a laterally more homogeneous electrode, it does not necessarily result in an electrode that is more homogeneous in the z-direction (i.e. thickness of the electrode). This may indicate that dispersant is interacting more with the CsPAA binder and breaking it up rather than cleaving the silicon aggregates. In addition, the PCM electrode with dispersant has a different depth profile when compared to the other electrodes: none of the other electrodes have CsPAA mixed with silicon (yellow) in two distinct bands. These two different CsPAA mixed with silicon bands are likely due to differences in degree of entanglement of the polymer chains.

The results from the BM blended binder with dispersant are shown in Figures II.I.A.26 (last row) and 2D inset. Similar to the previous samples, the highest concentration of Cs is at the center of the electrode (Figure II.I.A.27). However, the slices from 24-44 μm are comprised of approximately 60-80% CsPAA intermixed with silicon

(yellow regions), compared to 60% of CsPAA intermixed with silicon from 18-38 μm for the PCM CsPAA without dispersant electrode, 40% of CsPAA intermixed with silicon from 18-24 μm for the BM CsPAA without dispersant electrode, and 75% of CsPAA intermixed with silicon from 32-38 μm for the PCM CsPAA with dispersant electrode. There are limited CsPAA rich areas and there is a broad band of CsPAA intermixed with silicon making up 60-80% of the slices from 20-44 μm , which indicates that the BM CsPAA with dispersant electrode is the most homogeneous electrode laterally. Similar to the PCM electrodes, adding dispersant to the silicon electrode slurry causes the CsPAA rich regions to become almost non-existent, however, adding dispersant to the electrode causes the majority of the yellow regions to be pushed deeper into the electrode. This also indicates that electrodes made with dispersant are less homogeneous in the z-direction, while being more homogeneous in the lateral direction. This supports the hypothesis that the dispersant is interacting with the binder chains and breaking up those agglomerates rather than interacting with the silicon and cleaving those bound aggregates.

Regardless of whether the electrode contained dispersant or not, there is clear evidence that the binder segregates to middle of the electrode, leaving a silicon rich, binder poor skin on both the air and copper interfaces. This may be contributing to the observed delamination issues noted by the CAMP and Post-Test Facilities in several of the postmortem analysis studies of the program cells. However, the degree of binder segregation depends on if the electrode was constructed using a slurry that contained dispersant and how the binder was fabricated. The data in Figure II.I.A.27 indicates that adding dispersant increases the homogeneity of the electrode causing the CsPAA rich region (red) to disappear, at the expense of driving the majority of the yellow regions deeper into the electrode and away from the air surface. Therefore, adding dispersant to the electrode slurry causes a laterally more homogeneous electrode by better distributing the binder and the silicon (i.e. little to no red regions in the electrodes made with dispersant). However, adding dispersant causes the electrode to be more heterogeneous in the z-direction, meaning that the silicon and silicon/binder areas have separated into a layered-like structure. One of the main questions that this data relates to the possibility of achieving homogeneity in both the lateral and z-direction and its role in electrochemical performance. In order to better probe the silicon/binder and silicon/carbon black interaction and explore the electrode homogeneity in all directions and its effect on electrode properties Raman mapping, X-ray photoelectron spectroscopy (XPS), galvanostatic cycling, and rheology are utilized.

The first lithiation cycle voltage profile is instrumental in understanding the effect the electrode architecture has on electrochemical properties. The voltage versus capacity lithiation and delithiation curves are presented for all electrodes discussed in Figure II.I.A.27. The BM CsPAA without dispersant electrode has a first lithiation voltage profile that resembles a crystalline silicon lithiation profile and shows the crystalline silicon to amorphous silicon transition indicated by the plateau at around 150 mV.[19-21] The PCM CsPAA without dispersant electrode has a similar profile in that it also reaches a crystalline to amorphous silicon transition plateau at 150 mV. However, the capacity of the PCM CsPAA without dispersant electrode is approximately 850 mAh/g compared to the BM CsPAA capacity of 1300 mAh/g. An additional 100 mAh/g is achieved for the BM CsPAA without dispersant electrode upon the voltage hold, bringing its total capacity to approximately 1400 mAh/g. The BM CsPAA with dispersant electrode only a capacity of 400 mAh/g is achieved before 50 mV is reached. However, during the voltage hold at 50 mV, an additional 1225 mAh/g in capacity is achieved, making the total first cycle capacity 1625 mAh/g. The PCM CsPAA with dispersant electrode has the worst first lithiation voltage profile in that only a capacity of 75 mAh/g is achieved until the electrode reaches 50 mV. The final capacity of the PCM CsPAA with dispersant electrode is 1600 mAh/g, indicating that an additional 1575 mAh/g in capacity is achieved during the 50 mV voltage hold. Some of this capacity is likely related to Cs reduction at

0.05V (vs. Li/Li⁺). These last two electrodes don't have the characteristic voltage profile of crystalline silicon indicating poor transport of electrons and/or Li⁺.

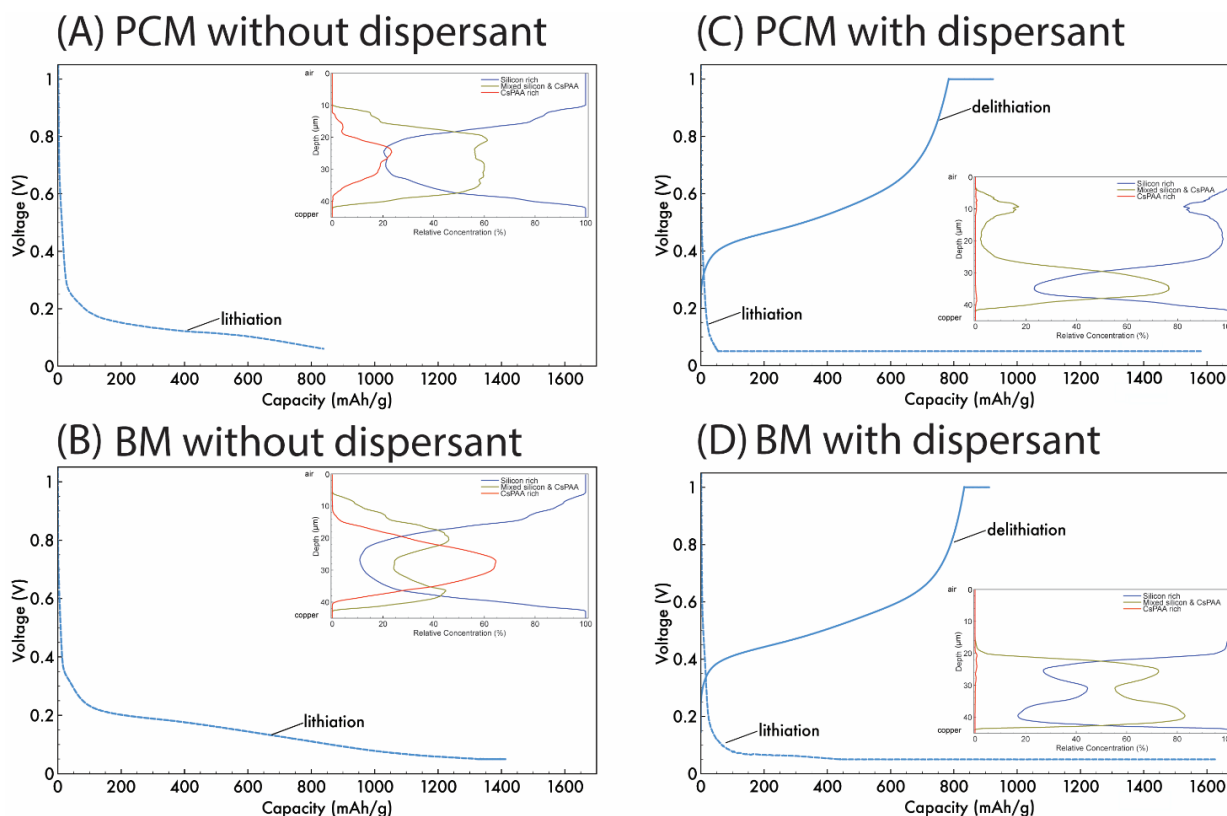


Figure II.I.A.27: First galvanostatic cycle presented as voltage versus gravimetric capacity for electrodes made with Planetary Milled (PCM) blended CsPAA (A) without and (C) with dispersant and Ball-Milled (BM) CsPAA (B) without and (D) with dispersant. Electrodes made with dispersant (C and D) completed a full lithiation/delithiation cycle while electrodes made without dispersant (A and B) only completed a lithiation cycle. Insets are the relative concentration of silicon-rich/CsPAA binder poor regions (blue), intermixed silicon and CsPAA binder regions (yellow), and CsPAA binder rich/silicon-poor (red) as a function of depth in the electrode where the two extremes are at the electrode-air interface and at the silicon-copper interface for electrodes made with (A) PCM CsPAA without dispersant, (B) PCM CsPAA with dispersant, (C) BM CsPAA without dispersant, and (D) BM CsPAA with dispersant.

From Figure II.I.A.27, it seems that adding dispersant to the electrode causes an enhancement of the layered aspects of the electrode structure, which results in an electrode with more lateral homogeneity. This is consistent with the homogeneity (z-direction) through the thickness of the electrode is more important than lateral homogeneity (x-y plane) in determining how ideal the voltage profile is and may be related to connectivity to the current collector or overall stability to delamination. While the electrodes with dispersant had higher overall capacity coming from the voltage hold, 75% for the BM CsPAA with dispersant or 95% for PCM CsPAA with dispersant electrode, respectively. This shows that there is a fundamental lithium and/or electronic transport problem in the electrodes with dispersant. Since Cs⁺ has a reduction potential of 100 mV vs. Li⁰/Li⁺, and the minimum cut off voltage was 50 mV, the focus of the electrochemical study was on the first cycle lithiation/delithiation voltage profile. [22]

To investigate the possible change in binder structure, a series of dilute (0.25-2 wt%) solutions of each binder were used to determine the intrinsic viscosity, and thus the molecular weight, using an Ostwald viscometer. [23-

43] Viscometer measurements showed that the molecular weight of the BM and PCM CsPAA had average molecular weights of 59,208 g/mol and 56,638 g/mol, respectively (Table 1). Note, Ostwald viscometry provides average molecular weight, not molecular weight distribution.

The higher molecular weight BM CsPAA can explain why the electrode slurries made with BM CsPAA have higher viscosities (26.58 Pa*s and 33.01 Pa*s for slurries with and without dispersant, respectively) than that of PCM CsPAA electrodes (19.27 Pa*s and 24.10 Pa*s for slurries with and without dispersant, respectively). However, the electrodes, irrespective of mixing method, made with dispersant consistently have a lower viscosity (difference between with and without dispersant being 6.4 Pa*s and 4.8 Pa*s for BM and PCM mixed CsPAA electrodes) than their counterparts made without dispersant (Figure II.I.A.27 and Table II.I.A.3). While all electrode slurries shear thin, the shear flow index shows the effect of molecular weight of binder and the presence of dispersant on the degree of shear thinning. The shear flow indices of electrodes made with BM CsPAA with and without dispersant or with PCM CsPAA with and without dispersant are 0.324, 0.343, 0.355, and 0.372, respectively (Table II.I.A.3). The BM CsPAA slurries with and without dispersant are more shear thinning than their PCM counterparts by approximately 14%. Again, this is likely because higher molecular weights cause a more pronounced shear thinning effect, but changes in polymer conformation could also contribute to these effects. The shear thinning behavior is mitigated when dispersant is present in the slurry because the dispersant likely helps reduce the agglomerates of CsPAA, as indicated in the X-ray tomography data, which promotes lateral homogeneity within the electrode.

From the depth profile, it seems that the dispersant is interacting with the CsPAA binder molecules and disentangling them. This is somewhat counterintuitive in that dispersants are expected to improve the overall homogeneity of the slurry. However, CsPAA may be more strongly interacting with silicon surface as both are hydrophilic whereas carbon black is hydrophobic. Therefore, the dispersant may be causing silicon to be broken into smaller aggregates, while carbon black remains as large agglomerates. This particle size discrepancy may result in a slurry that is less homogeneous than it would be without dispersant counterpart. Essentially, the slurries without dispersant have large agglomerates, but the overall agglomerate size is more similar than that of the dispersant slurries.

From these processing and tomography studies, electrodes fabricated with binder solutions that were mixed by BM or PCM showed that the molecular weight distribution of the polymeric binder chains differed and led to unique architectures. Rheology and viscometry results revealed that different mixing methods caused a drastic decrease in molecular weight of the binder. BM blended binder has a higher average molecular weight (59,208 g/mol) and produced a laterally more uniform electrode in the presence of dispersant. PCM mixed binder suffered from the largest decrease in molecular weight (56,638 g/mol) and resulted in a more heterogeneous electrode laterally in the presence of dispersant. Regardless of the binder mixing method or the presence of dispersant, the binder segregated to the middle of the electrode, which suggests that PAA is not performing as a typical binder is not holding silicon and the carbon black in intimate contact with one another.

Table II.I.A.3: Molecular weight, initial viscosity, shear flow index, initial gravimetric capacity, and number of cycles for each electrode made with PCM blended binder with and without dispersant and BM blended binder with and without dispersant.

Binder, dispersant	Ostwald Molecular Weight of Binder (g/mol)	Initial Viscosity (Pa*s)	Shear Flow Index	Initial Capacity (mAh/g)	Number of Cycles
Starting PAA	450,000	—	—	—	—
PCM without dispersant	56,638	24.19	0.372	1142	1
BM without dispersant	59,208	33.01	0.343	1584	1
PCM with dispersant	—	19.27	0.355	1412	20
BM with dispersant	—	26.58	0.324	1630	20

Section Conclusions: These components, namely baseline PAA substitutional variants, alternative conductive additives, and low-oxide coated silicon materials, in combination with Zintl- electrolyte additives discussed later in the testing section, were evaluated. While data indicates that the exact conductive additive was not an important performance variable, low oxide content silicon had more stable electrochemical performance (i.e. gradual SiO₂ dissolution may disrupt the binder-solid interfaces), increasing PAA density at the electrode surface, and maximizing the bonding of the binder to the silicon surface (note dissolution issues) were critical to extending calendar life. Additionally, slurry and electrode formation studies using conventional PAA-based systems found that the binder preferentially segregates to the center of the electrode, which may be an important observation as delamination has been found to be an issue with several cell build runs where cell pressure is not controlled. Combined with BatPaC modeling efforts led by NREL, the best combination of materials available to the program, including a low oxide (hydride –terminated) silicon, a surface Ca-ion Zintl electrolyte additive, Gen2F electrolytes, and a densified PAA produced a very high CE cell that meets the Q4 milestone. Alternatives to the low oxide silicon samples are being considered once scale up issues are resolved. Notably samples with bonded surface coatings or reactive species have shown promise but have not made it to the point where a specific material has been identified as superior and scaled to the needed amounts using the stage-gate process. While several observations of stability and performance issues have been noted, alternatives to PAA (or LiPAA), mainly rely on water-based processing that can introduce water into the electrolyte leading to gassing, surface passivation issues, and salt hydrolysis. For the SCP program, baseline binder choices will be made by agreement between the Cell Build and the Science of Manufacturing teams.

2. Results: Silicon Electrode: Testing Protocols

Calendar Aging Screening Protocol: This protocol document provides a framework for the development of silicon (Si) electrodes for high capacity lithium ion batteries by providing standardized test protocols that researchers and early stage developers can use to assess the progress of silicon modifications, cell designs, electrolytes, or additives. Overall while full cell cycling for silicon anodes has progressed significantly over the past several years, similar progress in the area of calendar life remains a major challenge. The procedures detailed below have been developed out of a major scientific effort, funded by the Vehicles Technology Office, to understand the formation and evolution of the silicon solid electrolyte interphase (SEI). This first generation of procedures is designed to enable a reasonably well-equipped research laboratory to assess early research progress towards improving calendar aging issues in silicon cells in a reasonable timeframe. These generation-one procedures will be updated, modified and expanded as the research team obtains feedback from stakeholders and as our understanding of the SEI evolves.

Traditional approaches to investigate calendar aging often involve experiments that take as long as the period they investigate, the aging inflicted by months of storage is evaluated by exposing the charged cell to controlled conditions for that same number of months. More specifically, such tests age the cells under open-circuit conditions (no current or load applied), with periodic reference performance tests (RPTs) that measure the cell degradation as a function of aging time. The RPTs directly measure the metrics of interest, such as reversible capacity and energy/power retention. While providing extremely useful information, such approaches are clearly time-consuming and are likely to slow down the development of Si-based cells [44]

The testing protocol described in this document is designed to provide semi-quantitative insights on the quality of the SEI in approximately ~2 weeks. Rather than tracking cell capacity losses over very long times, the protocol presented relies on measuring, in real time, the currents associated with reactions that form or decompose the SEI as the anode is held at a constant state-of-charge (SOC). The evolution of these currents over time provides a basis to understand how the state of passivation of the anode evolves over longer time scales. We note that calendar aging is a complex process that involves not only loss of Li^+ inventory, but also active material loss, electrolyte degradation and power fade. While the testing protocol being developed by our team will *not* predict all these aspects of calendar aging, it will nonetheless provide information about the rates of Li^+ inventory losses to the SEI, which is a main factor limiting the calendar life of silicon-based anodes.

The testing protocol described herein departs from traditional calendar aging tests in that *it does not provide absolute calendar lifetime predictions*. Instead, the results should be compared against those of standard electrodes like graphite with calendar lifetimes well characterized by other methods. Future versions of this protocol may provide the ability to quantitatively predict calendar lifetime as the analysis methods are further developed and the lifetime predictions are validated by independent tests. Until such capabilities are available, this protocol can be used to quickly and easily screen electrolyte compositions and silicon electrodes. After this initial investigation, the most promising systems can be studied under more resource intensive experiments, such as traditional calendar life tests that use long rests with intermittent RPTs.

Protocols: The procedure to test the calendar life of Si anode materials is extremely sensitive to the test cell setup, especially the geometric size and areal capacities of both the test electrode and the counter electrode. Therefore, for reliable comparisons between tests, the testing procedures should adhere to the following requirements:

Cell Design: Size 2032 stainless steel coin cells are used as the electrochemical test vehicle. The electrodes consist of the Si anode material (the test electrode) against a thick high-capacity lithium iron phosphate (LFP) cathode. When an LFP electrode of sufficiently high areal capacity is not available a Li counter electrode can be used instead, we warn that the chemical reactivity of lithium can alter the electrolyte composition and can affect

the generality of observations obtained for some systems. The diameters are 14 mm for the cathode (LFP) when it is paired with the 15 mm diameter Si-containing test anode. When the Si-containing electrode is paired with a Li counter electrode then the Si electrode is 14 mm diameter with a 15 mm diameter Li foil (less than 1 mm thick).

The areal capacities of the electrodes are chosen to ensure that there is enough Li^+ inventory to supply the Si-containing test electrode with capacity during the aging protocol. The LFP electrode is greater than or equal to 2.5 mAh/cm^2 , while the Si-containing test electrode is less than or equal to 1.3 mAh/cm^2 at the state-of-charge (SOC) at which aging will be assessed. This additional Li^+ inventory is meant to guarantee that the cathode would still retain excess capacity even after the large irreversibility that is typical of Si electrodes in the first few cycles. If electrodes with loadings other than those designated are used, it is imperative that the total utilized capacity of the Si electrode (reversible capacity + accumulated irreversible capacity) not exceed the capacity of the counter electrode during the test. This design ensures that the counter electrode can effectively supply the Li^+ needed to (re)form the SEI at the Si test electrode.

Table II.I.A.4: Requirements of test and counter electrodes

Electrodes	Chemistry	Capacity	Diameter
Test Anode:	Si material	$<1.3 \text{ mAh/cm}^2$	15 mm diameter (14 mm vs. Li)
Preferable cathode:	Lithium iron phosphate (LFP)	$>2.5 \text{ mAh/cm}^2$	14 mm diameter
Acceptable counter electrode:	Lithium metal	$>2.5 \text{ mAh/cm}^2$	15 mm diameter

Cell assembly: The 2032 stainless steel coin cell is built following an assembly process, summarized in Table II.I.A.4, that has been well established at Argonne National Laboratory [45] and is summarized below:

1. Electrodes should be dried under dynamic vacuum for at least 14 h at $120 \text{ }^\circ\text{C}$ for PVDF binder (LFP cathode) containing electrodes, and $150 \text{ }^\circ\text{C}$ for PAA or LiPAA binder containing electrodes. Other binders that are used should be dried appropriately so as not to affect the cell chemistry.
2.
 - a. Note that thick single sided LFP electrodes can curl when wet with the electrolyte. Thus, we recommend assembling LFP containing cells from the anode side up in the following order: cell cap with attached polypropylene gasket, 0.5 mm thick stainless steel spacer, 15 mm Si test electrode, $20 \text{ } \mu\text{L}$ electrolyte, 19 mm diameter layer of 2325 Celgard separator or equivalent, $20 \text{ } \mu\text{L}$ electrolyte, 14 mm LFP counter electrode, 0.5 mm thick stainless steel spacer, stainless steel wave spring, cell case.
 - b. Li half-cells should be assembled in the following order: cell case, 14 mm Si test electrode, $20 \text{ } \mu\text{L}$ electrolyte, 19 mm diameter separator layer, polypropylene gasket (oriented to properly mate with cell cap), $20 \text{ } \mu\text{L}$ electrolyte, 15 mm diameter Li metal foil ($< 1 \text{ mm}$ thick), 0.5 mm thick stainless steel spacer, stainless steel wave spring, cell cap.

3. The assembled cell stack should then be crimped together with a hydraulic crimper, preferably an automatic crimper for consistency.

C-rate determination: The C-rate is defined as the current necessary to drive the Si test electrode from one voltage cut-off to the other in 1 hour (a C/10 rates takes 10 hours to drive the electrode from one voltage cutoff to the other). This value is determined using half-cell data of the second cycle of the Si test electrode. Because the LFP electrode delithiates at ~ 3.45 V vs. Li/Li⁺, and relithiates at ~ 3.40 V vs. Li/Li⁺, the cutoff potentials correlate as follows:

- 2.7 V vs. LFP (discharge) = 0.7 V vs. Li/Li⁺
- 3.35 V vs. LFP (charge) = 0.1 V vs. Li/Li⁺

LFP-based full cell:

1. Rest cell at OCV for 4 hours to allow electrolyte wetting
2. At a C/10 rate, charge to 3.35 V, discharge to 2.7 V, repeat 3 times, data acquisition should be $\Delta V = 5$ mV
3. Hold cell at 2.7 V until $i < C/100$ to fully lithiate test electrode, data acquisition should be $\Delta t = 1$ min, $\Delta i = 10$ μ A at a C/10 rate, data acquisition should be $\Delta V = 5$ mV
4. Hold potential at 3.35 V for 180 hours, data acquisition should be $\Delta t = 1$ min, $\Delta i = 10$ μ A
5. Discharge to 2.7 V at a C/10 rate, data acquisition should be $\Delta V = 5$ mV
6. Hold cell at 2.7 V until $i < C/100$ to fully lithiate test electrode, data acquisition should be $\Delta t = 1$ min, $\Delta i = 10$ μ A
7. At a C/10 rate, charge to 3.35 V, discharge to 2.7 V, repeat 2 times, data acquisition should be $\Delta V = 5$ mV

Lithium Half-cell (same procedure as LFP full cell with potential cutoffs substituted as follows):

- 0.1 V instead of 3.35 V
- 0.7 V instead of 2.7 V

The preliminary efforts described in this report are limited to studying SEI passivation at the SOC achieved by the anode at ~ 0.1 V vs. Li/Li⁺, for a graphite electrode, this would correspond to $\sim 55\%$ of lithiation. Most Si-based electrodes can remain mechanically stable when cycled to this potential, and thus permanent losses of active material are less likely to occur during the tests discussed here. Our team recognizes that SOC is an important variable when investigating calendar aging and modeling SEI growth [46] and future studies will expand the scope of this report.

Data Collection: Verifying the current response of the cell during the voltage hold is critical to guarantee that the data analysis will be meaningful. **Figure II.I.A.28** shows the current that is measured during the hold, normalized to the capacity (lithiation capacity measured during the charge immediately before the voltage hold) of a test silicon electrode and a graphite baseline electrode. The expected behavior for the current measured in both systems are shown in **Figure II.I.A.28**, where the continuous decay exhibited by the traces indicates that the counter electrode is supplying sufficient Li⁺ inventory. This plot also qualitatively demonstrates that the currents that arise from parasitic reactions on the graphite electrode, seen long after the initial decay, are roughly an order of magnitude smaller than those observed for the silicon, demonstrating its better passivating behavior

and longer calendar lifetimes, as expected. The results displayed in this type of plot should serve as a gate to determine if further analysis should be performed using the testing protocols described in this document. *If the residual current (i) does not approach that of a baseline electrode such as graphite (necessarily within an order of magnitude), then further analysis is not warranted, as the SEI is clearly not sufficiently stable.* It is recommended that the data acquisition parameters discussed in the previous section are used in the voltage hold test, to ensure enough resolution.

A major pitfall of this experimental protocol occurs when the Li^+ inventory of a test cell is exhausted (counter electrode is completely delithiated). The sudden decline of the current responses to diminishingly small and indistinguishable values as seen in **Figure II.I.A.28** (after ~ 40 h of voltage hold) indicates that the Li^+ inventory supplied by the counter electrodes has been exhausted during the V-hold. Under these conditions, the external current no longer provides a direct measure of the rate of parasitic reactions, yielding inaccurate information about the electrode's calendar lifetime. This is another critical reason why the current response of the collected data needs to be evaluated before performing the analysis described in the next section. If the current response displays a similar behavior to that shown in **Figure II.I.A.28**, the test cell should be remade with a higher capacity counter electrode or a lower capacity test electrode.

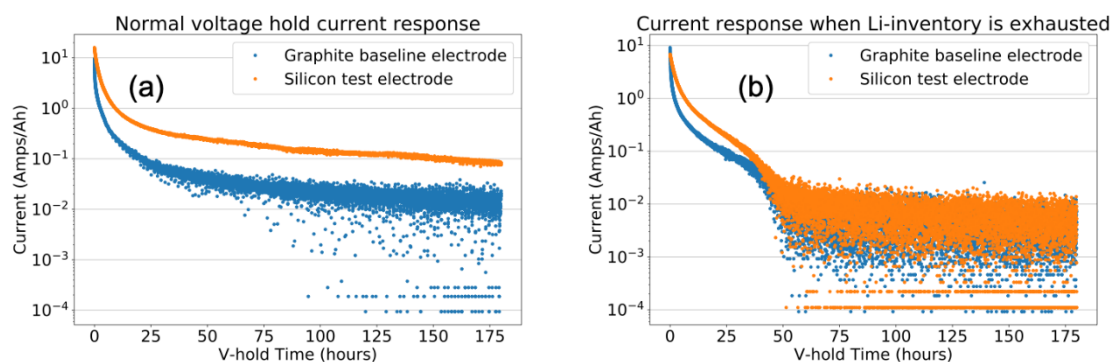


Figure II.I.A.28 Current decay versus time during voltage holds of (blue) graphite baseline anode and (orange) 80 wt% Si test anode. The current has been normalized to the capacity of the test electrode measured during the lithiation immediately before the voltage hold. Panel (a) shows the current response where there is an excess of Li^+ inventory supplied by a counter electrode with a flat voltage profile, as is the scenario marked (a) in Figure 3. Panel (b) shows how the current suddenly declines as the Li^+ inventory supplied by the counter electrode is exhausted, polarizing the electrodes to high potentials. Under these conditions, the measured current underestimates the actual rate of parasitic reactions experienced by the test electrode.

Data Analysis: Analysis of the data should first be done by qualitative visual inspection and comparison between the test electrodes and a baseline electrode. Figure II.I.A.29 shows the current decays of three different Si test electrodes and a graphite baseline electrode. The normalization of the current data to the reversible capacity of each electrode is important because the resulting units of Amps/Ah indicate the rate at which each electrode is losing reversible capacity due to Li^+ consumption at the SEI. If the normalized current measured from a Si test electrode at the end of the 180-hour voltage hold is distinguishably higher than the baseline electrode, further analysis is not needed, as the electrode's SEI is clearly not sufficiently stable. This is the case for each of the Si test electrodes shown in Figure II.I.A.29, thus showing the effectiveness of this simple qualitative comparison for the initial screening of Si test electrodes.

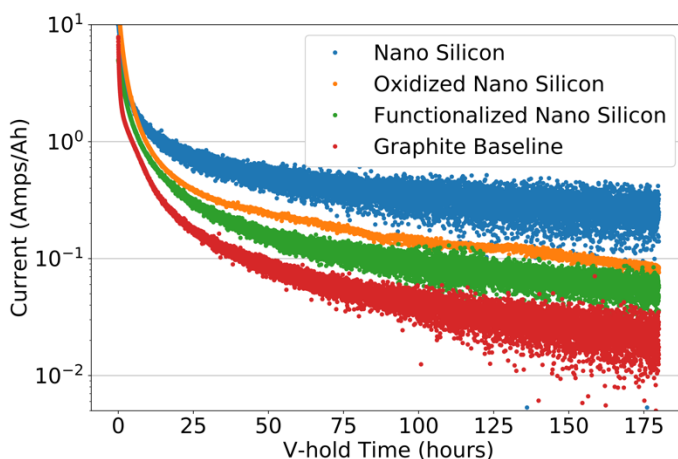


Figure II.I.A.29. Current decay versus time during voltage holds of several different Si test electrodes and a graphite baseline electrode. The rate of parasitic reactions of the Si test electrodes can be qualitatively distinguished by visual inspection, and all exhibit greater aging rates than the graphite baseline electrode.

The average current after 180 hours of voltage hold can be used as a metric to rank the rate of parasitic reactions at each electrode and is reported below for the examples shown in **Figure II.I.A.29**. This information should be complemented by details about electrode composition, areal capacity, and electrolyte used in the tests. Additionally, because there can be variability between tests for a given electrode and electrolyte pair, we recommend that a sample size of at least three test cells for each test electrode type be reported.

Example reporting:

Graphite baseline electrode

1.17 mAh/cm²

91.83 wt% Superior Graphite SLC1520P

2 wt% Timcal C45 carbon

6 wt% Kureha 9300 PVDF Binder

0.17 wt% Oxalic Acid

Electrolyte: 1.2 M LiPF₆ in ethylene-carbonate:ethyl-methyl-carbonate 3:7 + 10 wt% FEC

Mean terminal current = 0.023 mA/Ah

Nano Silicon

0.3 mAh/cm²

20 wt% 3.9 nm diameter Si nanoparticles

65 wt% Timcal C65 carbon

15 wt% PAA Binder

Electrolyte: 1.2 M LiPF₆ in ethylene-carbonate:ethyl-methyl-carbonate 3:7 + 10 wt% FEC

Mean terminal current = 0.262 mA/Ah

Oxidized Nano Silicon1.24 mAh/cm²

80 wt% Surface oxidized 150 nm diameter Si nanoparticles

10 wt% Timcal C45 carbon

10 wt% LiPAA Binder

Electrolyte: 1.2 M LiPF₆ in ethylene-carbonate:ethyl-methyl-carbonate 3:7 + 10 wt% FEC**Mean terminal current = 0.092 mA/Ah****Functionalized Nano Silicon**0.7 mAh/cm²

40 wt% 4-phenylphenol surface functionalized 30 nm diameter Si nanoparticles

40 wt% Timcal C65 carbon

20wt% PAA Binder

Electrolyte: 1.2 M LiPF₆ in ethylene-carbonate:ethyl-methyl-carbonate 3:7 + 10 wt% FEC**Mean terminal current = 0.059 mA/Ah**

These examples highlight the capabilities of the screening protocol described in the current version of this document. Because it is currently limited to qualitative analysis, it is especially important to use a baseline electrode with a calendar life well characterized by other methods under the conditions of interest. Future versions of this report may include a semi-quantitative model to describe the rate of parasitic reactions in the electrodes of interest, which is currently under validation by long-term experiments, this model is outlined in general terms at the end of the discussion section.

Our methodology is based on using *voltage holds* to measure the rate of Li⁺ trapping at the SEI in Si-containing cells. *This approach has the advantage of recording real-time rates of side reactions, providing information about the time-dependence of such processes and potentially enabling extrapolation of behaviors observed in short duration experiments.* Its working principle is since parasitic *reduction* reactions (such as the ones involved in SEI formation) effectively consume electrons from the anode, which decreases the anode SOC. The instantaneous voltage of a cell is the difference between the potentials of the positive and negative electrodes, so a change in the anode SOC yields a change in cell voltage. If the anode SOC is “pinned” by holding the cell voltage constant, electrons must flow from the cathode to the anode to replenish the charge consumed by side reactions, in order to keep the anode SOC invariant, i.e., the *current* flowing through the cell and measured by an external circuit is equal to the rate of these parasitic processes. This ideal equivalence between the parasitic and measured currents is achieved when the anode has a sloped potential and is most sensitive to SOC and the cathode is insensitive to SOC (the voltage profile is “flat”). We can approximate these conditions by using LiFePO₄ (LFP) as a cathode (which can provide most of its capacity while at ~3.45 V vs. Li/Li⁺), and by performing the voltage hold at potentials in which the anode cycling profiles are notably sloped to maximize sensitivity.

For these tests, it is important that the LFP counter-electrode have a capacity in excess of what is used by the reversible and irreversible reactions occurring at the Si test electrode. The importance of this condition is demonstrated by the simulated voltage profiles shown in **Figure II.I.A.30**, where the LFP voltage profiles are shown in blue. Profiles for pristine (solid line) and aged (dashed line) Si anodes are displayed in black with the corresponding full cell voltage profiles displayed in red. The intersecting lines marked **(a)** in **Figure II.I.A.30** represent the pristine full cell being held at 3.35 V, where the potential at the pristine Si anode would be roughly

equivalent to ~ 100 mV vs. Li/Li^+ . In this pristine cell at 3.35 V, the LFP voltage profile is insensitive to SOC (voltage profile is flat), and thus any changes of the Si SOC would require a change in cell voltage i.e., the Si SOC is “pinned”. As electrons and Li -ions are consumed at the Si electrode during aging, they are replenished by the LFP cathode, as additional Li^+ extraction is possible at that same electrode potential. Nevertheless, if enough capacity is lost, the aged cell may no longer be able to keep the Si SOC constant. This Li^+ inventory exhaustion scenario is represented by the intersecting lines marked **(b)** in **Figure II.I.A.30**, where the aged cell is still held at 3.35 V. In the aged cell with an exhausted Li^+ inventory, the LFP voltage profile is polarized above its plateau potential and is sensitive to SOC (highly sloped), resulting in the Si electrode no longer being held at the desired potential of 100 mV vs. Li/Li^+ . When that happens, additional Li^+ extraction from LFP to counter parasitic reactions at the anode would cause an increase in the potential of both electrodes, this would involve a net decrease in anode SOC, and thus the currents measured by an external circuit would underestimate the extent of side-reactions in the cell.

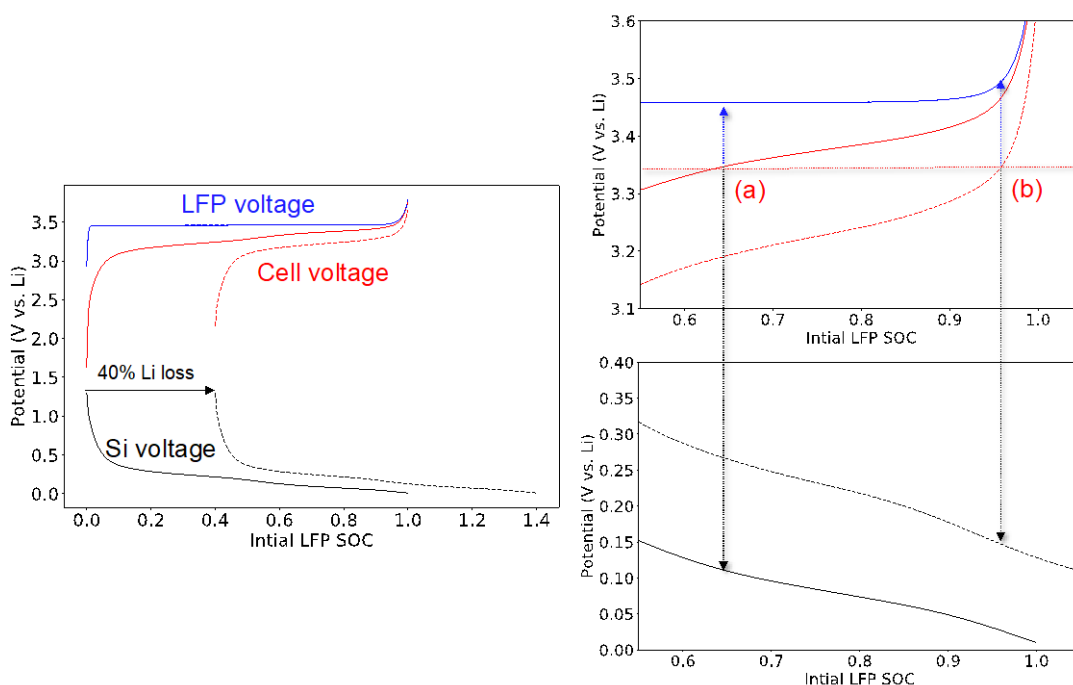


Figure II.I.A.30. (left) Simulated voltage profiles for an LFP cathode (blue), Si anode (black), and the 2-electrode cell combining those two electrodes (red). The dashed black line represents Si electrode aging by the loss of Li^+ inventory, which effectively shifts the Si voltage profile relative to the LFP voltage profile, and results in the aged cell having the dashed red voltage profile. **(right)** Zoomed in portions of the voltage profiles where the dotted horizontal red line represents a voltage hold potential of 3.35 V for pristine (a) and aged (b) Si electrode containing cells.

The use of LFP as a counter-electrode has additional advantages. One is that the cathode can be assumed to be an essentially inert electrode, since its low potentials will lead to little changes in electrolyte composition and are unlikely to generate oxidative currents that could affect the analysis. Additionally, the extremely flat voltage plateau of LFP over its entire capacity range allows it to be used as a reliable pseudo-reference electrode in a two-electrode coin cell. Thus, the absolute potential of the anode can be well controlled, facilitating studies on the effect of SOC on passivation. The test protocol specifics and an example voltage profile are shown in **Figure II.I.A.31**, where a 180-hour long voltage hold is preceded by three formation cycles and followed by two additional diagnostic cycles. The total test time is ~ 290 hours (less than two weeks).

Calendar-life Protocol

1. 4 hour OCV rest
2. 3 cycles @ C/10 (2.7 V to V_{high})
3. Charge to V_{high} , 180 hrs hold @ V_{high} , discharge to 2.7 V
4. Optional: 2x cycles @ C/10 (2.7 V to V_{high})

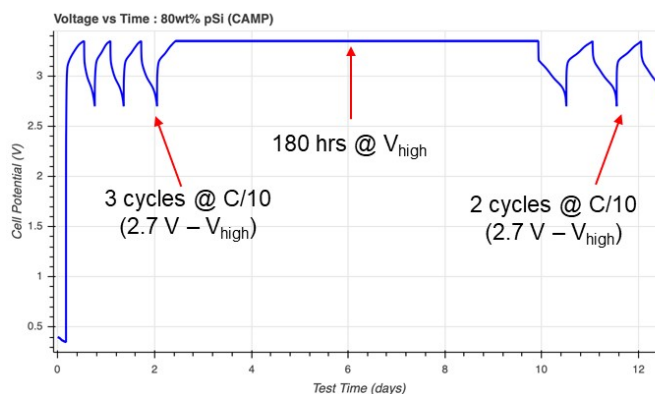


Figure II.I.A.31. The test protocol to estimate the rate of parasitic reactions of Si-based electrodes. The example voltage profile is from a cell coupling a 80% Si electrode vs. an LFP cathode.

Although this experimental approach is a logical pathway to derive information about electrode passivation from short term tests, it also presents challenges. In practice, electrodes present a finite impedance and lithiation processes are incomplete by the time the voltage hold initiates. Hence, the current measured during the early periods of voltage hold is a combination of reversible lithiation processes (lithiation of Si) and irreversible electrochemical reactions (SEI formation and concomitant Li^+ consumption). As the voltage is held for longer and longer times, the proportion of the current driving reversible reactions diminishes relative to the current driving the irreversible reactions, and the measured current becomes a more reliable descriptor of parasitic processes. For these component contributors, *the challenge exists to validate that the analyses can differentiate between both these contributions to the measured current.* The reversible capacity that is passed during the voltage hold can be experimentally quantified by inspecting cell discharge after the hold, and these values are used to help differentiate the time dependent contributions from the reversible and irreversible processes.

The purpose of the 180-hour long voltage hold is to determine the rate of Li^+ inventory consumption, as measured by the current, due to irreversible side reactions at the anode surface. Using this method, the current measured during the voltage hold is due to a combination of the reversible lithiation reactions and the irreversible side reactions. **Figure II.I.A.28** shows the typical current responses during the voltage hold of example electrodes. The current densities decrease more than an order of magnitude during the first ~20 hours of the voltage hold as the reversible lithiation reactions near completion. In contrast, towards the end of the voltage hold, the current densities stabilize at diminishingly small values that are primarily due to irreversible Li^+ consuming reactions. The lower current density of the graphite electrode at the end of the voltage hold compared to the Si electrode is good confirmation that the measurement is qualitatively capturing the expectedly better SEI stability (and lower Li^+ inventory consumption rate) of the graphite electrode. **Figure II.I.A.28** shows the current response during the V-hold where the Li^+ inventory of the cell becomes exhausted. This occurs when the cathode is unable to supply additional electrons and Li-ions to keep the anode pinned at a fixed SOC, as outlined by marker **(b)** in **Figure II.I.A.30**. In this case, the full cell is maintained at a fixed voltage with a net decrease in anode SOC,

resulting in the measured currents underestimating the parasitic reaction rates. This can be seen in **Figure II.I.A.28** by the sudden decrease in current to vanishingly small values and highlights the importance of performing these experiments in cells with excess counter electrode capacity.

Integrating the measured current over time during the voltage hold and normalizing to the electrode's reversible capacity yields time dependent capacity, $Q_{\text{hold}}(t)$. In order to deconvolute the irreversible and reversible contributions to the capacity, the following function can be fit to the normalized capacity data:

$$Q_{\text{hold}}(t) = Q_{\text{irrev}}(t) + Q_{\text{rev}}(t)$$

The numerical forms of these functions are still being determined using long term voltage hold validation experiments. As the validation data becomes available, future versions of this report may include numerical models that can be used to semi-quantitatively describe the rate of SEI-related side-reactions. Preliminary results suggest that $Q_{\text{rev}}(t)$ has an asymptotic time dependency as the reversible capacity approaches a maximum value at long times, whereas $Q_{\text{irrev}}(t)$ may be proportional to the square-root of time. The square-root of time dependency of $Q_{\text{irrev}}(t)$ is well supported by empirical observations in the literature, and is believed to capture the general behavior of SEI growth. [46,47] This particular functional form arises from the hypothesis that the irreversible side reactions occurring at the electrode surface due to SEI formation are diffusion limited, and thus their rates are inversely proportional to the square root of time.

Notwithstanding, the Si SEI stability will naturally fluctuate as a function of numerous internal and external factors. The present report is just the beginning of an exploration of the Si calendar life behavior embedded in a current response, the measurement probe of choice. In an electrochemical process, electrode kinetics and their reaction rates are tied to a current value. The parasitic reactions in Si electrodes are exceedingly complex and, as a first pass, it is affiliated with (1) the Li ion conductivity in the SEI, (2) the mechanical stability of SEI, (3) chemical stability (solubility) of the SEI, and (4) the electronic conductivity within the SEI. What factors dominate thus begs the question: how can one slow down this degradation phenomena and create 'immunity'?

Section Conclusions: A method to qualitatively compare the calendar aging rates of silicon anodes has been developed using full cells with an excess amount of electrolyte and of Li^+ supplied by an LFP counter electrode. After formation cycles, the voltage of a test cell is held for 180 h, and the current response measured during the voltage hold can be used to qualitatively compare the rates of Li^+ consumption at the SEI of silicon test electrodes to a baseline electrode. Long term voltage hold aging experiments are underway to determine numerical models that can be used to derive aging parameters for silicon test electrodes. Once the numerical models developed by our team are fully validated, they can be used to support developments of cell, material, and interfacial designs that minimize calendar aging rates of Si electrodes. This protocol study, produced by a joint effort between the SEISTA and DeepDive teams, is a work in progress and will be updated on the SCP program as new updates are available and agreed upon by the SCP team.

3. Results: Silicon Electrodes: Additives

Stability issues associated with silicon anodes have hampered the widespread their use in commercial lithium-ion batteries. A critical aspect, especially as it relates to calendar life issues, is their reactivity when charged (lithiated) due to formation of highly reactive lithium silicide binary Zintl phases, i.e. Li_7Si_3 . This reactivity against cell components and the electrolyte causes major inefficiencies and loss of lithium and electrons, which severely reduces cycle life and long-term performance of the silicon electrode. Our FY19 efforts showed that,

the addition of small amounts of soluble alkaline earth salts (Mg,Ca etc.) to the programmatic baseline Gen2 electrolyte + FEC led to a significant improvement in cycle and calendar life for silicon-containing anode materials for LIBs, a focus of the DeepDive program in association with the SEISTA Si effort. This stabilization is achieved by replacing the reactive and redox active lithium silicide with more stable surface Li-Mg-Si ternary Zintl phases. As shown by Han, et al., the incorporation of Mg was not done by heating or an external process but by inclusion from the electrolyte in an in-situ electrochemical fashion via an ion-exchange reaction at low cell voltage. Spectroscopically, data collected indicated that the Mg^{2+} from solution was incorporated into the surface of the silicon electrode, replacing $2 Li^+$ with Mg^{+2} . Of the metal salts tested in 2032-coin cells, the added electrolyte salts with either magnesium (Mg^{2+}) or calcium (Ca^{2+}) cations proved to work the best over hundreds of charge — discharge cycles. For instance, in cells with pure silicon anodes coupled with lithium-rich cathodes, the energy densities surpassed those for comparable cells having graphite chemistry by up to 50%, as long as a compatible silicon source is used to allow for multivalent ions to diffuse through the anode.

In a continuation of this effort, the DeepDive expanded the multivalent electrolyte additive study to pouch cells fabricated by ANL CAMP facility and evaluate various cell configurations with different electrolyte systems. Stabilization and optimization of silicon electrode studies have focused on electrode composition optimization and calendar life studies.

Silicon Pouch Cells with Multivalent Electrolyte Additives: The CAMP Facility completed the first round of testing the magnesium and calcium electrolyte additives in single-layer pouch cells that were fabricated in the fourth quarter of FY2019. The high silicon content electrodes used in this project were from the CAMP Facility's Electrode Library and used a LiPAA binder paired with NMC532 or HE5050 cathodes – these cell configurations cycling protocols are described in Table II.I.A.5.

Two NMC532 cathodes were selected with different capacity loadings to test the effect of n:p ratio. Magnesium and calcium containing electrolytes were provided to the CAMP Facility before the pouch cells were assembled. These electrolytes (including the baseline electrolyte) are described as follows:

- Gen2F= Gen2 + 10% FEC (baseline electrolyte)
- GenFM = Gen2F+ 0.1M $Mg(TFSI)_2$
- Gen2FC = Gen2F+ 0.1M $Ca(TFSI)_2$

Under evaluation, the additive cells showed superior cyclability and higher coulombic efficiencies in both half-cell and full cell configurations than the cell tests using Gen2F electrolytes (Figure II.I.A.32). The pouch cells with the higher capacity NMC532 cathodes (A-C013B) lost capacity at a faster than expected rate, regardless of the electrolyte. The pouch cells with the lower capacity cathodes (HE5050 (A-C017) and NMC532 (A-C015B)) had better capacity retention and that was found to be independent of the additive electrolyte used, with the exception that the baseline electrolyte test (“GenF”) pouch cells teamed with a lower capacity NMC532 electrodes (A-C015B). These results were not in total agreement with the earlier coin cell studies where the Ca^{+2} and Mg^{+2} additives had a clear advantage, in these pouch cells the Ca^{+2} stood out as the better performer and are still under evaluation (~70% retention after 300 cycles). Cells from these evaluations are being evaluated at the Post-Test Facility. As with last year’s larger scale studies, the pouch cells that used the higher capacity NMC532 cathode (A-C013B) showed excessive signs of delamination in the pouch cells with NMC532 at the higher capacity (A-C013B cathode).

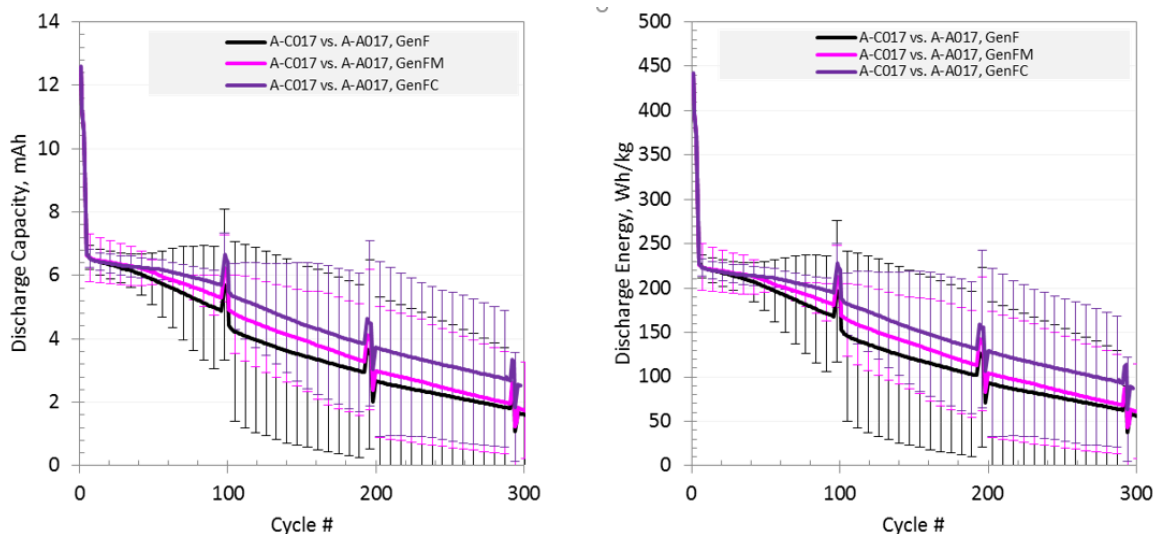


Figure II.I.A.32 Cycle life discharge capacity and energy comparison for baseline and multivalent electrolytes

The cathode cell sets with lower capacity cathodes: HE5050 (A-C017) and NMC532 (A-C015B) were also checked for signs of anode delamination. It was observed that the NMC532 low-loading cathode cells (at 4 psi) only showed anode delamination for the Gen2F electrolyte case (see Figure II.I.A.33). In FY19 this was also observed and coincided with the cell pressure applied. Work by CAMP has found that the higher constant (spring) pressure in coin cells had more stable cycling performance than the pouch cells. Adding pressure to the testing protocol (up to 76 PSI) enhanced the performance, initial analysis by CAMP researchers indicated that shrinking the lower cutoff in the testing may be beneficial after formation cycling to magnesiate the surface in order to minimize the crystallization of $Li_{13}Si_4$, the point silicon in the electrode goes from an amorphous state to a crystalline one.

Optimization of Electrode Composition: The program has been using two kinds of Si anode compositions, 80% silicon or 10%-20% silicon with graphite. The electrodes with 80% silicon show inferior stability while the Si/graphite electrodes had low specific capacity in which the performance gradually became graphite only. Therefore, we focused on optimization of silicon anode composition. This ANL effort then focused on the optimum composition for baseline systems but also helps to improve performance by understanding the working

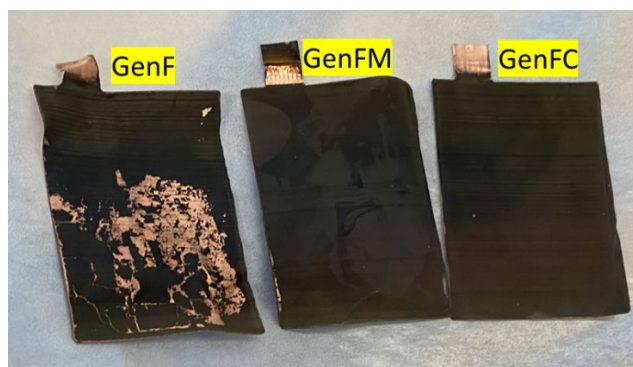


Figure II.I.A.33. Harvested anode electrodes from single-layer pouch cells (at 4 psi) with baseline “Gen2F” electrolyte (left), “Gen2FM” electrolyte (center), and “Gen2FC” electrolyte (right) using the lower capacity NMC532 cathode (A-C015B). Unexpected delamination seen only on anode with Gen2F electrolyte.

Table II.I.A.5 Cell configurations and Cycling Protocols

			Protocol
CAMP C015 NMC532 Electrode	CAMP A017 Graphite-free Si Electrode (4kg-batch)	Gen2F Gen2FM Gen2FC Gen2FA	First at C/20 from 3.0 to 4.1 V for 3 formation cycles, then at C/3 from 3.0 to 4.1 V for 92 aging cycles, with voltage holding at the end of each charging stage.
CAMP C015 NMC532 Electrode	CAMP A016 Graphite-free Si Electrode (4kg-batch)	Gen2	
CAMP C015 NMC532 Electrode	CAMP A013 15%Si+73%Graphite	Gen2F Gen2FM	
CAMP C017 HE5050 Electrode	CAMP A017 Graphite-free Si Electrode (4kg-batch)	Gen2F Gen2FM Gen2FC Gen2FA	First at C/20 from 3.0 to 4.5 V for 3 formation cycles, then at C/3 from 3.0 to 4.1 V for 92 aging cycles, with voltage holding at the end of each charging stage.
CAMP C017 HE5050 Electrode	CAMP A016 Graphite-free Si Electrode (4kg-batch)	Gen2	

As shown in Figure II.I.A.34, six compositions with different silicon contents, conductive additive (C45), and binder (LiPAA) were studied. Each composition is denoted by three numbers representing the components. For instance, 811 indicates 80% Si, 10% C45, and 10% LiPAA. Since C45 is much lighter and more porous than Si powders, the higher content of C45 automatically reduces the areal loading of electrode materials. Therefore, the areal Si loading of 442/433 anodes is 71% lower than 811 anodes (Figure II.I.A.34). Such lower areal loading would decrease the deliverable capacity of the electrodes.

Figure II.I.A.34 shows the cyclic performance of typical cells with different Si anodes, showing specific capacity normalized by the weight of silicon. Most of the initial capacities are higher than the theoretical capacity of silicon, indicating that C45 also contributes to the capacity. More conductive additive and binder clearly enhanced the performance and stability of silicon, which is reflected by the highest specific capacity and capacity retention of the 442 electrodes while the lowest specific capacity and rapid capacity decay of the 811 electrodes. However, if the specific capacity is normalized by the weight of the electrode (Si+C45+LiPAA), 442 and 433 cells have the lowest specific capacity due to the low electrode areal loading and silicon content (Figure II.I.A.34). Except for the 811 cells, the coulombic efficiency of other cells exhibits a similar tendency without

notable differences (Figure II.I.A.34). Based on Figure II.I.A.34, the 712 cell and the 622 cells have the best balance between the silicon performance and electrode performance.

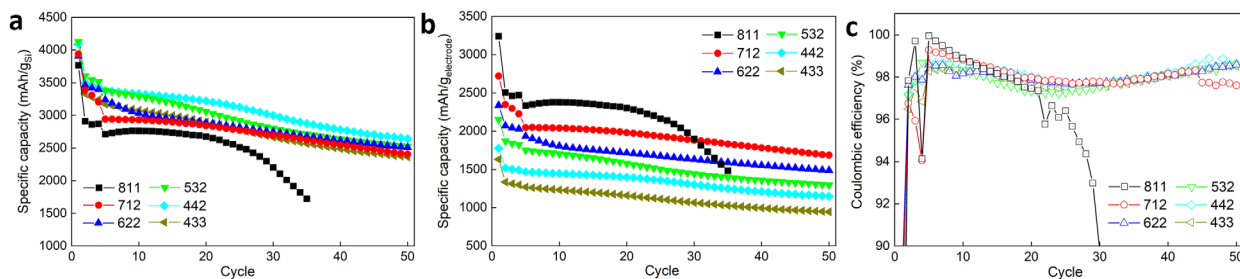


Figure II.I.A.34 Cyclic performances of typical cells with different Si anodes. (a) Specific capacity normalized by the weight of silicon. (b) Specific capacity normalized by the weight of electrode (Si+C45+LiPAA). (c) Coulombic efficiency of the cells.

Figure II.I.A.35 is the average lithiation specific capacity of three 622 cells and three 712 cells up to 60 cycles. The lithiation capacity of 622 cells surpassed that of 712 cells after 58 cycles. Moreover, from the error bars, 712 cells start losing their lithiation stability after 46 cycles. The cyclic performance of delithiation exhibited a similar tendency with an even earlier start point of 712 cells losing stability (Figure II.I.A.35). The coulombic efficiency plot indicates that 712 cells have a higher irreversible capacity loss after 40 cycles (Figure II.I.A.35). Further tests revealed that 622 cells can stably operate over 100 cycles without notable capacity fluctuation. Therefore, 622 Si anodes have a good combination of capacity and stability, which have the potential to be used in full cells.

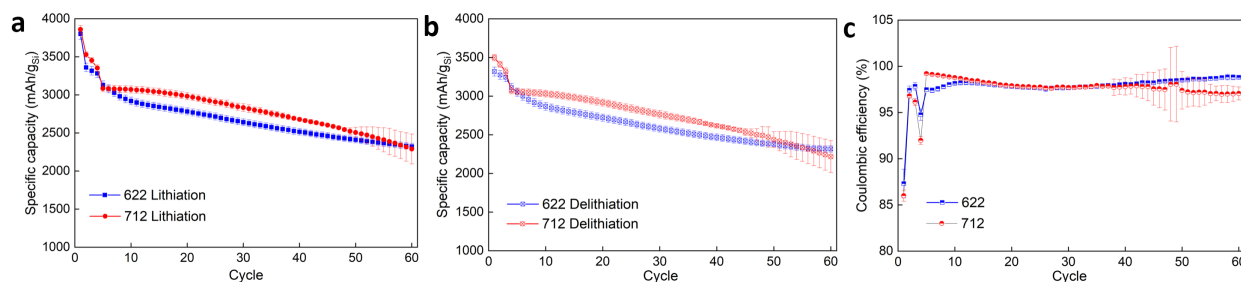


Figure II.I.A.35 Cyclic performance of 622 and 712 cells. (a) Lithiation specific capacity. (b) Delithiation specific capacity. (c) Coulombic efficiency.

Calendar Life Studies with Multivalent Electrolyte Additives: As previously discussed in detail, Li-M-Si (M=Mg, Ca, Al) Zintl phases form in-situ formed around Si particles can stabilize the electrode-electrolyte interface and improve cyclic lifespan as well as capacity retention. However, for Si anodes calendar life is also critical for practical applications. Here, a preliminary study was carried out on Si622/NMC532 cells. When assembling the cells, Mg(TSFI)₂ and Ca(TSFI)₂ were added into the baseline Gen2F electrolyte, forming Gen2FM and Gen2FC electrolytes, respectively. The cells were held at 4.1 V for 1 week (168 h) after three formation cycles at C/20 and three aging cycles at C/3. Figure II.I.A.36 is the current/time profile during constant voltage holding. The data points of the Gen2FC cell appear to be more concentrated. Accordingly, the capacity/time profiles show that the cell with the Gen2FC electrolyte had less capacity loss when holding (Figure II.I.A.36). Consistent with the current and capacity profiles, the specific capacity change of aging cycles before and after holding showed that the Gen2FC cell had the least capacity loss indicating that the Li-Ca-Si Zintl phase may also stabilize the interface while constant voltage holding, leading to better calendar life for the full cells (Figure II.I.A.36).

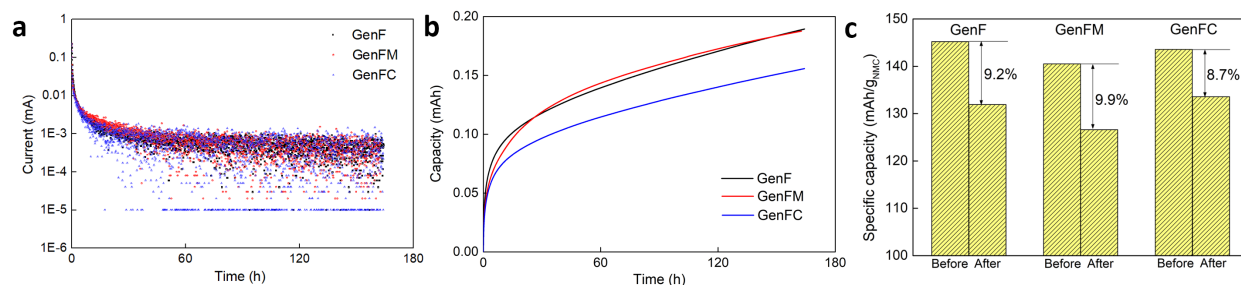


Figure II.I.A.36 Calendar life tests of Si622/NMC532 cells with GenF, Gen2FM, and Gen2FC electrolytes. (a) Current/time profile. (b) Capacity/time profile. (c) Comparison bar chart of aging cycle specific capacity before and after constant voltage holding.

Si622/LFP full cells were used to further identify the influences of Zintl phase on the calendar life due to the outstanding stability and small voltage variation of LFP when charging/discharging. For this study we used the Silicon Deep Dive Calendar Aging Electrochemical Screening Protocol. Specifically, the cells with GenF, Gen2FM, and Gen2FC electrolytes were held at 3.35 V for 1 month (720 h) after three formation cycles at C/10. The current/time clearly shows that the data points of the Gen2FC cell are highly concentrated comparing with the other two cells (Figure II.I.A.37), indicating the interphase enabled by the Li-Ca-Si ternary Zintl phase is more stable than the other two electrolytes. A similar conclusion can be concluded from the capacity/time profile (Figure II.I.A.37), which shows the cell with Gen2FC electrolyte had lower capacity loss after 720 h holding. Although more characterizations are needed, it is safe to say that Gen2FC enabled Li-Ca-Si Zintl phase stabilized the interface and has positive influences on the calendar life of Li-ion batteries with Si anodes.

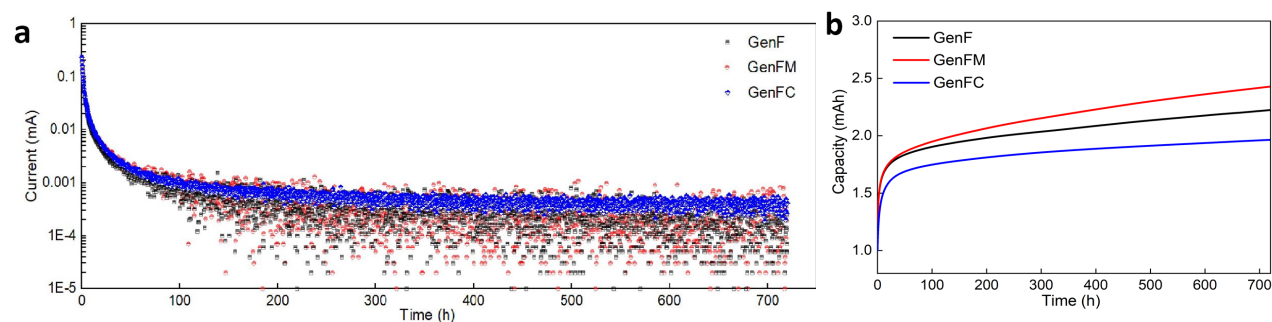


Figure II.I.A.37 Calendar life tests of Si622/LFP cells with GenF, Gen2FM, and Gen2FC electrolytes. (a) Current/time profile. (b) Capacity/time profile

Study of multivalent electrolyte additives (ternary Zintl chemistries) on CAMP pouch cells where we achieved better cyclability, higher coulombic efficiencies when compared to baseline electrolytes. An evaluation of electrode delamination identified as a major limitation on the long-term cycling effort which was partially overcome by higher pressure pouch cell design and lower cathode loadings. Examining silicon composition optimization studies (varying silicon, carbon and binder content) significantly improved capacity retention, cyclability, and calendar life. Lastly, with these optimized electrode compositions, silicon electrode calendar life studies showed significant improvements versus baseline with the advanced electrolyte additives with the Ca^{+2} system only showing a 6% increase in capacity over 700 h versus 28% increase for the baseline Gen2F electrolyte. Evaluation continues however data collected to date indicates that the growth in capacity lost to parasitic reactions will not eclipse the milestone guideline of 20% in the remaining time (goal ~1400h).

The active surface phase has been investigated by TEM, NMR, and XPS in order to better understand the formation mechanism of the Zintl phases. In this case an *in-situ* analytical technique, the Electrochemical Quartz Crystal Microbalance Measurement with Dissipation (EQCM-D), mode is applied to better understand the

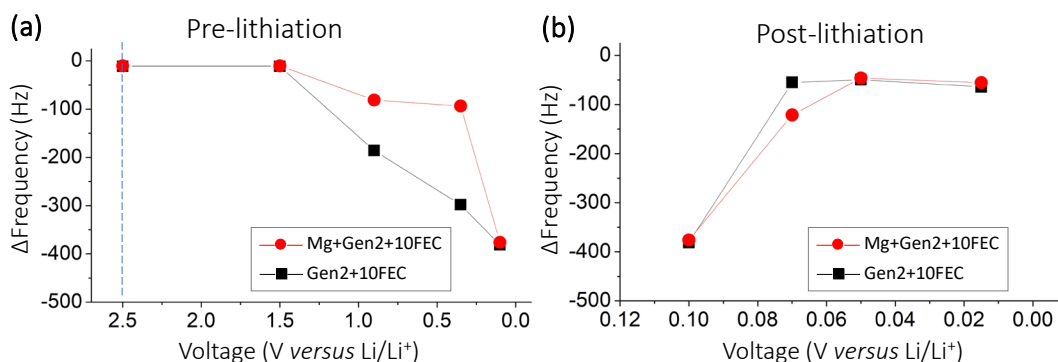


Figure II.I.A.38. Correlation of the lithiation voltage versus the frequency difference from the *in-situ* EQCM measurement on a 50 nm Si thin film referenced with lithium metal in Gen2F (black square) and Gen2FM (red circle) electrolyte. (a) pre-lithiation stage at $V > 350$ mV, (b) post-lithiation stage at $V < 350$ mV.

formation/growth of the SEI as a function of state of charge and additive. A Si thin film anode (50 nm) free of binder and conductive carbon is sputtered on a resonator and used as the working electrode with electrochemical signals referenced with Li metal. The frequency shift coupled with the electrochemical voltages in two electrolyte environments, Gen2F (Gen2+10%FEC) and Gen2FM (Gen2+10%FEC+0.2 M Mg(TFSI)₂) are presented in **Figure II.I.A.38**, where simultaneous electrochemical lithiation voltage from OCV = 2.5 V to 0.015 V is coupled with the corresponding frequency difference at the 3rd overtone. Two lithiation stages are monitored, the pre-lithiation process for SEI formation from 2.5 V to 350 mV and the post-lithiation stage from 350 mV to 15 mV. Results suggest before lithiation occurred (>350 mV), the frequency shift for the Gen2FM electrolyte is less significant than for the Gen2F electrolyte suggesting the SEI formation is less protuberant with the Mg addition in comparison with the Gen2F electrolyte. Frequency shift is mainly contributed from the electrolyte reduction as well as lithium insertion into surface SiO₂. For the post-lithiation stage (100 mV to 15 mV), frequency shift for the Gen2FM electrolyte at lowered voltage range from 100 mV to 50 mV is more significant than the Gen2F electrolyte and this trend is opposite in contrast to the pre-lithiation stage. Lithiation of Si into Li_{3.75}Si gives a mass increase of 48% of the reaction, however, formation of the Zintl phase and the magnesianation of Li_{3.75}Si into Li_{3.55}Mg_{0.1}Si phase merely gives a mass increase of 1.9%. Consequently, the apparently decreased frequency shift with the Mg addition occurring at lowered voltage range from 100 mV to 50 mV clearly suggests that a partial inclusion of Mg and formation of the Li-Mg-Si ternary taking place in parallel in addition to the lithiation of Si at these low voltages. At these points the silicon network has been broken down from a three dimensional solid to a molecular solid and appears to be capable of ion exchange and incorporating the magnesium ions.

Electrochemical performance of Si thin film anode with a 0.2 M Zn(TFSI)₂ and a 0.2 M Mg(TFSI)₂ as the electrolyte additives in the baseline electrolyte Gen2+10%FEC are studied and compared, presented in **Figure II.I.A.39**. Early stage SEI formation was more prominent with the Zn²⁺ additive in Gen2F electrolyte and SEI is suppressed with Mg²⁺ additive in the baseline electrolyte. Specifically, with the Zn²⁺ additive, no obvious current signal is detected for the first 2 electrochemical cycles suggesting no lithiation of Si. From OCV to lithiation at 0.4 V, capacitive current is detected without lithium intercalation. However, a mass accumulation is observed at the Si electrode indicative of the electrolyte reduction contributed SEI. Lithiation of Si started at lithiation potential from 0.4 V to 0.115 V, where clear intercalation and de-intercalation of Li is observed which correspond to reversible mass change. On the other hand, with the Mg²⁺ additive in the baseline electrolyte, it essentially prevents further SEI development at Si anode which is clearly indicated by the shift of the frequency. Thickness of the SEI in the Mg(TFSI)₂+Gen2+10%FEC electrolyte is about 50% of the SEI in a conventional Gen2+10%FEC electrolyte.

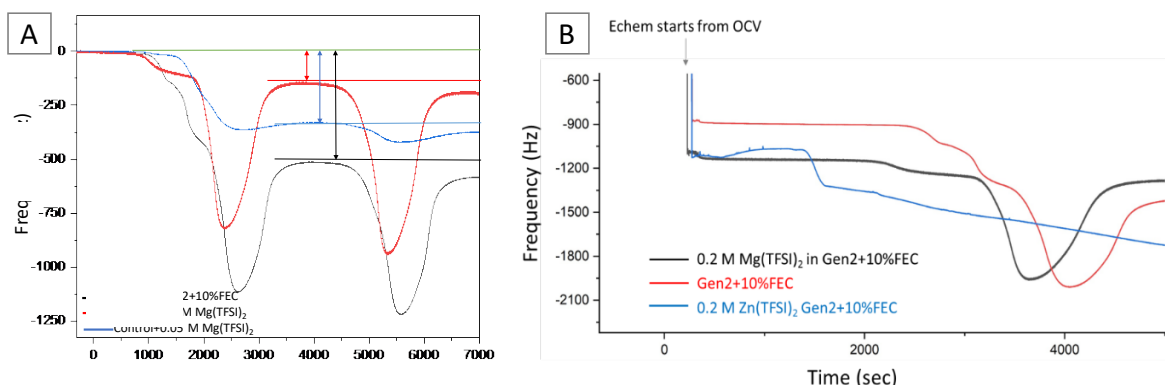


Figure II.I.A.39. In-situ early SEI formation at a Si thin film anode in different electrolytes based on the frequency shift (3rd overtone). (a) Gen2+10%FEC (black), 0.2 M Mg(TFSI)₂ in Gen2+10%FEC (red), and a 50 mM Mg(TFSI)₂ in Gen2+10%FEC (blue), (b) Frequency shift for the early SEI formation of a 0.2 M Zn(TFSI)₂ and a 0.2 M Mg(TFSI)₂ as electrolyte additives to the baseline electrolyte (Gen2+10%FEC) on a Si thin film anode. Lithiation depth is 0.115 V.

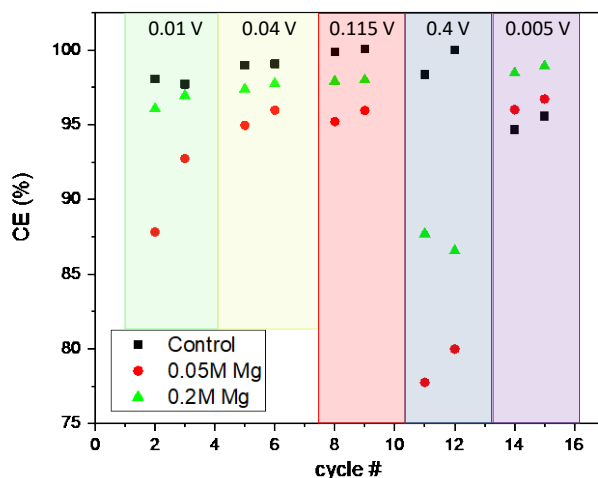


Figure II.I.A.40. Coulombic efficiency at lithiation depths of 5 mV, 10 mV, 40 mV, 115 mV, 400 mV in different electrolytes: baseline electrolyte Gen2+10%FEC (black), 50 mM Mg addition in baseline (red) and 200 mM Mg additive in baseline electrolyte (green).

Coulombic efficiency, an indication of the reversibility of lithiation, is evaluated at different lithiation depth at 5 mV, 10 mV, 40 mV, 115 mV to 400 mV in three different electrolytes, the baseline Gen2+10%FEC electrolyte (black square), a 50 mM Mg(TFSI)₂ in the baseline (red circle) and a 200 mM Mg(TFSI)₂ in the baseline (green triangle), presented in **Figure II.I.A.40**. Results suggest two important findings: (1) a higher CE is favored by the existence of Mg²⁺ in the electrolyte at low lithiation voltages, (2) a higher Mg concentration enables a higher CE at low lithiation voltages. These data are consistent with the testing studies reported earlier.

These EQCM-D studies allow us to quantify the early SEI formation for a Si thin film electrode with electrolytes with multivalent ion additives. Results suggest a suppressed early SEI with the presence of Mg²⁺ additive in electrolyte, and an enhanced SEI formation with the presence of Zn²⁺ additive in electrolyte. This is consistent with earlier studies by Han et al., where Zn was found to be electrochemically active (reduced to metal at 0.65V) and be more easily removed from the system. Results from the EQCM-D present an electrolyte dependent SEI formation mechanism with the Mg²⁺ additive in electrolyte stabilizing the Si interface upon formation of a compact SEI layer and enables a higher coulombic efficiency of Si anode at low lithiation voltages.

FEC & Temperature: In addition to the Zintl additives, temperature is known to have a significant impact on the performance and cycle lifetime of lithium-ion batteries (LiB) in the baseline electrolyte system. In the past year we have studied the effects of temperature on SEI formation and stability with and without 10wt% FEC additive in the Gen 2 electrolyte within the temperature range of 25 °C to 55 °C.

In FY20, we focused on the post-test analysis of Li-Si cells after the initial five cycles and compared the SEI properties at different temperatures with and without the FEC additive. **Figure II.I.A.41** shows the XPS data from the cycled Si rich anodes within the temperature range we tested.

The C1s spectrum at the surface consists essentially of five signals after peak deconvolution at all temperatures in both electrolytes. The line at 284.8eV corresponds to aliphatic carbon (C-C). The signal at 286.6eV can be assigned to carbon atoms in a one-oxygen environment (C-O). Based on the binding energy, it is more likely to consist of carbon atoms bound to an electron withdrawing group, as in R-C-OH (alcohols), R-C-O-C=O (esters) and C-O-COO (organic carbonate). Their presence is confirmed by the corresponding oxygen signals in the O1s spectrum. The peak at 287.8eV is assigned to a carbon atom doubly bound to one oxygen, as in ketones and aldehydes (R₂C=O, H-C=O) according to the literature. The peak at 289.6eV can be attributed to a carbon atom in a three-oxygen environment, such as Li₂CO₃ and organic carbonates. The signal at higher bonding energy, i.e., 290.5eV, might be related to the formation of polymeric fluoro-organic species (C_nF_m). The compound is also detected in the corresponding F1s spectrum. Overall, based on the decomposition reactions in EC/EMC system, we can assume the assigned SEI components at Si surface (C-O-C, C-OH, C-O-C=O, R₂C=O, C-OC(=O)O and C_nF_m) are most likely to be polymeric. These organic units can be connected to form aliphatic chains, as indicated by a relative higher contribution of aliphatic carbons in the C1s spectrum. This is supported by the results that the trend of contribution of CO_x species is similar in O1s spectra as that in the C1s emission.

The F1s spectrum of the Si surface shows three peak positions in both electrolytes. The first line at 684.5eV is assigned to LiF in agreement with most references. The peak appearing at 686.2eV can be attributed to Li_xPO_yF_z, based on the component assigned in the P2p spectra. The peak at 687.8eV is related to the formation of R-F (fluoro-organic species: C_nF_m, F-O-Si). XPS analysis shows the contribution of each component is quite different with/without the presence of FEC. SEI layer on anodes with FEC is primarily composed of LiF because the fluorinated ethylene carbonate (FEC) decomposes before EC and EMC. Overall, we can observe less temperature-sensitivity of SEI chemistry in the Si-rich cell with FEC, implying the SEI is more stable with the additive.

Figure II.I.A.42 shows the atomic percentage (at%) of the major SEI components, C, O, and F, on the Si surface that were calculated from XPS survey scans. The results clearly show less carbonate (C, O) and more F species formed on the surface with FEC, confirming FEC can suppress EC/EMC decomposition to some extent at the first 5 cycles. It is interesting to note that surface content of C, O, and F increases as temperatures increases from 25° to 45°C, but at 55°C, the values drop. This also is confirmed by lower peak intensity of C-O and C=O in C1s spectra in Figure II.I.A.39, indicating fewer organic carbonates were formed at 55°C, particularly for the anode without FEC. In addition, there is an increase in fluorophosphates at this temperature. It might be due to the kinetics of SEI formation were enhanced and the partial decomposition of SEI components at this high temperature.

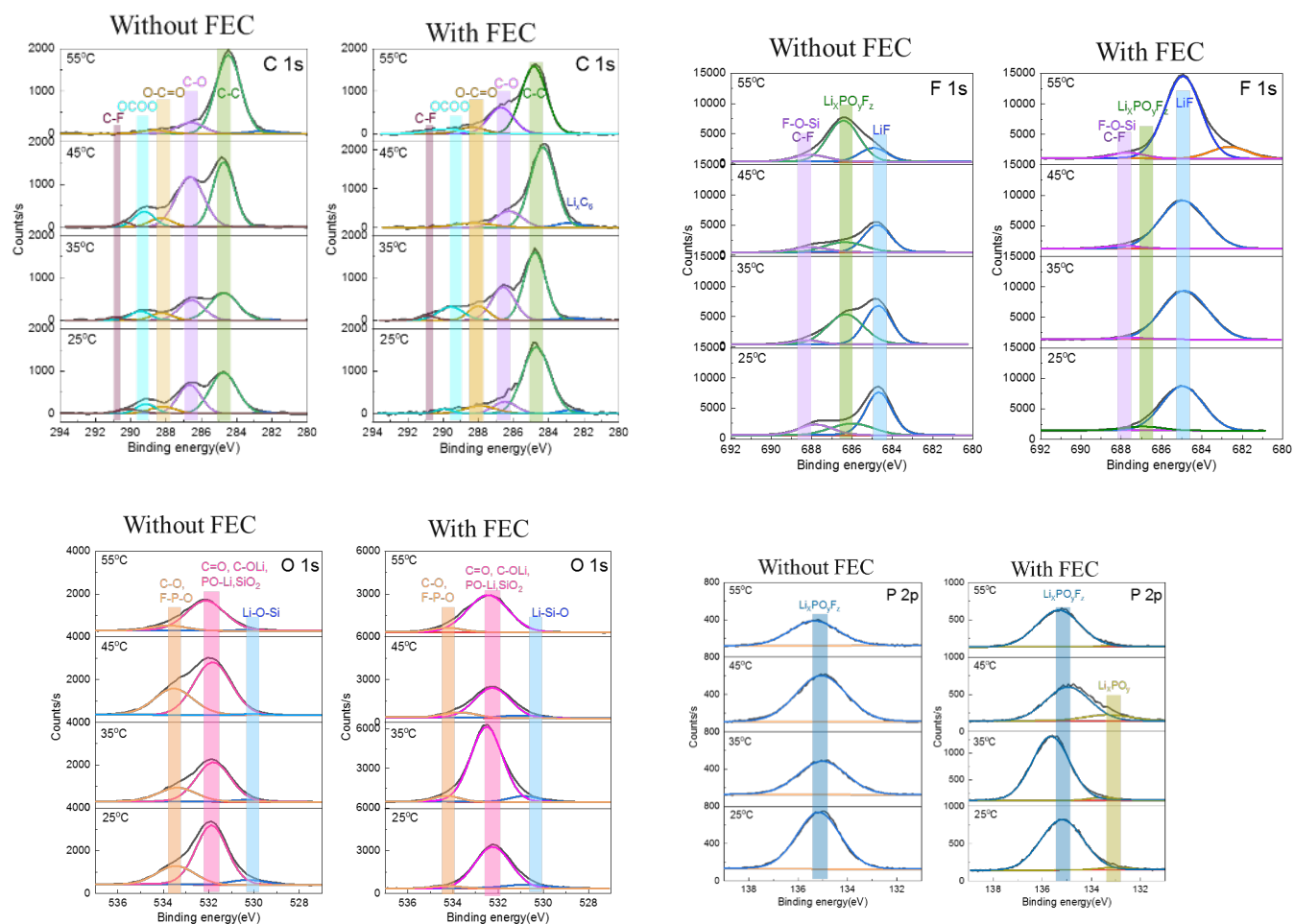


Figure II.I.A.41. C1s, F1s, O 1s, and P2p XPS spectra of Si anodes after 5 cycles in the temperature range from 25°C to 55°C with and without 10 wt% FEC in Gen 2 electrolyte.

From these studies, SEI formation and stability with and without FEC additive at different temperatures was investigated in high-Si content half cells by XPS and showed different SEI chemical species formed in the FEC-containing cells. Notably fewer organic species and more LiF observed in Si-rich with FEC addition. As result, cells with FEC showed less temperature-sensitivity of SEI chemistry when compared to the cells in Gen 2 only.

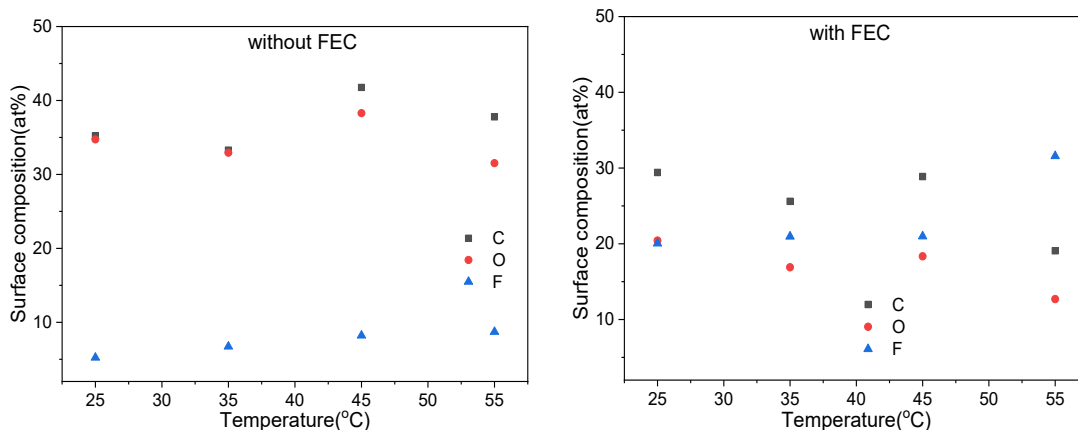


Figure II.I.A.42. The atomic percentage (at%) of the major SEI components at the Si surface after 5 cycles

SEI Solubility: When assessing the stability of the SEI layer, previous efforts have identified dissolution and reformation as a components of silicon chemistry not seen in graphitic systems. This has been highlighted in the year using EQCM, XPS, and SECM studies who have assessed the stability of electrode level silicon baseline materials on cycling and determine the range of species that solubilize and leach into the electrolyte. To assess the dissolving materials, new analytical tools were adapted to determine the types of species that are found in the electrolyte as solubilized SEI products. For the solid silicon SEI components identified in the literature, research efforts have identified several polymerized ring-opened solvents (FEC, EC), various salts including inorganic (Li_2CO_3) and coordination salts (i.e. LiEDC). Notably the latter, identified by the Ross Group at LBNL, has been seen to be a significant component that appears to have spectroscopic handles that allow its identification in the solid SEI films. LiEDC was later synthesized and found to form readily and, once purified, be insoluble in the solvents commonly used on out electrolytes. The insoluble nature of the materials makes identification and isolation more straightforward. However, in the silicon systems under study, it has been noted that the SEI layers on the anode are not dimensionally stable. On cycling the height, thickness, and weight of the SEI have been observed to change as a function of state of charge (SOC). Using Rotating Ring Disk Electrochemistry (RRDE), it has been seen that the SEI appears to show the most dramatic changes in volume above 450 mV (vs Li) while has seen dramatic weight and density shifts using EQCM-D. As the weight is changing as a function of state of charge, the conclusion drawn is that species in the SEI are oxidizing near those voltages and becoming soluble. Identification of these species is important as soluble species in the electrolyte may re-reduce on charge, and precipitate on the anode, transfer to the cathode and further react, or possibly change the transfer kinetics of the lithium cations in the electrolyte. In this case EC (or FEC) was seen to degrade as it accepted electrons from the reduced silicide on contact. Although made in a controlled environment, the exact nature of the reduced species was not identified, although the C-F bond in the FEC was maintained. A similar observation was seen with PVDF binders, where C-F bonds were stable and degradation reactions occurred at polymerization defects ($-\text{CH}_2-\text{CH}_2-$) rather than at random spots.

RRDE methods have been applied to solubilized species coming off as degradation products using a Si thin film cell. Earlier work (FY19) highlighted technique development efforts using redox mediators to track SEI conductivity vs SOC, the role of surface charge carrier, and FEC electrolyte additives. Work with FEC noted that measurable redox active species are coming off of 70% Si drop-cast electrode at SEI formation and during simultaneous sweep at the Pt ring electrode, in addition the FEC (via its film formed) was playing a role of surface passivation to these species, suggesting classic pre-passivation of the Si SEI.

For solubilized species, LBNL has been focused on the development of techniques to isolate and identify soluble SEI species. The work has two focus areas – a post-cycling gradient wash technique that uses polarity to solubilize and separate species formed but trapped in the SEI and FTIR, a spectroscopic technique useful for identification of organic species. The gradient solvent wash was developed with his group to isolate and identify species that formed but due to isolation techniques were often mixed. Using mixtures of ethyl acetate and hexane, he was able to create a gradient of polarity that selectively dissolved out species in the SEI by their relative ionicity, salts, to alcohols, to simple oligomeric species. MALDI data is shown in Figure II.I.A.44. Earlier work (FY19Q2-FY20Q2) reported on its utility for test cells (Cu with Gen2, VC), with future work using FEC species and assessing the differences in SEI between species generated in Gen2, Gen2/FEC, and Gen2/FEC/Zintl additives.

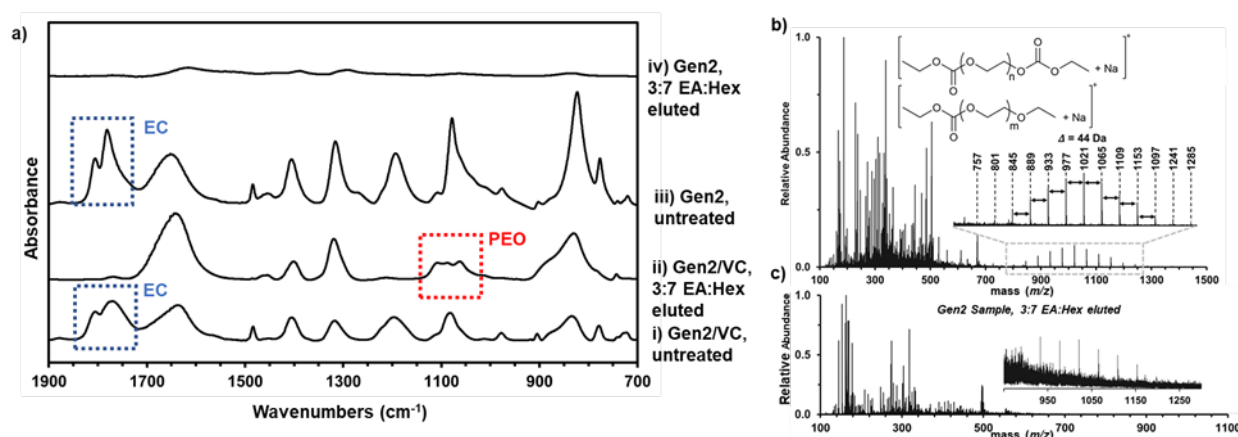


Figure II.I.A.44. a) FTIR spectra of untreated and treated electrodes cycled with and without VC. b) MALDI spectrum of electrode cycled with Gen2/VC after 3:7 EA:Hex treatment. c) MALDI spectrum of electrode cycled with Gen2 after 3:7 EA:Hex treatment. (Inserts are zoom-in spectra of PEO regions.)

The feasibility of this methodology has been fully demonstrated with Cu model electrodes, and the decomposition reaction of both electrolyte and additive molecules have been unambiguously characterized. In addition, these techniques have also been applied to actual SiO₂ and graphite composite electrodes, which delivered comparable results as those on Cu model electrodes, thus endorsing the universality of on-electrode chromatography and MALDI techniques.

Crossover: As well as species related to SEI dissolution being added to the electrolyte on cycling, crosstalk between cathode and anode in full cell system can have a significant impact on performance and cycle life for lithium-ion batteries (LIB). While this has been investigated for graphite anode systems where issues with catalytic decomposition of the SEI by the transported transition metal species are noted, similar studies for the Si-SEI in a full cell have not been investigated. To better understand if the Si SEI reacts differently than the graphite SEI to transition metal impurities, cells using a Si-rich (Si 80%/Graphite 20%) anode coupled with one

of the following cathodes, LiCoO_2 (LCO), $\text{LiNi}_{0.5}\text{Mn}_{0.3}\text{Co}_{0.2}$ (NMC532), or LiFePO_4 (LFP) in a full cell were investigated. We analyzed electrolyte decomposition products by HPLC/ESI-MS and SEI chemistry of the aged Si anodes by XPS. Finally, we compared the different aging properties of the Si anodes in each full cell.

We focused on the post-test analysis of Si-rich full cells after initial 5 cycles (3 formation cycles at C/20, an HPPC cycle, 2 aging cycles at C/3, an HPPC cycle). Three full cells were used: LCO-Si, NMC532-Si, LFP-Si cells were prepared. The voltage window was 3.0-4.1V for LCO-Si and NMC532-Si cells, and 2.7-3.7V for LFP-Si cell. Gen2 electrolyte was used. After 5 cycles, we compared electrolyte decomposition products by HPLC/ESI-MS analysis, the SEI chemistry of each aged Si anode by XPS, and electrochemical properties of each aged Si anode.

Figure II.I.A.45 shows total ion chromatograms (TICs) of fresh Gen2 electrolyte and aged electrolytes extracted from three different full cells after 5 cycles. Compared with TICs of Gen2 electrolyte, many different peaks are observed in TICs of the three aged electrolytes. This indicates the detection of multiple decomposition species from Gen2 electrolyte. Overall TICs of each aged electrolyte look similar, but several unique peaks are also visible in each electrolyte. This means that there are different decomposition species in each aged electrolyte. **Table II.I.A.6** shows most intense ions in each electrolyte detected by HPLC/ESI-MS. Each electrolyte has many kinds of unique organic species, and there are a few organic species which are commonly observed in all samples (marked by blue) or in all aged electrolytes (marked by orange). Compared with the aged electrolytes from LCO-Si and NMC532-Si, the LFP-Si electrolyte has more organophosphate or organo(fluoro)phosphate species, indicative of more reactions involving PF_5 (in LiPF_6) in Gen2 electrolyte. Together, the results indicate that each of the electrolytes followed different decomposition routes, depending on cathode materials.

Different electrolyte decomposition mechanisms can lead to different SEI chemistry on the aged Si anodes in

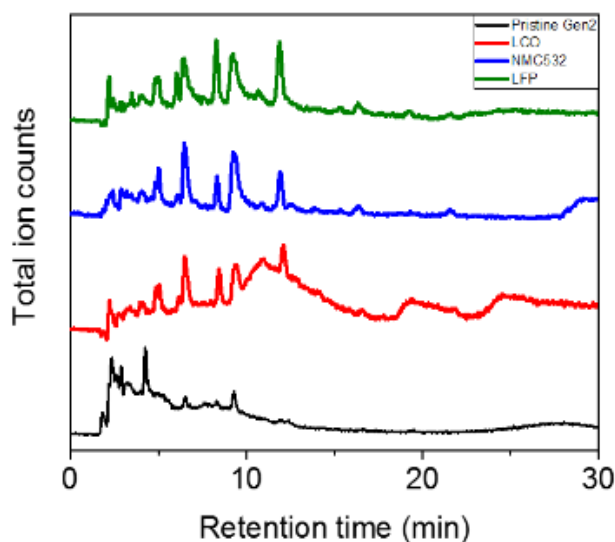


Figure II.I.A.45. TICs of fresh Gen2 electrolyte and aged electrolytes extracted from three full cells, obtained via HPLC/ESI-MS.

each full cell. **Figure II.I.A.46** shows XPS results of the aged Si anodes in three full cells after the initial five cycles. The results clearly show that SEI chemistry on each aged Si anode is also different.

The C1s spectrum of the aged electrolyte from LCO-Si full cell consist of 4 signals. The peak at 284.8eV corresponds to aliphatic carbon (C-C). The peak at 283.2eV is assigned to lithiated carbon as a result of lithiation

of graphite in the Si-rich electrode. Small peaks at 286.3eV and 288.4eV can be assigned to carbon atoms in a one-oxygen environment (C-O) and carbon atoms bound to an electron withdrawing group, like R-C-O-C=O (esters). While the C1s spectra of the both aged electrolytes from NMC532-Si and LFP-Si are quite different from that of LCO-Si. In both electrolytes, the C-O peak at 286.3eV is significantly stronger, and a new peak at 289.7eV that can be assigned to organic carbonate species (C-O-COO) is observed. Overall, the results show that SEI chemistry of aged Si anode from NMC532-Si or LFP-Si full cells consists of more organic species than the LCO-Si full cell.

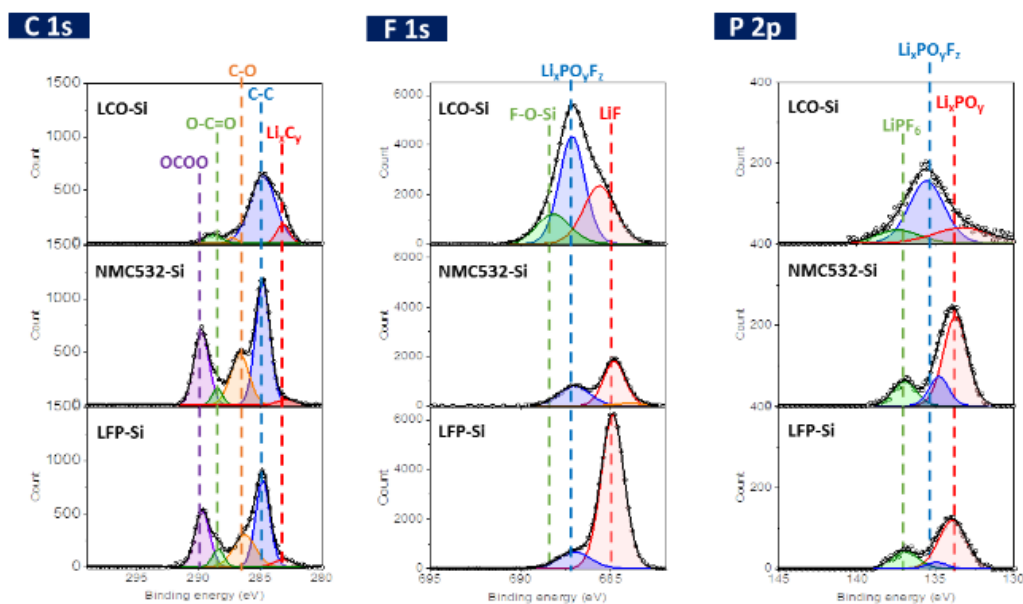


Figure II.I.A.46. C1s, F1s, and P2p XPS spectra of aged Si anodes from three full cells, after 5 cycles.

The F1s spectra of each aged Si anode are also different. In the aged Si from LCO-Si full cell, three peaks were observed. The peak at 684.9eV is assigned to LiF, in agreement with most references. The most intense peak at 687eV can be attributed to $\text{Li}_x\text{PO}_y\text{F}_z$. This could be supported by P2p spectrum. The peak at 688.2eV is related to the formation of R-F (fluoro-organic species: C_nF_m , F-O-Si). While the F1s spectra of aged electrolytes from NMC532-Si and LFP-Si are primarily composed of LiF. The peak assigned to $\text{Li}_x\text{PO}_y\text{F}_z$ is smaller, and the peak related to fluoro-organic species was not observed in both electrolytes. The smaller amount of $\text{Li}_x\text{PO}_y\text{F}_z$ could indicate that hydrolysis of LiPF_6 was suppressed in NMC532-Si or LFP-Si full cells.

The different crosstalk behavior in each full cell can lead to different degradation of each Si anode after 5 cycles. We prepared the aged Si anode/Li half-cell and compared their electrochemical properties. **Figure II.I.A.47** shows the 1st cycle voltage profiles of the half-cells. The three half-cells show very similar 1st discharge capacities but show different coulombic efficiency (CE) and irreversible capacity. The half-cell rebuilt from the aged silicon anode from the LCO-Si full cell shows the lowest CE at 67%, while the rebuilt half-cell from the LFP-Si full cell shows a very high CE at 93%. This, at this point in the analysis, infers that the stability of the LFP/Si SEI is higher than that seen for NMC532 or LCO cells as each cell was found to have different electrolyte chemistry within five cycles.

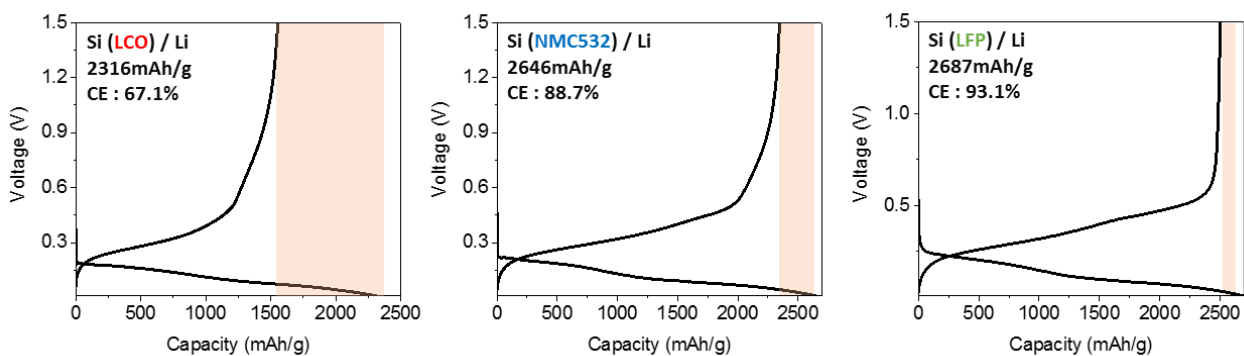


Figure II.I.A.47. The 1st cycle voltage profiles of each aged Si (from LCO-Si, NMC532-Si, LFP-Si) /Li half-cells. Red square means irreversible capacity of each half-cell.

Table II.I.A.6. Most intense ions detected via HPLC/ESI-MS

		m/z	M.W
Gen2 electrolyte	$[\text{C}_2\text{H}_6\text{O}]\text{Na}^+$	69	46
	$[\text{C}_3\text{H}_4\text{O}_3]\text{H}^+ : \text{EC}$	89	88
	$[\text{C}_2\text{H}_5\text{O}_4\text{P}]\text{H}^+$	125	124
	$[\text{C}_6\text{H}_{10}\text{O}_4\text{F}_2]\text{H}^+$	185	184
	$[\text{C}_7\text{H}_{12}\text{O}_6]\text{Na}^+$	215	192
	$[\text{C}_9\text{H}_{13}\text{O}_8\text{P}_1]\text{Na}^+$	303	280
Aged electrolyte (LCO-Si)	$[\text{C}_3\text{H}_4\text{O}_3]\text{H}^+ : \text{EC}$	89	88
	$[\text{C}_7\text{H}_{12}\text{O}_6]\text{Na}^+$	215	192
	$[\text{C}_6\text{H}_{11}\text{O}_7\text{P}_1\text{F}_2]\text{H}^+$	265	264
	$[\text{C}_9\text{H}_{11}\text{O}_8\text{P}_1]\text{H}^+$	279	278
	$[\text{C}_8\text{H}_9\text{O}_5\text{P}_1\text{F}_4]\text{H}^+$	293	292
	$[\text{C}_9\text{H}_{13}\text{O}_8\text{P}_1]\text{Na}^+$	303	280
	$[\text{C}_9\text{H}_{11}\text{O}_9\text{P}_1]\text{Na}^+$	317	294
	$[\text{C}_3\text{H}_4\text{O}_3]\text{H}^+ : \text{EC}$	89	88

Aged electrolyte (NMC532-Si)	$[\text{C}_4\text{H}_6\text{O}_3]\text{H}^+$	103	102
	$[\text{C}_8\text{H}_7\text{O}_6\text{F}_3]\text{H}^+$	257	256
	$[\text{C}_9\text{H}_{11}\text{O}_8\text{P}_1]\text{H}^+$	279	278
	$[\text{C}_8\text{H}_{11}\text{O}_7\text{P}_1\text{F}_2]\text{H}^+$	289	288
	$[\text{C}_9\text{H}_{11}\text{O}_9\text{P}_1]\text{H}^+$	295	294
	$[\text{C}_9\text{H}_{13}\text{O}_8\text{P}_1]\text{Na}^+$	303	280
	$[\text{C}_{10}\text{H}_{14}\text{O}_{10}\text{P}_1\text{F}_1]\text{Na}^+$	367	344
Aged electrolyte (LFP-Si)	$[\text{C}_5\text{H}_7\text{O}_4\text{P}_1\text{F}_2]\text{H}^+$	201	200
	$[\text{C}_7\text{H}_4\text{O}_4\text{F}_4]\text{H}^+$	229	228
	$[\text{C}_8\text{H}_7\text{O}_6\text{F}_3]\text{H}^+$	257	256
	$[\text{C}_9\text{H}_{11}\text{O}_8\text{P}_1]\text{H}^+$	279	278
	$[\text{C}_8\text{H}_{11}\text{O}_7\text{P}_1\text{F}_2]\text{H}^+$	289	288
	$[\text{C}_8\text{H}_9\text{O}_5\text{P}_1\text{F}_4]\text{H}^+$	293	292
	$[\text{C}_9\text{H}_{11}\text{O}_9\text{P}_1]\text{H}^+$	295	294
	$[\text{C}_9\text{H}_{13}\text{O}_8\text{P}_1]\text{Na}^+$	303	280
	$[\text{C}_{13}\text{H}_{13}\text{O}_9\text{P}_1\text{F}_2]\text{Na}^+$	405	382

Section Conclusion: In this section, calendar life and cycle testing were judged based on various electrolyte additives and SEI decomposition products, materials that may cause film formation or organic coatings within the cell. From the analysis of the data, significant improvements in calendar life were seen upon addition of alkaline earth cations to the cell's electrolyte. Previous work had highlighted that the insertion mechanism occurs at low voltage and that the extent of Ca or Mg addition was time dependent based on time at the pertinent voltages and diffusion of the metals from the electrolyte to form a ternary Li-M-Si surface phase. As noted by the SEISTA LBNL team (AMR, June 2020) this surface coating severely restricts the parasitic currents associated with charged silicon electrodes. This was consistent with the model that showed that the surface was deactivated for redox processes by the formation of the ternary phase. In this year we were able to show that for a calendar life study, the addition of Ca salts to the electrolyte with formation of a Li-Ca-Si ternary Zintl phase decreased capacity losses by 80% after 700h of evaluation compared to a Gen2F baseline. EQCM data from the Sa group at UMass-Boston was consistent with those results and highlighted their conclusion that the SEI in those ternary systems was thinner and more compact than baseline. For full cell cycling evaluation, Zintl additive testing was shown to raise the CE in cells tested and optimization of the Si to C ratio was found to have a strong correlation

with cycling life, with cells < 80% Si cycling better using the SCP protocol, but with a best performance (highest stable capacity) seen for a 70% Si/ 10% C45 / 20% LiPAA binder design.

In terms of SEI stability, while the EQCM data showed the SEI to be more compact with Zintl salt addition, previous studies had shown the Si SEI to be unstable towards dissolution. This may be related to catalytic effects of the cathode towards the electrolyte (or Si SEI) where we showed LCO actively altered the electrolyte, gradual dissolution of species that polymerize in solution (or on the cathode), or loss of species to oxidative breakdown as the cell voltage cycles. RRDE studies highlight that the Si SEI thins out significantly near 400 mV (vs Li) leaving most of the inorganic species on the anode but losing some of the small molecule organic components.

4. Key Publications

- Hays, KA, Armstrong, B, Veith, GM “Ending the Chase for a Perfect Binder: Role of Surface Chemistry Variation and its Influence on Silicon Anodes” *ChemElectroChem*, **7**, 3790 (2020).
- Burdette-Trofimov, MK, Armstrong, BL, Rogers, AM, Heroux, L, Doucet, M., Yang, G, Phillip, ND, Kidder, MK, Veith, GM “Understanding Binder-Silicon Interactions during Slurry Processing” *J. Phys Chem C.*, **124** 13479 (2020).
- Liu, Q., Jiang, W., Munoz, MJ, Liu, Y., Yang, ZZ, Bloom, I., Dzwiniel, T., Li, Y., Pupek, K., Zhang, ZC “Stabilized Electrode/Electrolyte Interphase by a Saturated Ionic Liquid Electrolyte for High-Voltage NMC532/Si-Graphite Cells” *ACS Appl Mat Interfaces*, **12**, 23035 (2020).
- Coyle, J., Brumbach M., Veith G., Appblett C., “Investigating the Chemical Reactivity of Lithium Silicate Model SEI Layers” *J. Phys Chem C.*, **124**, 8153 (2020).
- Seitzinger, CL, Sacci, RL, Coyle, JE, Appblett, CA, Hays, K., Armstrong, RR, Rogers, AM, Armstrong, BL, Bennet, TH, Neale, N., Veith, G. “Intrinsic Chemical Reactivity of Silicon Electrode Materials: Gas Evolution” *Chem Materials*, **32**, 3199 (2020).
- Jiang, S.S., Hu, B., Shi, Z., Chen, W., Zhang, Z., Zhang, L. “Re-Engineering Poly(Acrylic Acid) Binder toward Optimized Electrochemical Performance for Silicon Lithium-Ion Batteries: Branching Architecture Leads to Balanced Properties of Polymeric Binders” *Adv Functional Mat* **30**, 1908558 (2020).
- Kirner, J., Qin, Y., Zhang, L., Jansen, A., Lu, WQ “Optimization of Graphite-SiO blend electrodes for lithium ion batteries: Stable cycling enabled by single-walled carbon nanotube conductive additive” *J. Power Sources*, **450**, 227711 (2020).
- Browning, K., Sacci, R., Doucet, M., Browning, J., Kim, J., Veith G. “The Study of the Binder Poly(acrylic acid) and Its Role in Concomitant Solid-Electrolyte Interphase Formation on Si Anodes” *ACS Appl Mat Interfaces*, **12**, 10018 (2020).
- Piernas-Munoz, M., Trask, SE, Dunlop, A., Lee, E., Bloom, I. “Effect of temperature on silicon-based anodes for lithium-ion batteries” *J. Power Sources*, **441**, 227080 (2020).
- Rago, N., Basco, J., Vu, A., Li, J., Hays, K., Sheng, Y., Wood, D., Bloom, I. “Effect of formation protocol: Cells containing Si-Graphite composite electrodes” *J. Power Sources.*, **435** 126548 (2019).
- Jiang, SS, Hu, B, Sahore, R, Liu, HH, Pach, GF, Carroll, GM, Zhang, L , Zhao, B, Neale, NR, Zhang, ZC “Tailoring the Surface of Silicon Nanoparticles for Enhanced Chemical and Electrochemical Stability for Li-Ion Batteries” *ACS Appl Energy Mat*, **2** 6176 (2019).
- Hu, B., Jiang, S., Shkrob, I., Zhang, S., Zhang, J., Zhang, Z., Zhang, L. “Poly(4-vinylbenzoic acid): A Re-Engineered Binder for Improved Performance from Water-Free Slurry Processing for Silicon Graphite Composite Electrodes” *ACS Appl Energy Mat*, **2**, 6348 (2019)
- Bloom, I., Rago, N., Zheng, Y., Li, J., Wood, D., Steele, L., Lamb, J., Spanger, S., Grosso, C., Fenton, K. “Effect of overcharge on lithium-ion cells: Silicon/graphite anodes” *J. Power Sources*, **432**, 73 (2019).
- Han, B., Liao, C., Dogan F., Trask, S., Lapidus, S., Vaughey J., Key, B. “Using Mixed Salt Electrolytes to Stabilize Silicon Anodes for Lithium-Ion Batteries via in Situ Formation of Li-M-Si Ternaries (M = Mg, Zn, Al, Ca)” *ACS Appl Mat Interfaces*, **11**, 29780 (2019)
- Gao, X., Lu, WQ., Xu, J. “Modeling framework for multiphysics-multiscale behavior of Si-C composite anode” *J. Power Sources*, **449**, 227501 (2020).

5. References

- [1] Haiping Jia, Xiaolin Li, Junhua Song, Xin Zhang, Langli Luo, Yang He, Binsong Li, Yun Cai, Shenyang Hu, Xingcheng Xiao, Chongmin Wang, Kevin M. Rosso, Ran Yi, Rajankumar Patel, Ji-Guang Zhang “Hierarchical porous silicon structures with extraordinary mechanical strength as high performance lithium-ion battery anodes” *Nature Communications* **11** 1474 (2020).
- [2] Binghong Han, Maria Jose Piernas-Muñoz, Fulya Dogan, Joseph Kubal, Stephen E. Trask, Ira D. Bloom, John T. Vaughey, Baris Key “Probing the Reaction between PVDF and LiPAA vs Li7Si3: Investigation of Binder Stability for Si Anodes” *Journal of The Electrochemical Society*, **166** A2396-A2402 (2019).
- [3]. H. Wu, Y. Cui” Designing nanostructured Si anodes for high energy lithium ion batteries” *Nano Today* **7**, 414-429 (2012)
- [4] Bing Hu., I. Shkrob, S. Zhang, L. Zhang, J. Zhang, Y. Li, C. Liao. Z. Zhang, W. Lu, L. Zhang “Understanding of pre-lithiation of poly(acrylic acid) binder: Striking the balances between the cycling performance and slurry stability for silicon-graphite composite electrodes in Li-ion batteries” *J. Power Sources* **416**, 125-131 (2019)
- [5] F. Erogbogbo, T. Lin, P. Tucciarone, K. LaJoie, L.Lai, G. Patki, P. Prasad, M. Swihart “On-Demand Hydrogen Generation using Nanosilicon: Splitting Water without Light, Heat, or Electricity” *Nano Lett*, **13(2)**, 451-456 (2013)
- [6] M. Olszak-Humienik ”On the Thermal Stability of some Ammonium Salts” *Thermochimica Acta* **378**, 107-112 (2001).
- [7] Allen, C. L., Chhatwal, A. R., Williams, J. M. J.,” Direct amide formation from unactivated carboxylic acids and amines” *Chemical Communications* **48** (5), 666-668 (2012)
- [8] Pekarek, R. T., Affolter, A., Baranowski, L. L., Coyle, J., Hou, T., Sivonxay, E., Smith, B. A., McAuliffe, R. D., Persson, K. A., Key, B., Apblett, C., Veith, G. M., Neale, N. R., “Intrinsic chemical reactivity of solid-electrolyte interphase components in silicon–lithium alloy anode batteries probed by FTIR spectroscopy” *J. Mater. Chem. A*, **8**, 7897-7906 (2020)
- [9] Hou, T., Yang, G., Rajput, N. N., Self, J., Park, S.-W., Nanda, J., Persson, K. A. “The influence of FEC on the solvation structure and reduction reaction of LiPF6/EC electrolytes and its implication for solid electrolyte interphase formation” *Nano Energy*, **64**, 103881 (2019)
- [10] Flores-Zamora, M. I., Martinez-Perez, C. A., Garcia-Guaderrama, M., Estrada-Guel, I., Espinosa-Magana, F., Martinez-Sanchez, R. "Comparative Study of Al-Ni-Mo Alloys Obtained by Mechanical Alloying in Different Ball Mills" *Rev. on Adv. Mater. Science* **18** (3), 301-304 (2008)
- [11] Hernandez-Martinez, S. E., Cruz-Rivera, J. J., Garay-Reyes, C. G., Martinez-Sanchez, R., Estrada-Guel, I., Hernandez-Rivera, J. L., Comparative Study of Synthesis of AA 7075-ZrO₂ Metal Matrix Composite by Different Mills. *J. Alloys Compd.* **643**, S107-S113 (2015).
- [12] Krycer, I., Hersey, J. A., A Comparative-Study of Comminution in Rotary and Vibratory Ball Mills *Powder Technol.* **27** (2), 137-141 (1980).
- [13] Martinez, Y. R., Alcazar, G. A. P., Rodriguez, H. B., Lozano, D. O., Comparative Study by MS and XRD of Fe₅₀Al₅₀ Alloys Produced by Mechanical Alloying, Using Different Ball Mills. *Hyperfine Interact.* **161**, 191-195 (2005)
- [14] Westphal, B. G., Kwade, A., Critical Electrode Properties and Drying Conditions Causing Component Segregation in Graphitic Anodes for Lithium-Ion Batteries. *J. Energy Storage* **18**, 509-517 (2018)

- [15] Kasinathan, R., Marinaro, M., Axmann, P., Wohlfahrt-Mehrens, M., Influence of the Molecular Weight of Poly-Acrylic Acid Binder on Performance of Si-Alloy/Graphite Composite Anodes for Lithium-Ion Batteries. *Energy Technol.* **6**, 2256-2263 (2018)
- [16] Li, C. C., Lee, J. T., Peng, X. W., Improvements of Dispersion Homogeneity and Cell Performance of Aqueous-Processed LiCoO₂ Cathodes by Using Dispersant of PAA-NH₄. *J. Electrochem. Soc.* **153** (5), A809-A815 (2006)
- [17] Li, J. L., Armstrong, B. L., Daniel, C., Kiggans, J., Wood, D. L., Optimization of Multicomponent Aqueous Suspensions of Lithium Iron Phosphate (LiFePO₄) Nanoparticles and Carbon Black for Lithium-Ion Battery Cathodes. *J. Colloid Interface Sci.* **405** 118-124 (2013)
- [18] Li, J. L., Armstrong, B. L., Kiggans, J., Daniel, C., Wood, D. L., Optimization of LiFePO₄ nanoparticle suspensions with polyethyleneimine for aqueous processing. *Langmuir* **28**(8), 3783-3790 (2012)
- [19] Li, J. L., Armstrong, B. L., Kiggans, J., Daniel, C., Wood, D. L., Lithium ion Cell Performance Enhancement Using Aqueous LiFePO₄ Cathode Dispersions and Polyethyleneimine Dispersant. *J. Electrochem. Soc.* **160** (2), A201-A206 (2013).
- [20] Hatchard, T. D., Dahn, J. R., In situ XRD and Electrochemical Study of the Reaction of Lithium with Amorphous Silicon. *J. Electrochem. Soc.* **151** (6), A838-A842 (2004).
- [21] Obrovac, M. N., Christensen, L., Structural Changes in Silicon Anodes During Lithium Insertion/Extraction. *Electrochem. Solid-State Lett.* **7** (5), A93-A96 (2004).
- [22] Obrovac, M. N., Krause, L. J., Reversible Cycling of Crystalline Silicon Powder. *J. Electrochem. Soc.* **154** (2), A103-A108.(2007)
- [23] Burdette-Trofimov, M. K., Armstrong, B. L., Rogers, A. M., Heroux, L., Doucet, M., Yang, G., Phillip, N. D., Kidder, M. K., Veith, G. M., Understanding Binder-Silicon Interactions During Slurry Processing. *J. Phys. Chem. C* **124** (24), 13479-13494 (2020).
- [24] Debye, P., The Intrinsic Viscosity of Polymer Solutions. *J. Chem. Phys.* **14** (10), 636-639 (1946).
- [25] Krigbaum, W. R., Flory, P. J., Molecular Weight Dependence of the Intrinsic Viscosity of Polymer Solutions .2. *J. Polym. Sci.* **11** (1), 37-51 (1953).
- [26] Staikos, G., Bokias, G., The Intrinsic-Viscosity of Poly(acrylic acid) and Partially Neutralized Poly(acrylic acid) by Isoionic Dilution. *Polym. Int.* **31** (4), 385-389 (1993)
- [27] Busse, W. F., Longworth, R., Effect of Molecular Weight Distribution and Branching on the Viscosity of Polyethylene Melts. *J. Polym. Sci.* **58**(166), 49-69 (1962)
- [28] Schreiber, H. P., Bagley, E. B., The Newtonian Melt Viscosity of Polyethylene: An Index of Long-Chain Branching. *J. Polym. Sci.* **58**, 29-48 (1962)
- [29] Hammouda, B., Solvation Characteristics of a Model Water-Soluble Polymer. *J. Polym. Sci. Pol. Phys.* **44** (22), 3195-3199 (2006).
- [30] Hammouda, B., Ho, D. L., Kline, S., Insight into Clustering in Poly(ethylene oxide) Solutions. *Macromolecules* **37** (18), 6932-6937 (2004)
- [31] Huang, B. S., Zhang, Y., Shu, X., Liu, Y., Penumadu, D., Ye, X. P., Neutron Scattering for Moisture Fetection in Foamed Asphalt. *J. Mater. Civil Eng.* **25**(7), 932-938 (2013)

- [32] Hule, R. A., Nagarkar, R. P., Altunbas, A., Ramay, H. R., Branco, M. C., Schneider, J. P., Pochan, D. J., Correlations Between Structure, Material Properties and Bioproperties in Self-Assembled Beta-Hairpin Peptide Hydrogels. *Faraday Discuss.* **139**, 251-264 (2008).
- [33] Lee, J. H., Ruegg, M. L., Balsara, N. P., Zhu, Y. Q., Gido, S. P., Krishnamoorti, R., Kim, M. H., Phase Behavior of Highly Immiscible Polymer Blends Stabilized by a Balanced Block Copolymer Surfactant. *Macromolecules* **36**(17), 6537-6548 (2003)
- [34] Yang, Z., Hemar, Y., Hilliou, L., Gilbert, E. P., McGillivray, D. J., Williams, M. A. K., Chaieb, S., Nonlinear Behavior of Gelatin Networks Reveals a Hierarchical Structure. *Biomacromolecules* **17** (2), 590-600 (2016).
- [35] Pagac, E. S., Tilton, R. D., Prieve, D. C., Depletion Attraction Caused by Unadsorbed Polyelectrolytes. *Langmuir* **14** (18), 5106-5112 (1998)
- [36] Laguecir, A., Ulrich, S., Labille, J., Fatin-Rouge, N., Stoll, S., Buffle, J., Size and pH Effect on Electrical and Conformational Behavior of Poly(acrylic acid): Simulation and Experiment. *Eur. Polym. J.* **42** (5), 1135-1144 (2006).
- [37] Liu, L. J., Chen, J. Z., An, L. J., Individual Circular Polyelectrolytes Under Shear Flow. *J. Chem. Phys.* **149** (16) (2018)
- [38] Lin, S. H., Wiesner, M. R., Theoretical Investigation on the Interaction Between a Soft Particle and a Rigid Surface. *Chem. Eng. J.* **191**, 297-305 (2012)
- [39] Szilagyi, I., Trefalt, G., Tiraferri, A., Maroni, P., Borkovec, M., Polyelectrolyte Adsorption, Interparticle Forces, and Colloidal Aggregation. *Soft Matter* **10** (15), 2479-2502 (2014).
- [40] Radhakrishnan, R., Underhill, P. T., Influence of Shear on Globule Formation in Dilute Solutions of Flexible Polymers. *J. Chem. Phys.* **142** (14) (2015).
- [41] Hidber, P. C., Graule, T. J., Gauckler, L. J., Competitive Adsorption of Citric-Acid and Poly(vinyl alcohol) onto Alumina and its Influence on the Binder Migration During Drying. *J. Am. Ceram. Soc.* **78** (7), 1775-1780 (1995).
- [42] Zhang, Y., Suga, T., Kawasaki, M., Tang, X. X., Uchida, N., Uematsu, K., Effect of Poly(vinyl alcohol) Adsorption on Binder Segregation During Drying. *J. Am. Ceram. Soc.* **79** (2), 435-440 (1996)
- [43] Hoda, N., Kumar, S., Brownian Dynamics Simulations of Polyelectrolyte Adsorption in Shear Flow: Effects of Solvent Quality and Charge Patterning. *J. Chem. Phys.* **128** (16) (2008).
- [44] *United States Advanced Battery Consortium Battery Test Manual For Electric Vehicles*, 2015.
- [45] Long, B. R., Rinaldo, S. G., Gallagher, K. G., Dees, D. W., Trask, S. E., Polzin, B. J., Jansen, A. N., Abraham, D. P., Bloom, I., Bareño, J., Croy, J. R. "Enabling High-Energy, High-Voltage Lithium-Ion Cells: Standardization of Coin-Cell Assembly, Electrochemical Testing, and Evaluation of Full Cells". *35th Annu. Int. Batter. Semin. Exhib. 2018* **1** (14), 112-122. (2018)
- [46] Single, F., Latz, A., Horstmann, B. "Identifying the Mechanism of Continued Growth of the Solid-Electrolyte Interphase" *ChemSusChem* **11** (12), 1950-1955 (2018)
- [47] Attia, P. M., Chueh, W. C., Harris, S. J. Revisiting the t^{0.5} Dependence of SEI Growth. *J. Electrochem. Soc.* **167**(9), 090535.(2020)

